Monthly Notices
of the
ROYAL ASTRONOMICAL SOCIETY

MNRAS **432,** 1862–1893 (2013)
Advance Access publication 2013 May 16

doi:10.1093/mnras/stt644

The ATLAS^{3D} project – XX. Mass–size and mass–σ distributions of early-type galaxies: bulge fraction drives kinematics, mass-to-light ratio, molecular gas fraction and stellar initial mass function

Michele Cappellari,[1⋆] Richard M. McDermid,[2] Katherine Alatalo,[3] Leo Blitz,[3] Maxime Bois,[4] Frédéric Bournaud,[5] M. Bureau,[1] Alison F. Crocker,[6] Roger L. Davies,[1] Timothy A. Davis,[1,7] P. T. de Zeeuw,[7,8] Pierre-Alain Duc,[5] Eric Emsellem,[7,9] Sadegh Khochfar,[10] Davor Krajnović,[7] Harald Kuntschner,[7] Raffaella Morganti,[11,12] Thorsten Naab,[13] Tom Oosterloo,[11,12] Marc Sarzi,[14] Nicholas Scott,[1,15] Paolo Serra,[11] Anne-Marie Weijmans[16] and Lisa M. Young[17]

[1]*Sub-department of Astrophysics, Department of Physics, University of Oxford, Denys Wilkinson Building, Keble Road, Oxford OX1 3RH, UK*
[2]*Gemini Observatory, Northern Operations Centre, 670 N. A'ohoku Place, Hilo, HI 96720, USA*
[3]*Department of Astronomy, Campbell Hall, University of California, Berkeley, CA 94720, USA*
[4]*Observatoire de Paris, LERMA and CNRS, 61 Av. de l'Observatoire, F-75014 Paris, France*
[5]*Laboratoire AIM Paris-Saclay, CEA/IRFU/SAp, CNRS, Université Paris Diderot, F-91191 Gif-sur-Yvette Cedex, France*
[6]*Department of Astrophysics, University of Massachusetts, 710 North Pleasant Street, Amherst, MA 01003, USA*
[7]*European Southern Observatory, Karl-Schwarzschild-Str. 2, D-85748 Garching, Germany*
[8]*Sterrewacht Leiden, Leiden University, Postbus 9513, NL-2300 RA Leiden, the Netherlands*
[9]*Université Lyon 1, Observatoire de Lyon, Centre de Recherche Astrophysique de Lyon and Ecole Normale Supérieure de Lyon, 9 avenue Charles André, F-69230 Saint-Genis Laval, France*
[10]*Max-Planck Institut für extraterrestrische Physik, PO Box 1312, D-85478 Garching, Germany*
[11]*Netherlands Institute for Radio Astronomy (ASTRON), Postbus 2, NL-7990 AA Dwingeloo, the Netherlands*
[12]*Kapteyn Astronomical Institute, University of Groningen, Postbus 800, NL-9700 AV Groningen, the Netherlands*
[13]*Max-Planck Institut für Astrophysik, Karl-Schwarzschild-Str. 1, D-85741 Garching, Germany*
[14]*Centre for Astrophysics Research, University of Hertfordshire, Hatfield, Herts AL1 9AB, UK*
[15]*Centre for Astrophysics & Supercomputing, Swinburne University of Technology, PO Box 218, Hawthorn, VIC 3122, Australia*
[16]*Dunlap Institute for Astronomy & Astrophysics, University of Toronto, 50 St George Street, Toronto, ON M5S 3H4, Canada*
[17]*Physics Department, New Mexico Institute of Mining and Technology, Socorro, NM 87801, USA*

Accepted 2013 April 15. Received 2013 March 24; in original form 2012 August 17

ABSTRACT

In the companion Paper XV of this series, we derive accurate total mass-to-light ratios $(M/L)_{JAM} \approx (M/L)(r = R_e)$ within a sphere of radius $r = R_e$ centred on the galaxy, as well as stellar $(M/L)_{stars}$ (with the dark matter removed) for the volume-limited and nearly mass-selected (stellar mass $M_\star \gtrsim 6 \times 10^9\,M_\odot$) ATLAS^{3D} sample of 260 early-type galaxies (ETGs, ellipticals Es and lenticulars S0s). Here, we use those parameters to study the two orthogonal projections (M_{JAM}, σ_e) and (M_{JAM}, R_e^{maj}) of the thin Mass Plane (MP) (M_{JAM}, σ_e, R_e^{maj}) which describes the distribution of the galaxy population, where $M_{JAM} \equiv L \times (M/L)_{JAM} \approx M_\star$. The distribution of galaxy properties on both projections of the MP is characterized by: (i) the same zone of exclusion (ZOE), which can be transformed from one projection to the other using the scalar virial equation. The ZOE is roughly described by two power laws, joined by a break at a characteristic mass $M_{JAM} \approx 3 \times 10^{10}\,M_\odot$, which corresponds to the minimum R_e and maximum stellar density. This results in a break in the mean M_{JAM}–σ_e relation with trends $M_{JAM} \propto \sigma_e^{2.3}$ and $M_{JAM} \propto \sigma_e^{4.7}$ at small and large σ_e, respectively; (ii) a characteristic mass $M_{JAM} \approx 2 \times 10^{11}\,M_\odot$ which separates a population dominated by flat fast rotator with discs

⋆ E-mail: cappellari@astro.ox.ac.uk

and spiral galaxies at lower masses, from one dominated by quite round slow rotators at larger masses; (iii) below that mass the distribution of ETGs' properties on the two projections of the MP tends to be constant along lines of roughly constant σ_e, or equivalently along lines with $R_e^{maj} \propto M_{JAM}$, respectively (or even better parallel to the ZOE: $R_e^{maj} \propto M_{JAM}^{0.75}$); (iv) it forms a continuous and parallel sequence with the distribution of spiral galaxies; (v) at even lower masses, the distribution of fast-rotator ETGs and late spirals naturally extends to that of dwarf ETGs (Sph) and dwarf irregulars (Im), respectively.

We use dynamical models to analyse our kinematic maps. We show that σ_e traces the bulge fraction, which appears to be the main driver for the observed trends in the dynamical $(M/L)_{JAM}$ and in indicators of the $(M/L)_{pop}$ of the stellar population like Hβ and colour, as well as in the molecular gas fraction. A similar variation along contours of σ_e is also observed for the mass normalization of the stellar initial mass function (IMF), which was recently shown to vary systematically within the ETGs' population. Our preferred relation has the form $\log_{10}[(M/L)_{stars}/(M/L)_{Salp}] = a + b \times \log_{10}(\sigma_e/130\,km\,s^{-1})$ with $a = -0.12 \pm 0.01$ and $b = 0.35 \pm 0.06$. Unless there are major flaws in all stellar population models, this trend implies a transition of the mean IMF from Kroupa to Salpeter in the interval $\log_{10}(\sigma_e/km\,s^{-1}) \approx 1.9$–$2.5$ (or $\sigma_e \approx 90$–$290\,km\,s^{-1}$), with a smooth variation in between, consistently with what was shown in Cappellari et al. The observed distribution of galaxy properties on the MP provides a clean and novel view for a number of previously reported trends, which constitute special two-dimensional projections of the more general four-dimensional parameters trends on the MP. We interpret it as due to a combination of two main effects: (i) an increase of the bulge fraction, which increases σ_e, decreases R_e, and greatly enhance the likelihood for a galaxy to have its star formation quenched, and (ii) dry merging, increasing galaxy mass and R_e by moving galaxies along lines of roughly constant σ_e (or steeper), while leaving the population nearly unchanged.

Key words: galaxies: elliptical and lenticular, cD – galaxies: evolution – galaxies: formation – galaxies: kinematics and dynamics – galaxies: structure.

1 INTRODUCTION

Much of our understanding of galaxy formation and evolution comes from the study of dynamical scaling relations relating galaxy luminosity or mass, size and kinematic (e.g. Faber & Jackson 1976; Kormendy 1977; Dressler et al. 1987; Djorgovski & Davis 1987; Faber et al. 1987) or regular trends in the distribution of galaxy properties as a function of their scaling parameters (e.g. Bender, Burstein & Faber 1992; Burstein et al. 1997; Kauffmann et al. 2003b; Gallazzi et al. 2006) and from the study of their evolution with redshift (e.g. van Dokkum & Franx 1996; Kelson et al. 1997; van Dokkum et al. 1998; Treu et al. 2005; Franx et al. 2008).

The volume-limited ATLAS^{3D} sample of nearby early-type galaxies (ETGs; Cappellari et al. 2011a, hereafter Paper I) constitute an ideal benchmark for studying scaling relations and the distribution of galaxy properties, given the availability of a high-quality multiwavelength data set. In particular, in Cappellari et al. (2013, hereafter Paper XV), we used the state-of-the-art integral-field kinematics, in combination with detailed axisymmetric dynamical models, to derive accurate masses and global dynamical parameter. We found that galaxies lie, with very good accuracy, on a thin Mass Plane (MP) describing galaxies in the parameter space defined by mass, velocity dispersion and projected half-light radius (M_{JAM}, σ_e, R_e^{maj}). Here, M_{JAM} is a very good estimate of the galaxy total stellar mass, R_e^{maj} is the major axis of the 'effective' isophote containing half of the observed galaxy light and σ_e is the velocity dispersion measured within that isophote. The existence of this MP is mainly due to the virial equilibrium condition

$$M_{JAM} \propto \sigma_e^2 R_e^{maj} \quad (1)$$

combined with a smooth variation of galaxy properties with σ_e. For this reason, by itself it contains no useful information on galaxy formation. All the useful constraints on galaxy formation models come from the inhomogeneous distribution of galaxies in non-edge-on views of the MP and from the distribution of galaxy properties along the MP.

This paper is devoted to a study of the non-edge-on projections of the MP to see what we learn from it on galaxy formation. This is done in the spirit of the classic papers by Bender et al. (1992) and Burstein et al. (1997). However, the fact that we have accurate dynamical masses implies that our MP is extremely thin and it follows the scalar virial relation (1) quite accurately. For this reason, we can ignore edge-on views of the plane and focus on non-edge-on projections only. The thinness of the MP implies that any inclined projection shows essentially the same information, after a change of coordinates. We can use standard and easy-to-understand observables as our main coordinates, instead of trying to observe the plane at a precisely face-on view.

In this paper, in Section 2, we summarize the sample and data; in Section 3, we present our projections of the MP. We illustrate the distribution of a number of quantities on the (M_{JAM}, σ_e) and (M_{JAM}, R_e^{maj}) projection. We show the variation of the $(M/L)_{JAM}$, as well as of population indicators of M/L and of the molecular

gas fraction. We also show the variation of galaxy concentration, intrinsic shape, morphology and stellar rotation. The variations of the stellar initial mass function (IMF) are separately presented in Section 4, together with a review of previous results on the IMF variation. In Section 5, we discuss the implications of our findings for galaxy formation and briefly summarize our paper in Section 6.

2 SAMPLE AND DATA

2.1 Selection and completeness confirmation

The galaxies studied in this work are the 260 ETGs which constitute the volume-limited and nearly mass-selected ATLAS^{3D} sample (Paper I). The objects were morphologically selected as early type according to the standard criterion (Hubble 1936; de Vaucouleurs 1959; Sandage 1961) of not showing spiral arms or a disc-scale dust lane (when seen edge-on). The early types are extracted from a parent sample of 871 galaxies of all morphological types brighter than $M_K = -21.5$ mag, using 2MASS photometry (Skrutskie et al. 2006), inside a local ($D < 42$ Mpc) volume of 1.16×10^5 Mpc^3 (see full details in Paper I).

In Paper I (Section 2.3), we discussed possible incompleteness in the volume-limited parent sample of 871 galaxies, from which the ATLAS^{3D} sample of ETGs was extracted, due to lack of redshift determinations at the faint-end limit of our selection. We concluded that the parent sample was 99 per cent complete. We pointed out that the 2MASS redshift survey (2MRS) was going to change the situation by providing redshifts for the all galaxies brighter than the apparent total magnitude $K_T < 11.6$ mag, which makes a galaxy a potential candidate for satisfying our absolute magnitude cut of $M_K < -21.5$ mag, within the adopted $D = 42$ Mpc volume. The 2MRS was recently released with a completeness of 98 per cent for $K_T \leq 11.75$ mag (Huchra et al. 2012). This allowed us to explicitly verify the completeness level estimated in Paper I. For this, we used the redshifts from the 2MRS, in combination with the available redshift-independent distance determinations, to repeat the selection of the ATLAS^{3D} parent sample as described in Paper I. We confirmed that our parent sample has a completeness of 98 per cent, quite close to our original estimation.

In Paper XV, we compared our sample to previous samples for which accurate dynamical masses have been determined either via gravitational lensing (e.g. Bolton et al. 2008b; Auger et al. 2010b) or dynamics (e.g. Magorrian et al. 1998; Cappellari et al. 2006; Thomas et al. 2009) and concluded that it provides a major step forward in sample size and accuracy.

2.2 Stellar kinematics and imaging

Various multiwavelengths data sets are available for the sample galaxies (see a summary in Paper I). In this work, we make use of the SAURON (Bacon et al. 2001) integral-field stellar kinematics within about one half-light radius R_e. The kinematics of all galaxies in the ATLAS^{3D} sample was homogeneously extracted as described in Paper I, using the penalized pixel-fitting (PPXF) software[1] (Cappellari & Emsellem 2004) and the full MILES stellar library (Sánchez-Blázquez et al. 2006; Falcón-Barroso et al. 2011) as templates. For the subset of 48 early types in the SAURON survey (de Zeeuw et al. 2002), the kinematics had already been presented in Emsellem et al. (2004).

The photometry used in this work comes from the Sloan Digital Sky Survey (SDSS; York et al. 2000) data release 8 (DR8; Aihara et al. 2011) and was supplemented by our own photometry taken at the 2.5-m Isaac Newton Telescope (INT) in the same set of filters and with comparable signal to noise (S/N) for the rest of the sample galaxies (Scott et al. 2013a, hereafter Paper XXI).

2.3 Measuring galaxy global parameters: M/L, R_e and σ_e

The dynamical masses used in this paper were obtained with the dynamical models of the ATLAS^{3D} sample presented in Cappellari et al. (2012) and described in more detail in Paper XV. In brief, the modelling approach starts by approximating the observed SDSS and INT r-band surface brightness distribution of the ATLAS^{3D} galaxies using the Multi-Gaussian Expansion (MGE) parametrization (Emsellem, Monnet & Bacon 1994), with the fitting method and software[1] of Cappellari (2002). Full details of the approach and all the resulting MGE fits are given in Paper XXI. The MGE models are used as input for the Jeans Anisotropic MGE (JAM) modelling method[1] (Cappellari 2008) which calculates a prediction of the line-of-sight second velocity moments $\langle v_{los}^2 \rangle$ for a given set of model parameters and fits this to the observed $V_{rms} \equiv \sqrt{V^2 + \sigma^2}$ using a Bayesian approach (Gelman et al. 2004). The models assume axisymmetry and include a spherical dark halo, which is parametrized according to six different sets of assumptions (see Paper XV for full details). In Cappellari et al. (2012), we showed that the adopted assumptions on the halo have insignificant influence on the measured trend of M/L. For this reason, in this paper, we only use the two simplest sets of models from that paper (using the same notation):

(A) Self-consistent axisymmetric JAM model, in which the dark matter (DM) is assumed to be proportional to the stellar one. We call the total (luminous plus dark) M/L of this model $(M/L)_{JAM}$.

(B) Axisymmetric JAM model with spherical Navarro, Frenk & White (1996) (NFW) DM halo. Here, the M/L of the stars alone $(M/L)_{stars}$ is measured directly.

Lablanche et al. (2012, hereafter Paper XII) studied the accuracy in the M/L obtained with the JAM method, using N-body simulations that resemble real galaxies, and concluded that the M/L of unbarred galaxies can be measured with negligible bias <1.5 per cent, while the M/L of barred galaxies that resemble typical bars found in the ATLAS^{3D} sample can bias the determination by up to 15 per cent in our tests, depending on the position angle of the bars.

The M/L of the stellar population $(M/L)_{Salp}$ in the SDSS r band was presented in Cappellari et al. (2012). It was extracted using the PPXF method and software of Cappellari & Emsellem (2004) for full spectrum fitting. In this case, the model templates consisted of a regular rectangular grid of 26 ages and 6 metallicities [M/H], assuming a Salpeter (1955) IMF for reference, from the MILES models[2] of Vazdekis et al. (2012). We used the PPXF keyword REGUL to enforce linear regularization (Press et al. 1992, equation 18.5.10) in the recovered set of templates weights w_j from the fit. The regularization parameter was chosen for every galaxy to obtain an increase $\Delta\chi^2 = \sqrt{2 \times N_{pix}}$ in the χ^2, with respect to a non-regularized fit. In this way, the recovered w_j solution constitutes the smoothest one consistent with the observed spectrum (see fig. 20 of Onodera et al. 2012 for an example). This regularized approach helps reducing the noise in the $(M/L)_{Salp}$ determination; however, the results are

[1] Available from http://purl.org/cappellari/idl

[2] Available from http://miles.iac.es/

quite insensitive to the precise value of this parameter and remain essentially unchanged for a range of plausible values. Once the weights for the N model templates have been obtained with PPXF, the properly mass-weighted M/L of the combined population is given by

$$(\mathrm{M/L})_{\mathrm{Salp},r} = \frac{\sum_{j=1}^{N} w_j M_j^{\mathrm{nogas}}}{\sum_{j=1}^{N} w_j L_{j,r}}, \quad (2)$$

where M_j^{nogas} is the mass of the jth model in living stars and stellar remnants (black holes and neutron stars), but excluding the gas lost during stellar evolution and $L_{j,r}$ is the corresponding r-band luminosity of the population. The values are given in Table 1. The details on our spectral fitting of the SAURON data and the analysis of the resulting weight distributions is presented in McDermid et al. (in preparation).

Effective radii are defined as the projected half-light radii of the isophote containing half of the total analytic light of the MGE models from Paper XXI. Both circularized radii R_{e} and the more inclination-independent major axes $R_{\mathrm{e}}^{\mathrm{maj}}$ were extracted as described in Paper XV and are taken from table 1 there.

Effective velocity dispersions σ_{e} were measured by co-adding all the spectra in the SAURON data cube contained within the half-light isophote. The resulting 'effective' spectrum was fitted with PPXF using the full MILES stellar library as templates, and assuming a Gaussian line-of-sight velocity distribution. Gas emission around the possible Hβ and O III emission lines were systematically excluded from the fits and the CLEAN keyword of PPXF was used to reject possible remaining outliers from the spectra. The values for the sample are given in table 1 of Paper XV.

3 PROJECTIONS OF THE MP

3.1 Total M/L variations

We have shown in Paper XV that the existence of the Fundamental Plane (FP; Djorgovski & Davis 1987; Dressler et al. 1987) is due, with good accuracy, to a virial equilibrium condition combined with a smooth variation of galaxy properties, mainly the total mass-to-light ratio M/L, with velocity dispersion. Once this is clarified, the edge-on projection of the MP becomes uninteresting from the point of view of the study of galaxy formation, as it merely states an equilibrium condition satisfied by galaxies and it does not encode any memory of the formation process itself. This is in agreement with previous findings with simulations (Nipoti, Londrillo & Ciotti 2003; Boylan-Kolchin, Ma & Quataert 2006). All information provided by scaling relations on galaxy formation is now encoded in the non-edge-on projections of the MP, and first of all in the distribution of M/L on that plane. In Paper XV, we also confirmed that M/L correlates remarkably tightly with σ_{e} (Cappellari et al. 2006). This is especially true (i) for slow rotators, (ii) for galaxies in clusters and (iii) at the high end of the σ_{e} range. Here, we look at the entire MP and try to clarify the reason for these and other galaxy correlations.

In a classic paper, Bender et al. (1992) studied the distribution of hot stellar systems in a three-dimensional space, they called κ space, defined in such a way that one of the axes was empirically defined to lie nearly orthogonal to the plane. This made it easy to look at both the edge-on and face-on versions of the plane. In this paper, thanks to the availability of state-of-the-art integral-field kinematics and the construction of detailed dynamical models, we can use mass as one of the three variables (M_{JAM}, σ_{e}, $R_{\mathrm{e}}^{\mathrm{maj}}$). We have shown in

Table 1. Central velocity dispersion, DM fraction and M/L for the ATLAS^{3D} sample of 260 ETGs (see the Supporting Information with the electronic version of the article for an ASCII file of this table).

Galaxy	$\log\sigma(R_{\mathrm{e}}/8)$ (km s^{-1})	$f_{\mathrm{DM}}(r = R_{\mathrm{e}})$	$\log(\mathrm{M/L})_{\mathrm{stars}}$ ($\mathrm{M}_\odot/\mathrm{L}_{\odot r}$)	$\log(\mathrm{M/L})_{\mathrm{Salp}}$ ($\mathrm{M}_\odot/\mathrm{L}_{\odot r}$)
(1)	(2)	(3)	(4)	(5)
IC 0560	1.920	0.12	0.429	0.381
IC 0598	2.001	0.24	0.268	0.364
IC 0676	1.825	0.20	0.481	0.261
IC 0719	1.934	0.11	0.833	0.518
IC 0782	1.818	0.57	0.318	0.510
IC 1024	1.772	0.15	0.570	0.194
IC 3631	1.733	0.00	−0.153	0.109
NGC 0448	1.988	0.14	0.396	0.673
NGC 0474	2.223	0.00	0.620	0.724
NGC 0502	2.107	0.00	0.466	0.725
NGC 0509	1.792	0.07	0.495	0.388
NGC 0516	1.743	0.16	0.421	0.573
NGC 0524	2.386	0.43	0.625	0.840
NGC 0525	1.954	0.00	0.710	0.706
NGC 0661	2.279	0.08	0.929	0.754
NGC 0680	2.316	0.08	0.713	0.739
NGC 0770	2.045	0.19	0.362	0.696
NGC 0821	2.300	0.18	0.734	0.773
NGC 0936	2.292	0.38	0.504	0.824
NGC 1023	2.316	0.00	0.531	0.827
NGC 1121	2.235	0.13	0.706	0.786
NGC 1222	1.840	0.76	0.219	−0.014
NGC 1248	1.965	0.00	0.326	0.488
NGC 1266	1.897	0.00	0.598	0.364
NGC 1289	2.133	0.14	0.577	0.578
NGC 1665	1.999	0.12	0.450	0.567
NGC 2481	2.271	0.06	0.642	0.706
NGC 2549	2.174	0.17	0.666	0.710
NGC 2577	2.320	0.06	0.843	0.790
NGC 2592	2.384	0.01	0.882	0.812
NGC 2594	2.263	0.07	0.659	0.729
NGC 2679	1.983	0.17	0.423	0.576
NGC 2685	1.972	0.18	0.327	0.620
NGC 2695	2.342	0.11	0.672	0.795
NGC 2698	2.355	0.00	0.749	0.802
NGC 2699	2.181	0.07	0.538	0.724
NGC 2764	1.954	0.00	0.649	0.154
NGC 2768	2.306	0.00	0.933	0.772
NGC 2778	2.215	0.04	0.842	0.768
NGC 2824	2.127	0.45	0.262	0.343
NGC 2852	2.306	0.00	0.834	0.784
NGC 2859	2.252	0.06	0.546	0.732
NGC 2880	2.150	0.25	0.580	0.675
NGC 2950	2.230	0.11	0.539	0.661
NGC 2962	2.244	0.00	0.813	0.782
NGC 2974	2.375	0.07	0.950	0.787
NGC 3032	1.983	0.42	0.164	−0.070
NGC 3073	1.755	0.44	0.105	−0.145
NGC 3098	2.038	0.18	0.517	0.612
NGC 3156	1.838	0.23	0.245	0.132
NGC 3182	2.060	0.48	0.336	0.606
NGC 3193	2.299	0.08	0.532	0.794
NGC 3226	2.250	0.00	0.873	0.784
NGC 3230	2.303	0.04	0.754	0.795
NGC 3245	2.322	0.11	0.588	0.727
NGC 3248	1.990	0.15	0.420	0.527
NGC 3301	2.096	0.21	0.297	0.448
NGC 3377	2.163	0.06	0.553	0.731
NGC 3379	2.329	0.33	0.600	0.838
NGC 3384	2.208	0.22	0.404	0.724

Table 1 – *continued*

Galaxy	$\log\sigma(R_e/8)$ (km s^{-1})	$f_{DM}(r=R_e)$	$\log(M/L)_{stars}$ ($M_\odot/L_{\odot,r}$)	$\log(M/L)_{Salp}$ ($M_\odot/L_{\odot,r}$)
(1)	(2)	(3)	(4)	(5)
NGC 3400	1.878	0.18	0.522	0.687
NGC 3412	2.022	0.47	0.211	0.648
NGC 3414	2.365	0.14	0.714	0.826
NGC 3457	1.889	0.21	0.173	0.517
NGC 3458	2.253	0.05	0.627	0.767
NGC 3489	2.028	0.24	0.113	0.394
NGC 3499	1.845	0.25	0.189	0.449
NGC 3522	2.011	0.24	0.582	0.648
NGC 3530	2.049	0.23	0.493	0.695
NGC 3595	2.206	0.00	0.602	0.749
NGC 3599	1.874	0.11	0.234	0.467
NGC 3605	1.966	0.00	0.459	0.668
NGC 3607	2.360	0.07	0.661	0.799
NGC 3608	2.286	0.09	0.669	0.829
NGC 3610	2.244	0.12	0.409	0.566
NGC 3613	2.327	0.00	0.772	0.761
NGC 3619	2.221	0.28	0.615	0.693
NGC 3626	2.134	0.23	0.332	0.261
NGC 3630	2.241	0.13	0.550	0.745
NGC 3640	2.267	0.17	0.534	0.722
NGC 3641	2.241	0.34	0.821	0.773
NGC 3648	2.277	0.21	0.694	0.807
NGC 3658	2.216	0.00	0.572	0.721
NGC 3665	2.352	0.14	0.748	0.764
NGC 3674	2.346	0.04	0.811	0.809
NGC 3694	1.892	0.60	0.082	0.437
NGC 3757	2.170	0.20	0.610	0.705
NGC 3796	1.955	0.34	0.243	0.387
NGC 3838	2.144	0.00	0.589	0.694
NGC 3941	2.144	0.00	0.400	0.693
NGC 3945	2.262	0.22	0.549	0.760
NGC 3998	2.445	0.15	0.920	0.818
NGC 4026	2.279	0.08	0.633	0.747
NGC 4036	2.276	0.00	0.697	0.783
NGC 4078	2.242	0.07	0.823	0.755
NGC 4111	2.201	0.00	0.651	0.616
NGC 4119	1.771	0.20	0.423	0.306
NGC 4143	2.336	0.16	0.646	0.834
NGC 4150	1.945	0.20	0.336	0.358
NGC 4168	2.241	0.25	0.775	0.738
NGC 4179	2.264	0.08	0.724	0.771
NGC 4191	2.127	0.22	0.533	0.685
NGC 4203	2.202	0.00	0.536	0.827
NGC 4215	2.147	0.04	0.589	0.652
NGC 4233	2.337	0.22	0.724	0.812
NGC 4249	1.885	0.78	−0.071	0.672
NGC 4251	2.137	0.08	0.360	0.684
NGC 4255	2.255	0.04	0.785	0.743
NGC 4259	2.060	0.51	0.212	0.728
NGC 4261	2.469	0.28	0.820	0.859
NGC 4262	2.290	0.02	0.751	0.782
NGC 4264	2.021	0.31	0.464	0.668
NGC 4267	2.193	0.17	0.548	0.831
NGC 4268	2.194	0.20	0.744	0.672
NGC 4270	2.153	0.00	0.542	0.669
NGC 4278	2.395	0.26	0.734	0.846
NGC 4281	2.409	0.00	0.956	0.788
NGC 4283	2.078	0.00	0.568	0.770
NGC 4324	1.969	0.32	0.310	0.620
NGC 4339	2.093	0.00	0.684	0.728
NGC 4340	2.030	0.34	0.484	0.700
NGC 4342	2.403	0.01	1.018	0.822

Table 1 – *continued*

Galaxy	$\log\sigma(R_e/8)$ (km s^{-1})	$f_{DM}(r=R_e)$	$\log(M/L)_{stars}$ ($M_\odot/L_{\odot,r}$)	$\log(M/L)_{Salp}$ ($M_\odot/L_{\odot,r}$)
(1)	(2)	(3)	(4)	(5)
NGC 4346	2.162	0.22	0.517	0.718
NGC 4350	2.300	0.08	0.717	0.826
NGC 4365	2.408	0.18	0.688	0.862
NGC 4371	2.142	0.27	0.596	0.789
NGC 4374	2.460	0.15	0.761	0.846
NGC 4377	2.164	0.53	0.284	0.733
NGC 4379	2.069	0.00	0.600	0.735
NGC 4382	2.264	0.50	0.438	0.578
NGC 4387	2.024	0.00	0.574	0.759
NGC 4406	2.336	0.17	0.717	0.816
NGC 4417	2.183	0.13	0.569	0.771
NGC 4425	1.921	0.14	0.529	0.638
NGC 4429	2.292	0.00	0.787	0.824
NGC 4434	2.116	0.00	0.416	0.753
NGC 4435	2.214	0.13	0.518	0.734
NGC 4442	2.288	0.00	0.672	0.838
NGC 4452	1.771	0.00	0.706	0.679
NGC 4458	2.032	0.15	0.460	0.740
NGC 4459	2.252	0.20	0.572	0.721
NGC 4461	2.173	0.06	0.621	0.792
NGC 4472	2.460	0.00	0.746	0.856
NGC 4473	2.287	0.24	0.574	0.780
NGC 4474	1.964	0.05	0.482	0.660
NGC 4476	1.854	0.20	0.324	0.382
NGC 4477	2.234	0.47	0.602	0.788
NGC 4478	2.160	0.00	0.715	0.775
NGC 4483	1.966	0.30	0.472	0.757
NGC 4486	2.497	0.13	0.815	0.883
NGC 4486A	2.156	0.00	0.656	0.705
NGC 4489	1.812	0.77	−0.030	0.556
NGC 4494	2.188	0.20	0.511	0.699
NGC 4503	2.170	0.00	0.733	0.815
NGC 4521	2.247	0.16	0.774	0.778
NGC 4526	2.371	0.00	0.748	0.775
NGC 4528	2.044	0.01	0.580	0.641
NGC 4546	2.345	0.00	0.737	0.810
NGC 4550	1.974	0.21	0.537	0.656
NGC 4551	1.998	0.00	0.697	0.769
NGC 4552	2.418	0.21	0.743	0.861
NGC 4564	2.241	0.04	0.669	0.792
NGC 4570	2.281	0.15	0.574	0.820
NGC 4578	2.043	0.38	0.514	0.739
NGC 4596	2.179	0.18	0.638	0.776
NGC 4608	2.139	0.00	0.633	0.766
NGC 4612	1.934	0.56	0.168	0.448
NGC 4621	2.350	0.03	0.759	0.846
NGC 4623	1.835	0.50	0.309	0.723
NGC 4624	2.156	0.25	0.582	0.794
NGC 4636	2.300	0.39	0.789	0.844
NGC 4638	2.080	0.05	0.433	0.703
NGC 4643	2.184	0.14	0.635	0.755
NGC 4649	2.498	0.29	0.774	0.871
NGC 4660	2.338	0.10	0.601	0.817
NGC 4684	1.837	0.10	0.304	0.571
NGC 4690	2.052	0.00	0.590	0.542
NGC 4694	1.792	0.00	0.150	−0.042
NGC 4697	2.257	0.00	0.703	0.800
NGC 4710	2.021	0.00	0.645	0.587
NGC 4733	1.750	0.00	0.338	0.518
NGC 4753	2.263	0.25	0.519	0.615
NGC 4754	2.254	0.21	0.596	0.815
NGC 4762	2.129	0.23	0.417	0.760

Table 1 – *continued*

Galaxy	$\log\sigma(R_e/8)$ (km s^{-1})	$f_{DM}(r = R_e)$	$\log(M/L)_{stars}$ ($M_\odot/L_{\odot,r}$)	$\log(M/L)_{Salp}$ ($M_\odot/L_{\odot,r}$)
(1)	(2)	(3)	(4)	(5)
NGC 4803	2.016	0.55	0.336	0.670
NGC 5103	2.061	0.22	0.376	0.695
NGC 5173	2.005	0.33	0.261	0.507
NGC 5198	2.304	0.00	0.794	0.809
NGC 5273	1.870	0.55	0.247	0.502
NGC 5308	2.376	0.09	0.744	0.790
NGC 5322	2.395	0.16	0.634	0.700
NGC 5342	2.254	0.21	0.676	0.773
NGC 5353	2.462	0.11	0.769	0.855
NGC 5355	1.918	0.47	0.227	0.279
NGC 5358	1.886	0.27	0.477	0.623
NGC 5379	1.840	0.73	0.307	0.468
NGC 5422	2.242	0.21	0.670	0.758
NGC 5473	2.332	0.49	0.511	0.783
NGC 5475	2.041	0.33	0.411	0.544
NGC 5481	2.174	0.00	0.776	0.740
NGC 5485	2.253	0.09	0.806	0.777
NGC 5493	2.208	0.20	0.305	0.514
NGC 5500	1.915	0.13	0.649	0.650
NGC 5507	2.320	0.17	0.708	0.786
NGC 5557	2.406	0.01	0.659	0.774
NGC 5574	1.885	0.04	0.378	0.368
NGC 5576	2.269	0.00	0.454	0.705
NGC 5582	2.180	0.37	0.599	0.752
NGC 5611	2.120	0.06	0.651	0.645
NGC 5631	2.207	0.10	0.580	0.627
NGC 5638	2.202	0.06	0.647	0.791
NGC 5687	2.280	0.12	0.864	0.768
NGC 5770	1.988	0.12	0.328	0.576
NGC 5813	2.354	0.47	0.699	0.816
NGC 5831	2.220	0.14	0.610	0.743
NGC 5838	2.441	0.00	0.901	0.834
NGC 5839	2.208	0.01	0.716	0.802
NGC 5845	2.431	0.00	0.695	0.810
NGC 5846	2.365	0.14	0.844	0.853
NGC 5854	2.061	0.12	0.356	0.472
NGC 5864	2.079	0.00	0.570	0.636
NGC 5866	2.205	0.00	0.663	0.640
NGC 5869	2.260	0.24	0.750	0.787
NGC 6010	2.213	0.17	0.685	0.719
NGC 6014	1.953	0.48	0.429	0.518
NGC 6017	2.041	0.00	0.447	0.526
NGC 6149	2.031	0.31	0.425	0.611
NGC 6278	2.338	0.16	0.667	0.812
NGC 6547	2.285	0.12	0.740	0.629
NGC 6548	2.240	0.20	0.768	0.698
NGC 6703	2.260	0.00	0.775	0.736
NGC 6798	2.137	0.16	0.564	0.684
NGC 7280	2.061	0.36	0.406	0.444
NGC 7332	2.143	0.07	0.288	0.528
NGC 7454	2.049	0.13	0.673	0.585
NGC 7457	1.874	0.45	0.238	0.455
NGC 7465	1.971	0.05	0.333	0.348
NGC 7693	1.816	0.00	0.586	0.357
NGC 7710	2.019	0.00	0.537	0.616
PGC 016060	1.992	0.00	0.651	0.509
PGC 028887	2.132	0.35	0.643	0.730
PGC 029321	1.762	0.90	−0.541	0.362
PGC 035754	2.067	0.00	0.577	0.634
PGC 042549	2.004	0.14	0.422	0.506
PGC 044433	2.123	0.10	0.688	0.724
PGC 050395	1.869	0.74	−0.061	0.581
PGC 051753	1.892	0.15	0.584	0.621
PGC 054452	1.818	0.28	0.411	0.534
PGC 056772	1.916	0.00	0.620	0.379
PGC 058114	1.902	–	–	0.474
PGC 061468	1.823	0.90	−0.280	0.415
PGC 071531	1.969	–	–	0.479
PGC 170172	2.020	0.16	0.111	0.650
UGC 03960	1.946	0.04	0.729	0.606
UGC 04551	2.265	0.04	0.658	0.737
UGC 05408	1.919	0.00	0.194	0.331
UGC 06062	2.156	0.25	0.629	0.760
UGC 06176	2.045	0.50	0.331	0.328
UGC 08876	2.152	0.00	0.760	0.740
UGC 09519	1.992	0.10	0.513	0.345

Note. Column (1): the Name is the principal designation from LEDA (Paturel et al. 2003), which is used as standard designation for our project. Column (2): central stellar velocity dispersion (1σ random error of 5 per cent or 0.021 dex) within a circular aperture of radius $R = R_e/8$, where R_e is the value given in table 1 of Paper XV. This $\sigma(R_e/8)$ is measured by co-adding all SAURON spectra contained within the aperture. The velocity dispersion is measured on that single spectrum using PPXF and adopting a Gaussian line-of-sight velocity distribution (keyword MOMENTS=2). Column (3): fraction of DM (dark over total) contained within an isosurface of volume $V = 4\pi R_e^3/3$ (a sphere of radius $r = R_e$ for spherical galaxies). Column (4): mass-to-light ratio (1σ random error of 6 per cent or 0.027 dex) of the stellar component (approximately within a sphere of radius $r \sim R_e$) in the SDSS *r*-band, for the best-fitting JAM model with NFW halo (model B in Paper XV) for the assumed distance and extinction of table 3 of Paper I. A description of the quality of the model fits is given in table 1 of Paper XV. The $(M/L)_{stars}$ and f_{DM} of models with qual < 2 there, should be used with caution. Column (5): mass-to-light ratio of the stellar population (1σ random error of 6 per cent or 0.027 dex) within $1R_e$, in the SDSS *r*-band, assuming a Salpeter IMF slope from 0.1 to 100 $M_\odot$ and using the models of Vazdekis et al. (2012). This value is mass weighted with equation (2) over the multiple populations fitted to the SAURON spectra with PPXF. Table 1 is also available from our project website http://purl.org/atlas3d.

Paper XV that in these variables the plane is extremely thin and follows the scalar virial equation $M_{JAM} \propto \sigma_e^2 R_e^{maj}$ within our tight errors. This implies that any projection of the plane contains the same amount of information, except for a change of coordinates. Instead of looking at the plane precisely face-on, we constructed special projections which correspond to physically meaningful and easy-to-interpret quantities.

Our selection of meaningful projections of the MP is shown in Fig. 1. We use as horizontal axis in all plots our main mass variable

$$M_{JAM} \equiv L \times (M/L)_{JAM} \approx 2 \times M_{1/2} \approx M_{stars}, \quad (3)$$

where $(M/L)_{JAM}$ is the total (luminous plus dark) dynamical M/L obtained using self-consistent JAM models, L is the total galaxy luminosity (both quantities were taken from table 1 of Paper XV) and $M_{1/2}$ is the total mass within a sphere of radius $r_{1/2}$ enclosing half of the total galaxy light, where $r_{1/2} \approx 1.33R_e$ (Hernquist 1990; Ciotti 1991; Wolf et al. 2010; Paper XV). Although the self-consistency assumption, where the total mass is proportional to the stellar mass, is not justified at large radii, it is accurate within the region where we have stellar kinematics (about $1R_e$). It was shown in Williams, Bureau & Cappellari (2010a) and in Paper XV that $(M/L)_{JAM}$ closely reproduces the total $(M/L)(r = R_e)$ inside a

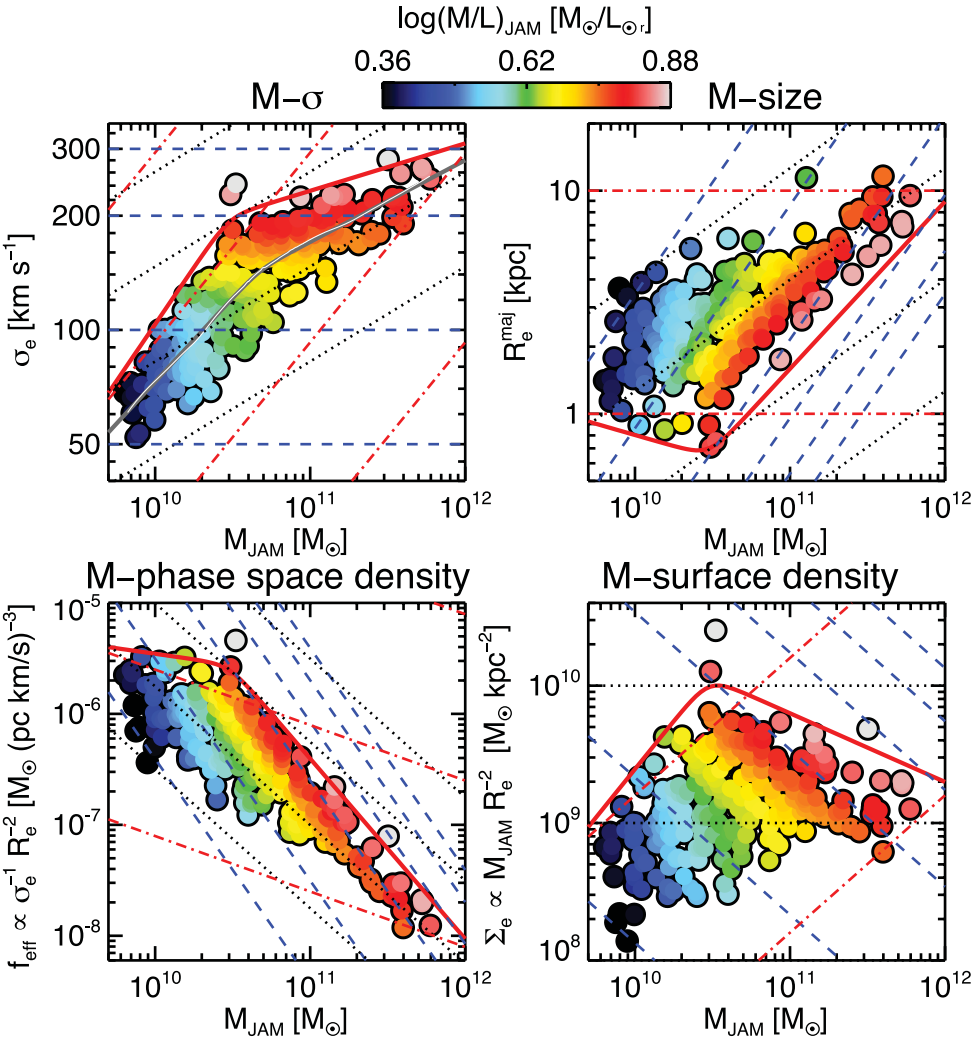

Figure 1. The MP and its projections. The top two panels show the two main projections of the MP in the ($M_{\rm JAM}$, $\sigma_{\rm e}$) and ($M_{\rm JAM}$, $R_{\rm e}^{\rm maj}$) coordinates. Overlaid are lines of constant $\sigma_{\rm e} = 50$, 100, 200, 300, 400, 500 km s^{-1} (dashed blue), constant $R_{\rm e}^{\rm maj} = 0.1$, 1, 10, 100 kpc (dot–dashed red) and constant $\Sigma_{\rm e} = 10^8$, 10^9, 10^{10}, 10^{11} M$_\odot$ kpc^{-2} (dotted black) transformed in different panels using the scalar virial relation $M_{\rm JAM} = 5.0 \times \sigma_{\rm e}^2 R_{\rm e}/G$. The observed ($M_{\rm JAM}$, $\sigma_{\rm e}$, $R_{\rm e}^{\rm maj}$) points follow the scalar virial relation so closely that the virial coordinates provide a unique mapping on these diagrams and one can reliably infer all characteristics of the galaxies from any individual projection. In each panel, the galaxies are coloured according to the (LOESS-smoothed) log (M/L)$_{\rm JAM}$, as shown in the colour bar at the top. The LOESS method tries to estimate the mean values of the underlying galaxy population, namely the values one should expect to obtain by averaging much larger galaxy samples. In all panels, the thick red line shows the same ZOE relation given by equation (4), again transformed in different panels according to the scalar virial relation. The thin white line in the top-left panel is a LOESS-smoothed version of the $M_{\rm JAM}$–$\sigma_{\rm e}$ relation, while the thick dark grey line is a double power-law fit (equation 5) with trends $M_{\rm JAM} \propto \sigma_{\rm e}^{2.3}$ and $M_{\rm JAM} \propto \sigma_{\rm e}^{4.7}$ below or above $\sigma_{\rm e} \approx 140$ km s^{-1}, respectively. While the top two panels contain different observable quantities, the bottom two panels merely apply a coordinate transformation to the quantities in the top two panels, to show the effective phase-space density $f_{\rm eff} \equiv 1/(\sigma\, {R_{\rm e}}^2)$ and effective mass surface density $\Sigma_{\rm e} \equiv M_{\rm JAM}/(2\pi {R_{\rm e}}^2)$. Two galaxies stand out for being significantly above the ZOE in the ($M_{\rm JAM}$, $\sigma_{\rm e}$) and ($M_{\rm JAM}$, $\Sigma_{\rm e}$) projections. The top one is NGC 5845 and the bottom one is NGC 4342.

sphere (actually an isosurface) with mean radius the projected half-light radius $R_{\rm e}$, derived using models which explicitly include DM. Different assumptions on the dark halo produce minor differences in (M/L)($r = R_{\rm e}$). Given that (M/L)($r = R_{\rm e}$) is nearly insensitive to the choice of the halo assumptions, we choose the self-consistent one, being the simplest.

As illustrated in Paper XV (see also Williams, Bureau & Cappellari 2009), most of the galaxies in our sample are consistent with having small fractions of DM within a sphere of radius $r = R_{\rm e}$, with a median value of just 13 per cent of DM within that radius for our standard models (B). This implies that $M_{1/2}$ is dominated by the stellar mass. For this reason $M_{\rm JAM}$ is a quantity that very closely represents and is directly comparable to the total stellar galaxy mass used in numerous previous studies. Stellar mass seems to relate well with galaxy properties and is often used to study galaxy formation (e.g. Kauffmann et al. 2003a,b; Hyde & Bernardi 2009b). The difference of our mass parameter is that it does not suffer from the uncertainties related to the stellar population models (e.g. Maraston et al. 2006; Conroy, Gunn & White 2009; Gallazzi & Bell 2009; Longhetti & Saracco 2009; Wuyts et al. 2009); moreover, it automatically includes the effects of a non-universal IMF (van Dokkum & Conroy 2010; Cappellari et al. 2012). Being a measure of the total enclosed mass within a spherical region, and thus being directly related to the dynamics, $M_{\rm JAM}$ is the ideal parameter to use in scaling relations. Note that $M_{\rm JAM}$, unlike mass determinations obtained via strong lensing, does not include the possible contribution of DM

along the cylinder parallel to the line of sight (Dutton et al. 2011b), which provides a useful additional constraint on DM at large radii, but complicates the interpretation of scaling relations in the galaxy centres.

In the top-left and top-right panels of Fig. 1, we show the projections of the MP along the ($M_{\rm JAM}$, $\sigma_{\rm e}$) and ($M_{\rm JAM}$, $R_{\rm e}^{\rm maj}$) projections, respectively. The colour in these diagrams represent the dynamical (total) M/L inside a sphere of radius $R_{\rm e}$. Three important results are clear from these plots.

(i) Both projections are equivalent and provide basically the same picture, apart from a coordinate transformation. This is expected from the tightness of the MP. Moreover, given that the MP nearly follows the scalar virial relation, the expression $M_{\rm JAM} = 5.0 \times \sigma_{\rm e}^2 R_{\rm e}/G$ (Cappellari et al. 2006) can be used to provide an accurate estimate of lines of constant $R_{\rm e}$ on the ($M_{\rm JAM}$, $\sigma_{\rm e}$) projection or the lines of constant $\sigma_{\rm e}$ on the ($M_{\rm JAM}$, $R_{\rm e}^{\rm maj}$) projection.

(ii) Galaxies define a clear zone of exclusion (ZOE) at small sizes or large densities, as already pointed out by Bender et al. (1992) and Burstein et al. (1997); however, we find a clear break in the ZOE at a mass $M_{\rm JAM} \approx 3 \times 10^{10}\,{\rm M}_\odot$ and two nearly power-law regimes above or below this value. The ZOE is approximated by

$$R_{\rm e}^{\rm maj} = R_{\rm e,b} \left(\frac{M_{\rm JAM}}{M_{\rm JAM,b}}\right)^{\gamma} \left[\frac{1}{2} + \frac{1}{2}\left(\frac{M_{\rm JAM}}{M_{\rm JAM,b}}\right)^{\alpha}\right]^{(\beta-\gamma)/\alpha}, \qquad (4)$$

with $R_{\rm e,\,b} = 0.7$ kpc, $\alpha = 8$, $\beta = 0.75$ and $\gamma = -0.20$. The relation has an asymptotic trend $R_{\rm e} \propto M_{\rm JAM}^{0.75}$ above $M_{\rm JAM,b} = 3.0 \times 10^{10}\,{\rm M}_\odot$, and a sharp transition into $R_{\rm e} \propto M_{\rm JAM}^{-0.20}$ below this break. The values were determined by simultaneously matching the observed boundary in the galaxy distribution in all MP projections (but see Fig. 2 for a quantitative definition). These values are nearly the same as those we already reported in Paper I (equation 4 there), using K-band luminosity in place of mass and 2MASS $R_{\rm e}$ instead of MGE ones. The maximum in the galaxy density at $M_{\rm JAM,\,b}$ that we infer from our sample is also clearly visible in much larger SDSS samples (e.g. fig. 2 of van Dokkum et al. 2008). This shows that the relation is valid for the general galaxy population. The ZOE relation of equation (4) can be converted into a ($M_{\rm JAM}$, $\sigma_{\rm e}$) one, or into other projections using the scalar virial relation $M_{\rm JAM} = 5.0 \times \sigma_{\rm e}^2 R_{\rm e}/G$. The corresponding trend becomes $\sigma_{\rm e} \propto M_{\rm JAM}^{0.6}$ ($M_{\rm JAM} \propto \sigma_{\rm e}^{1.67}$) below the break, which flattens to $\sigma_{\rm e} \propto M_{\rm JAM}^{0.125}$ ($M_{\rm JAM} \propto \sigma_{\rm e}^{8.0}$) above the break. The location of the break we find agrees with the value at which scaling relations of large sample of SDSS galaxies show a subtle deviation from a straight line (Hyde & Bernardi 2009a). Interestingly, the characteristic mass at the cusp also coincides with the value reported by Kauffmann et al. (2003b), as the fundamental dividing line between the two distinct families of passive and star-forming galaxies.

(iii) The contours of constant $({\rm M/L})_{\rm JAM}$ closely follow lines of constant $\sigma_{\rm e}$ in the ($M_{\rm JAM}$, $\sigma_{\rm e}$) projection (above $\sigma_{\rm e} \gtrsim 120\,{\rm km\,s^{-1}}$) and equivalently $R_{\rm e}^{\rm maj} \propto M_{\rm JAM}$ in the ($M_{\rm JAM}$, $R_{\rm e}^{\rm maj}$) projection. Comparable agreement is reached using lines parallel to the ZOE $R_{\rm e}^{\rm maj} \propto M_{\rm JAM}^{0.75}$. Neither mass $M_{\rm JAM}$, nor size $R_{\rm e}$ nor surface mass density $\Sigma_{\rm e}$ provide a comparably good approximation to the $({\rm M/L})_{\rm JAM}$ contours, although $\Sigma_{\rm e}$ provides a better approximation than the other two. This is consistent and explains the finding by Cappellari et al. (2006) that $\sigma_{\rm e}$ and not mass or luminosity is the best tracer of $({\rm M/L})_{\rm JAM}$. At lower $\sigma_{\rm e} \lesssim 120\,{\rm km\,s^{-1}}$, the $({\rm M/L})_{\rm JAM}$ contours start deviating from the lines of constant $\sigma_{\rm e}$ and tend to lie closer to lines of constant $M_{\rm JAM}$. Given that the M/L describes the deviations between the FP and the MP, this twist in the contours demonstrates that the FP is warped with respect to the MP, and explains the sensitivity of the FP parameters to the region included in the fit (D'Onofrio et al. 2008; Gargiulo et al. 2009; Hyde & Bernardi 2009b).

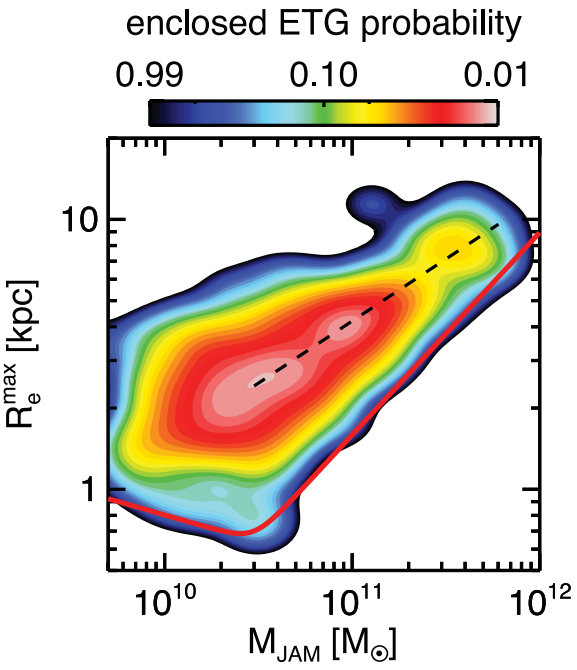

Figure 2. Probability density contours for ETGs on the M–size plane. Colours indicate the contours enclosing a given fraction of the total probability, with the outermost (lowest) contour enclosing 99 per cent of the total probability, above our survey mass limit ($M_{\rm JAM} \gtrsim 6 \times 10^9\,{\rm M}_\odot$). The thick red curve is the same as in Fig. 1 and provides a convenient approximation for the lowest 99 per cent contour. The dashed line indicates the relation $(R_{\rm e}^{\rm maj}/{\rm kpc}) = 4.2 \times [M_{\rm JAM}/(10^{11}\,{\rm M}_\odot)]^{0.46}$, which approximates the peak ridge-line of the ETG M–size distribution.

To quantitatively define the meaning of the ZOE, which is shown in various plots of this paper, we estimated the probability density underlying the set of discrete measurements for our galaxies in the M–size plane. For this, we used the kernel density estimator method. We adopted an Epanechnikov kernel and determined the optimal smoothing parameter in each dimension following Silverman (1986). The resulting estimate of the ETGs' density is shown in Fig. 2. The plot shows that the adopted functional form of the ZOE in equation (4) provides a convenient approximation of the lower contour enclosing 99 per cent of the ETG population, above our survey mass limit $M_{\rm JAM} \gtrsim 6 \times 10^9\,{\rm M}_\odot$. We argue that, for volume-limited samples, this line constitutes a more meaningful reference to define the lower limit of the sizes of the normal galaxy population than the mean M–size relation and its scatter (e.g. Shen et al. 2003). The reason is that the ZOE takes the galaxies mass function into account. Low-mass galaxies are more numerous than high-mass ones. This implies that, for a given rms scatter $\sigma_{R_{\rm e}}$, low-mass galaxies are more likely than high-mass galaxies to deviate more than $\sigma_{R_{\rm e}}$ from the mean M–size relation.

Two galaxies stand out for being significantly above the ZOE in the ($M_{\rm JAM}$, $\sigma_{\rm e}$) and ($M_{\rm JAM}$, $\Sigma_{\rm e}$) projections. The top one is NGC 5845 and the bottom one is NGC 4342. The two objects have very high surface brightness and consequently excellent kinematic and photometric data. They are genuine examples of dense objects in the nearby Universe. These two outliers were already presented in Cappellari (2011a) and their compactness was later discussed by Jiang et al. (2012). However, they have smaller masses

($M_{\rm JAM} \approx 3 \times 10^{10}\,{\rm M}_\odot$) than their high-redshift counterparts (Cimatti et al. 2008; van Dokkum et al. 2008).

In the top-left panel of Fig. 1, we overplot a version of the $M_{\rm JAM}$–$\sigma_{\rm e}$ relation which was adaptively smoothed using the one-dimensional locally weighted regression robust technique (dubbed LOESS[3]) of Cleveland (1979). The relation is equivalent to the Faber & Jackson (1976) but uses dynamical mass instead of luminosity. Like the ZOE, the mean $M_{\rm JAM}$–$\sigma_{\rm e}$ relation appears well approximated by a double power law of the form

$$\sigma_{\rm e} = \sigma_{\rm e,b} \left(\frac{M_{\rm JAM}}{M_{\rm JAM,b}}\right)^{\gamma} \left[\frac{1}{2} + \frac{1}{2}\left(\frac{M_{\rm JAM}}{M_{\rm JAM,b}}\right)^{\alpha}\right]^{(\beta-\gamma)/\alpha}, \quad (5)$$

with best-fitting parameters (excluding NGC 5845 and NGC 4342) $\log(M_{\rm JAM,b}/{\rm M}_\odot) = 10.675 \pm 0.090$, $\log(\sigma_{\rm e,b}/{\rm km\,s^{-1}}) = 2.153 \pm 0.031$, $\alpha = 8$, logarithmic slope $\beta = 0.215 \pm 0.027$ at large masses and $\gamma = 0.442 \pm 0.028$ at small masses. When the two power laws are written as a function of $\sigma_{\rm e}$, the trends become $M_{\rm JAM} \propto \sigma_{\rm e}^{1/\beta} = \sigma_{\rm e}^{4.65\pm0.58}$ for $\sigma_{\rm e} \gg 140\,{\rm km\,s^{-1}}$, and $M_{\rm JAM} \propto \sigma_{\rm e}^{1/\gamma} = \sigma_{\rm e}^{2.26\pm0.14}$ for $\sigma_{\rm e} \ll 140\,{\rm km\,s^{-1}}$.

In all panels of Fig. 1, and in all subsequent similar figures for other parameters, the measured $({\rm M/L})_{\rm JAM}$ have been adaptively smoothed using the LOESS technique, straightforwardly generalized to two dimension as in Cleveland & Devlin (1988). In all plots, we adopt a regularization factor $f = 0.6$, and a linear local approximation. To deal with the different scales of the axes and the elongated shape of the galaxy distributions, before applying LOESS we rotated and re-normalized the coordinates so that the ellipse of inertia of the galaxy distribution reduces to a circle in every projection[3]. This change of coordinates improves the definition of neighbouring points during the LOESS smoothing. By design the LOESS-smoothed maps try to remove observational errors and intrinsics scatter to estimate the mean values of the underlying galaxy population. The maps try to predict the mean values one would obtain via simple histograms of much larger samples of galaxies (see also discussion in Section 3.2). We do not show here the original data, as the scatter in $({\rm M/L})_{\rm JAM}$, projected along the $\sigma_{\rm e}$ coordinate, was already analysed in detail in Paper XV. Given that most of the variation in the smooth surface happens orthogonally to the constant $\sigma_{\rm e}$ lines, the scatter from the smooth surface of 27 per cent is nearly unchanged from the value of 29 per cent in the global (M/L)–$\sigma_{\rm e}$ relation, further confirming that most of the variation happens orthogonally to $\sigma_{\rm e}$.

In the bottom-left and bottom-right panels of Fig. 1, we show the effective phase-space density, defined following Hernquist, Spergel & Heyl (1993) as $f_{\rm eff} \equiv 1/(G\sigma_{\rm e} {R_{\rm e}}^2)$ and the mass surface density, defined as $\Sigma_{\rm e} \equiv M_{\rm JAM}/(2\pi {R_{\rm e}}^2)$. Note that, while we use $R_{\rm e}^{\rm maj}$ for the mass–size plane, one has to use $R_{\rm e}$ for $f_{\rm eff}$ and $\Sigma_{\rm e}$. The two bottom panels do not plot new data, but are obtained by rearranging the three variables shown in the top panels; however, they illustrate how the above trends relate to other physical quantities. In particular, the phase-space density is interesting because it can only decrease during collisionless galaxy mergers, due to Liouville's theorem (Carlberg 1986; Hernquist et al. 1993). Interestingly, the ZOE we find is nearly flat in $f_{\rm eff}$ below $M_{\rm JAM,b} = 3 \times 10^{10}\,{\rm M}_\odot$ (a value $\gamma = 1/3$ gives $f_{\rm eff} = {\rm const}$ in the virial case) and starts decreasing at larger masses, as one would expect when dry mergers start becoming more important.

[3] Our implementations CAP_LOESS_1D and CAP_LOESS_2D of the one-dimensional and two-dimensional LOESS method as used in this paper are available from http://purl.org/cappellari/idl

3.2 Stellar population indicators of $({\rm M/L})_{\rm pop}$

We have shown in Paper XV that the stellar matter dominates in the regions we study. If this is indeed the case, we would expect stellar population indicators of the $({\rm M/L})_{\rm pop}$ of the stellar population to closely follow the behaviour of the dynamical $({\rm M/L})_{\rm JAM}$. Before addressing this question with our own data, the reader is strongly encouraged to compare Fig. 1 to the right-hand panel of fig. 15 of Gallazzi et al. (2006), which shows the luminosity-weighted age versus the stellar mass in the $(\sigma, M_\star)$ projection. Even though our Fig. 1 uses dynamical quantities, which are measured via dynamical models, while Gallazzi et al. (2006) derives population from line strengths, the resemblance of the two plots is striking. This includes rather subtle details like the change of orientation of the contours, which in both cases tend to be horizontal above $\sigma \gtrsim 120\,{\rm km\,s^{-1}}$ and become nearly vertical at lower σ. This comparison already indicates a close link between $({\rm M/L})_{\rm JAM}$ and stellar population (mainly age), in broad agreement with Cappellari et al. (2006). Importantly, given that our sample is 100 times smaller than the one of Gallazzi et al. (2006), this comparison also provides a validation of the adopted LOESS technique, which appears to recover as expected the underlying distribution of galaxy properties from our much smaller galaxy sample. This comparison confirms that the various LOESS-smoothed plots in this paper should be interpreted as estimates of the average trends in the galaxy distribution we would observe if we had much larger samples of galaxies than we have in ATLAS$^{\rm 3D}$.

We now address the relation between dynamical and population M/L using our own data set and a different approach. Two main simple tracers of $({\rm M/L})_{\rm pop}$ have been proposed in the past: (i) the $B - R$ colour, which was shown by Bell & de Jong (2001) to trace $({\rm M/L})_{\rm pop}$ alone, for a wide range of metallicities and (ii) the stellar absorption line-strength index Hβ, which was shown to satisfy a similar property (fig. 16 of Cappellari et al. 2006) for a wide range of metallicities (see also Worthey 1994). Here, we adopt the Hβ determination for our ATLAS$^{\rm 3D}$ galaxies, as derived from the same very high S/N 'effective' SAURON spectra from which we derived $\sigma_{\rm e}$. The homogeneous extraction of the line-strength parameters for the ATLAS$^{\rm 3D}$ sample is given in McDermid et al. (in preparation). The parameters for the SAURON survey (de Zeeuw et al. 2002) subset of 48 galaxies was already given in Kuntschner et al. (2006). As choice of colour, we use the SDSS $g - i$ one, which is available for 223 ATLAS$^{\rm 3D}$ galaxies in SDSS DR8 and was shown by Gallazzi & Bell (2009) to provide on average the smallest uncertainties and the most stable results, among the SDSS bands.

The results are presented in Fig. 3 and show quite good agreement between simple population estimators of M/L and the dynamical one. Both Hβ (top panel) and colour (middle panel) are nearly constant along lines of constant $\sigma_{\rm e}$ as it was the case for Fig. 1. This confirms the fact that the key driver of the total dynamical $({\rm M/L})_{\rm JAM}$ is the stellar population. We do notice some systematic differences at the low-σ end, with the contours of constant $({\rm M/L})_{\rm JAM}$ not quite following the population trends. As the effect is visible both in colour and Hβ, we believe it is significant. It may be due to the presence of extended star formation episodes, which are expected to be more prevalent at low mass (Heavens et al. 2004; Thomas et al. 2005) and cause deviations from the simple one-to-one relations between population observables and M/L. The study of the relation between our parameters and the actual physical parameters of the population, like age, metallicity and abundance ratios, is presented in McDermid et al. (in preparation). Analysis of the stellar population parameters for the SAURON survey

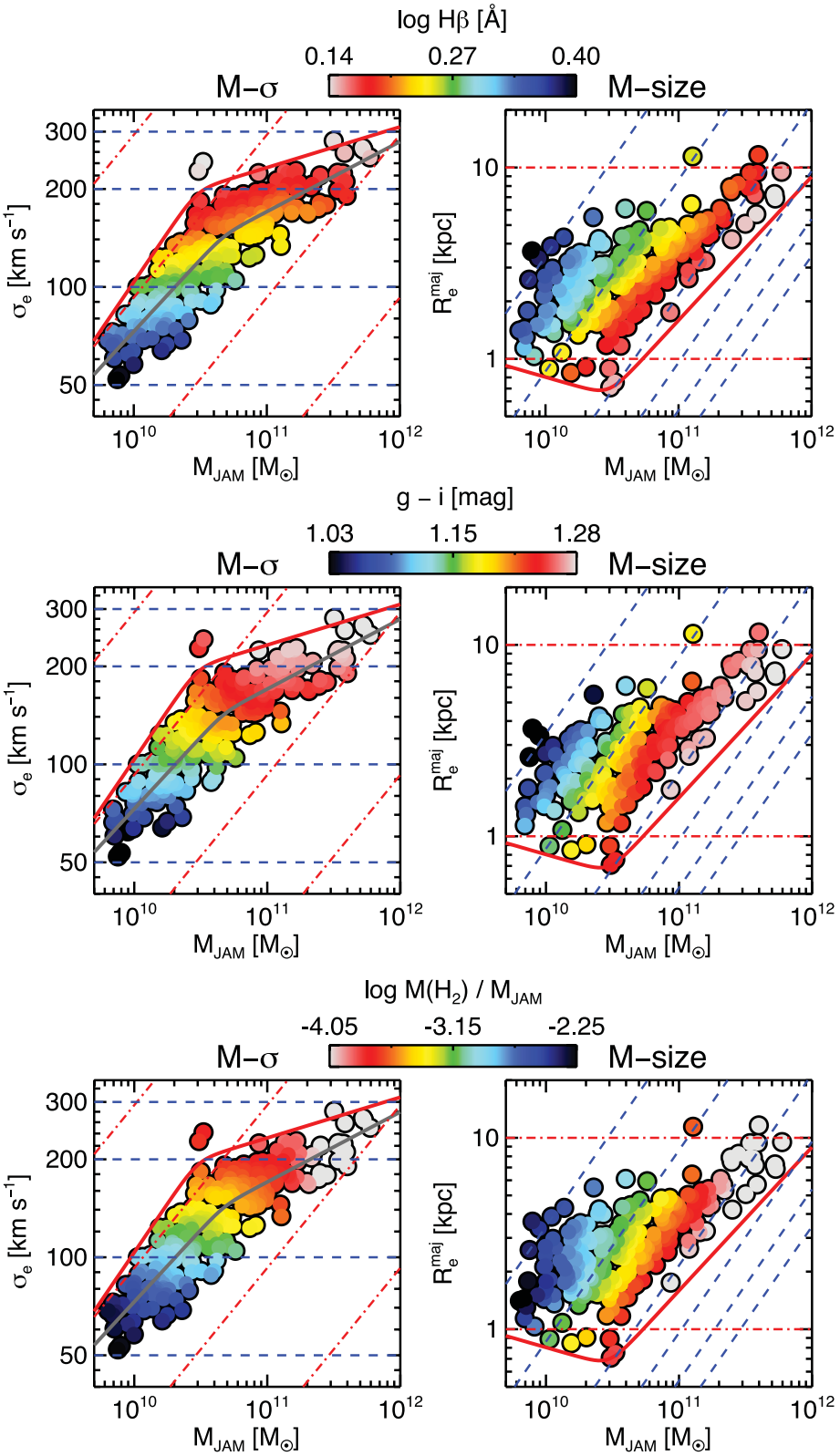

Figure 3. Indicators of the stellar population $(M/L)_{pop}$ on the MP. Top panels: same as in Fig. 1, with colours showing the log Hβ stellar absorption line-strength, from McDermid et al. (in preparation). Middle panels: same as in Fig. 1, with colours indicating the SDSS galaxy colour $g - i$. Bottom panels: same as in Fig. 1, with colour indicating the fraction of molecular hydrogen H_2 (from table 1 of Paper IV) with respect to M_{JAM}. All three indicators Hβ, $g - i$ and the H_2 fraction show a similar trends as the $(M/L)_{JAM}$ in the top panels of Fig. 1. This suggests that the stars dominate the region we observe and that the dynamical $(M/L)_{JAM}$ is driven by the stellar population, in agreement with the quantitative results via dynamical models in Paper XV.

(de Zeeuw et al. 2002) subset of 48 galaxies was already presented in Kuntschner et al. (2010).

In fig. 15 of Young et al. (2011, hereafter Paper IV), we showed that galaxies with the largest Hβ, and consequently younger mean ages, contain higher fractions of molecular hydrogen H_2 as traced by CO emission lines. The trend makes sense given that H_2 reservoir is expected to fuel star formation (see a more detailed discussion in Paper IV). Given the trend we observed for Hβ on the M–size plane, one should expect a similar trend for the H_2 fraction. This is indeed the case as presented in the bottom panel of Fig. 3, which shows the mass $M(H_2)$ as fraction of $M_{\rm JAM}$. Given that not all galaxies have a CO detection in Paper IV, we assigned to undetected galaxies a uniformly distributed random H_2 mass between zero and the quoted upper limit. A similar plot is obtained by assigning to all undetected galaxies a fixed mass $M(H_2) = 10^6\,M_\odot$ below our CO survey sensitivity, or by assigning the upper limit, showing that the trend does not depend critically on our treatment of the undetected galaxies. The plot shows that the molecular gas content, like other population indicators, also tends to follow contours of constant σ_e. However, some notable differences exist between this plot and the $(M/L)_{\rm JAM}$ or the Hβ ones. In particular, above the mass $M_{\rm JAM} \approx 2 \times 10^{11}\,M_\odot$, the likelihood of finding significant fractions of molecular gas seems to depend more on mass than σ_e. This mass is a characteristic one, where a number of other observables appear to change as we will show in Section 3.4.

3.3 Inferring bulge fractions from stellar kinematics

In the previous sections, we showed that galaxy properties follow smooth trends in the projections of the MP. We have seen that the dynamical M/L near the galaxy centre ($1R_e$) is driven by a variation of the stellar population (including IMF), with the dynamical M/L constituting an accurate tracer of the galaxy population! These trends distribute galaxies in the MP along lines of nearly constant σ_e on the $(M_{\rm JAM}, \sigma_e)$ plane, or equivalently $R_e^{\rm maj} \propto M_{\rm JAM}$ on the $(M_{\rm JAM}, R_e^{\rm maj})$ plane. In Paper I, we showed that the luminosity–size relation changes gradually with morphological type. Galaxy size decreases as a function of the bulge fraction as indicated by the morphological classification. We explained the size decrease as an increase of the bulge fraction between different morphological types. In Paper II and III, we showed that the vast majority of local ETGs is constituted by disc-like systems, the fast rotators, and in Cappellari et al. (2011b, hereafter Paper VII) we discussed how fast rotators morphologically resemble spirals with a variety of bulge fractions. We concluded that fast rotators simply constitute the end point of a smooth sequence of discs with increasing bulges, and this lead us to propose a fundamental change in our view of galaxy morphology (Paper VII). If this picture is correct, we should be able to find direct evidence for a systematic change in the bulge fraction, in the fast rotators class, while moving from the region of the MP populated by spiral galaxies towards the ZOE, dominated by the oldest and reddest ETGs, with the largest M/L. This is what we show in this section.

A detailed photometric bulge–disc decomposition of the unbarred galaxies subset of the ATLAS^{3D} sample is presented Krajnović et al. (2013b, hereafter Paper XVII). Although it provides a well-established definition of the bulge luminosity, it is a complex technique which depends on the extraction details and suffers from degeneracies. In particular, it is well established that, even assuming galaxies to be axisymmetric, the intrinsic stellar density cannot be uniquely recovered from the images unless galaxies are edge-on (Rybicki 1987; Gerhard & Binney 1996; van den Bosch 1997; Magorrian et al. 1998). For this reason, unless we knew galaxies to be accurately described by Sersic (1968) bulges and exponential discs (Freeman 1970), we should not expect to be able to uniquely decompose bulges and discs of inclined galaxies, as this would imply that we can uniquely infer their intrinsic densities. This is likely one of the reasons why we do not find trends in the bulge fraction (parametrized by the disc-over-total luminosity ratio D/T) of fast rotators on the M–size plane. An exception is the important and clear lack of discs above the characteristic $M_{\rm JAM} \gtrsim 2 \times 10^{11}\,M_\odot$.

In our survey, we have SAURON integral-field kinematics (Paper I) for all the galaxies in the sample. Here, we exploit that extra information to robustly infer the bulge fractions even at low inclinations. The reason why this is possible is because the kinematics retains information on the *flattening* of the galaxy components even at low inclinations, when no such information can be inferred from the images. In this situation, the photometric decomposition has to rely entirely on the radial profiles and the *assumption* of a specific functional form for the two components. The ability of the kinematics to uncover discs and bulges even at low inclination is illustrated in Fig. 4. For the plot, we constructed a model with a Sérsic bulge and an exponential disc. To have a representative model, we adopted the median ratio $R_e^{\rm disc}/R_e^{\rm bulge} \approx 5.2$ and the corresponding median Sérsic index for the bulges $n \approx 1.7$ (from table C1 of Paper XVII). We used the MGE_FIT_1D procedure[1] of Cappellari (2002) to obtain an accurate MGE fit to the one-dimensional profiles of both the bulge and the disc. We then assigned a typical intrinsic axial ratio $q_d = 0.2$ to the disc and $q_b = 0.7$ to the bulge. The Gaussian components of bulge and disc were then combined into a single MGE model that was used as input for a JAM dynamical model (Cappellari 2008), which provided a prediction for the second velocity moments $\langle v_{\rm los}^2 \rangle^{1/2}$. It was shown in Cappellari (2008), Scott et al. (2009) and for the full ATLAS^{3D} sample in Paper XV that the second moments calculated by the JAM method provide good predictions of the observed $V_{\rm rms} \equiv \sqrt{V^2 + \sigma^2}$ of real galaxies, where V is the mean stellar velocity and σ is the stellar velocity dispersion. The only free parameter in this model is the anisotropy in the (v_R, v_z) plane, which is parametrized by $\beta_z \equiv 1 - \sigma_z^2/\sigma_R^2$, for which we adopted a typical value $\beta_z = 0.25$ (Cappellari 2008). While keeping the bulge and disc parameters fixed, we varied their relative contribution D/T and we projected the models at different inclinations. Fig. 4 shows that the bulge fraction provides dramatic changes in the relative values of the $V_{\rm rms}$ in the galaxy centre with respect to its value at large radii. The presence of discs can still be inferred from the kinematics as a horizontal elongation in the $V_{\rm rms}$ maps, even for disc fractions as small as $D/T = 0.1$, and even for inclination as low as $i = 30^\circ$. Pure spheroids have $V_{\rm rms}$ maps roughly following the galaxy isophotes. Although the details of the $V_{\rm rms}$ maps are different for different galaxies, the qualitative trends shown in the figure are similar for quite different bulge and disc parameters.

In Fig. 5, we show the maps of $V_{\rm rms}$ actually observed with SAURON for a representative subsample of 40 galaxies in the ATLAS^{3D} sample, uniformly sampling the M–size plane (the full set of maps is shown in Paper XV). The plot shows that near the line $\sigma_e = 50\,{\rm km\,s^{-1}}$ all maps present the minimum of $V_{\rm rms}$, which is characteristic of pure disc galaxies. The minimum disappears around the line $\sigma_e = 100\,{\rm km\,s^{-1}}$, where the maps show the butterfly-like shape expected for galaxies with small bulges and dominant discs. For larger σ_e, the central peaks in $V_{\rm rms}$ become the norm and finally, near the line $\sigma_e = 200\,{\rm km\,s^{-1}}$, all galaxies show prominent $V_{\rm rms}$ peaks, indicating bulges as massive or more massive than the discs. The situation is, once more, qualitatively different above the characteristic mass $M_{\rm JAM} \gtrsim 2 \times 10^{11}\,M_\odot$. Above that mass,

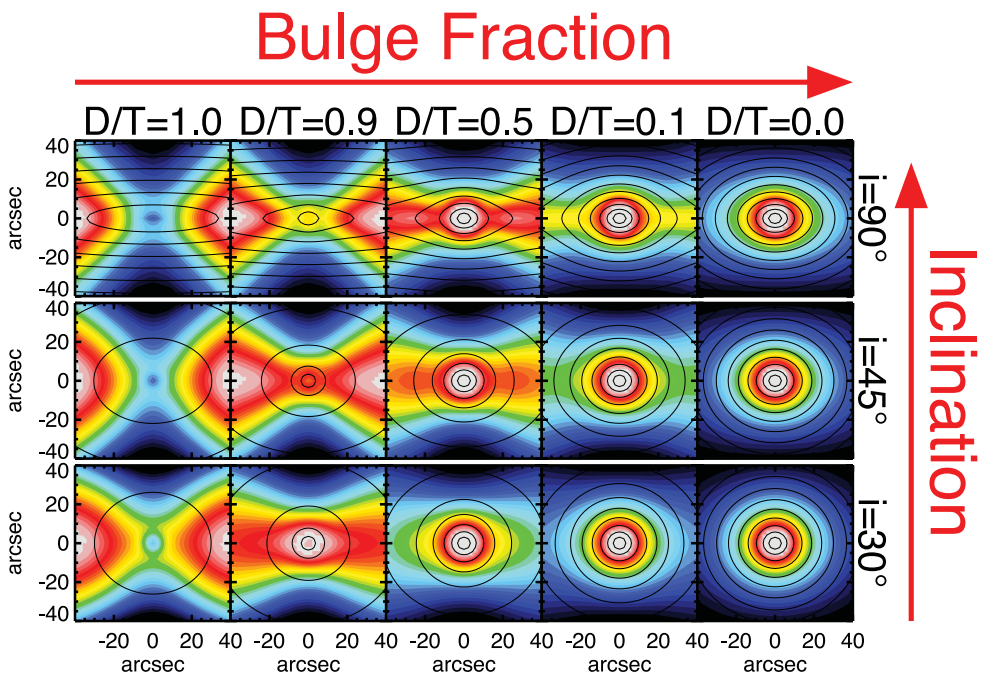

Figure 4. Inferring bulge fraction from stellar kinematics. The top panels show the prediction for the second velocity moment $\langle v_{\rm los}^2 \rangle^{1/2}$ using JAM dynamical models. This quantity approximates the observed $V_{\rm rms} \equiv \sqrt{V^2 + \sigma^2}$, where V is the mean stellar velocity and σ the velocity dispersion. The top panels show the predicted kinematics for edge-on realistic galaxy models with different bulge fractions, quantified by the disc-over-total luminosity parameter D/T. The middle and bottom panels show the same models, projected at different inclinations. The plots show that for any inclination (i) an increase of the bulge fraction produces a peak in the central $V_{\rm rms}$; (ii) the presence of a disc produces an horizontal elongation of the $V_{\rm rms}$ contours.

the $V_{\rm rms}$ maps lack the horizontal $V_{\rm rms}$ elongation. This indicates they do not have discs and consist of pure spheroid, in agreement with the bugle–disc decompositions of Paper XVII.

To try to generalize the qualitative results from the maps of Fig. 5, we need to encode the key information on the shape of the $V_{\rm rms}$ maps into a simple parameter that can be extracted for the full volume-limited ATLAS^{3D} sample. We found that the following simple approach is sufficient.[4] We quantified the variety of shapes in Fig. 4 by simply measuring the ratio between the central velocity dispersion $\sigma(R_{\rm e}/8)$ (given in Table 1) measured with PPXF (with keyword MOMENTS=2) within the commonly used circular aperture of radius $R = R_{\rm e}/8$ and our reference $\sigma_{\rm e}$ (given in table 1 of Paper XV), measured within the 'effective' isophote of major axis $R_{\rm e}^{\rm maj}$. The distribution of the $\sigma(R_{\rm e}/8)/\sigma_{\rm e}$ ratio on the MP projections is shown in Fig. 6. It shows that the ratio still approximately follows lines of constant $\sigma_{\rm e}$ (or even better lines parallel to the slightly more shallow ZOE $R_{\rm e}^{\rm maj} \propto M_{\rm JAM}^{0.75}$). This confirms that the trends in the bulge fractions we saw from the maps of the galaxy subset in Fig. 5 are also valid in a statistical sense for the whole ATLAS^{3D} sample. It demonstrates that at given mass, $\sigma_{\rm e}$ traces the bulge fraction, which in turn appear as the main driver for the trends in M/L, population parameters and molecular gas content that we observe.

Interestingly, the plot also shows a slight decrease in the $\sigma(R_{\rm e}/8)/\sigma_{\rm e}$ ratio above the characteristic mass $M_{\rm JAM} \gtrsim 2 \times 10^{11}\,{\rm M}_\odot$. This value coincides with the characteristic scale in ETGs above which galaxies start to be rounder (Tremblay & Merritt 1996; van der Wel et al. 2009b), nearly all have flat (core/deficit) central surface brightness profiles (Faber et al. 1997; Graham & Guzmán 2003; Ferrarese et al. 2006; Lauer et al. 2007b), they deviate from power-law colour–magnitude relations (Baldry et al. 2004; Ferrarese et al. 2006; Bernardi et al. 2011) and are embedded in massive X-ray haloes (Kormendy et al. 2009; Sarzi et al. 2013, hereafter Paper XIX).

In the bottom panel of Fig. 6, we show for comparison the distribution of the Sersic (1968) index n (from Paper XVII) on the MP projection. These values were obtained by fitting a single Sérsic function $I(R) \propto \exp(-kR^{1/n})$ to the entire galaxy profile and do not necessarily provide good descriptions of the galaxies. However, this kind of approach is routinely used to characterize sizes and morphologies of large galaxy samples (e.g. Blanton et al. 2003; Shen et al. 2003) or to study galaxies scaling relations at high redshift (e.g. Trujillo et al. 2007; Cimatti et al. 2008; van Dokkum et al. 2008). The plot clarifies that the Sérsic index behaves quite differently from the others galaxy indicators and in particular it is weakly sensitive to the bulge fraction. The global Sérsic index tends to vary along lines of nearly constant mass rather than $\sigma_{\rm e}$. Unlike $\sigma_{\rm e}$, the global Sérsic index is not a good predictor of galaxy properties. The plot also clarifies that defining ETGs as having $n > 2.5$ (e.g. Shen et al. 2003) tends to select ETGs above the characteristic mass $M_{\rm JAM} \approx 3 \times 10^{10}\,{\rm M}_\odot$, while defining genuine nearby elliptical galaxies as having $n > 4$ tends to select objects above the characteristic mass $M_{\rm JAM} \approx 2 \times 10^{11}\,{\rm M}_\odot$.

3.4 Variations of galaxy intrinsic flattening and rotation

Our dynamical modelling effort provides the unique opportunity of having the galaxy inclination for the entire ATLAS^{3D} sample

[4] For more quantitative results, one could try to break the degeneracy of the photometric bulge–disc decomposition approach by fitting simultaneously both the galaxy images, e.g. with a Sérsic+exponential model, and the $V_{\rm rms}$ maps with the corresponding JAM prediction for different (i, β_z). Although interesting and in principle straightforward, this goes beyond the scope of this paper

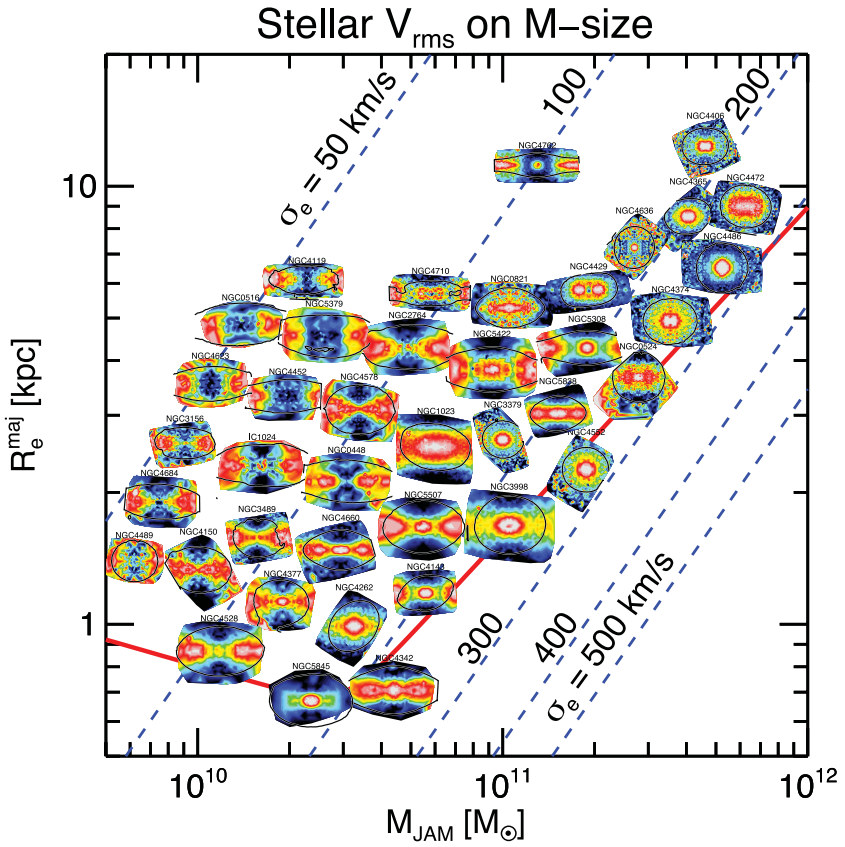

Figure 5. Observed $V_{\rm rms} \equiv \sqrt{V^2+\sigma^2}$ maps on the M–size plane. All galaxies are oriented with their kinematical major axis $\rm PA_{kin}$ (from Paper II) horizontal. A characteristic isophote is indicated by the thick black contour. The plot shows that (i) near the $\sigma_{\rm e} \approx 50\,{\rm km\,s^{-1}}$ line, galaxies show a drop in the central $V_{\rm rms}$ characteristic of pure discs (see Fig. 4); (ii) near the $\sigma_{\rm e} \approx 100\,{\rm km\,s^{-1}}$ line the maps show a butterfly-like shape characteristic of galaxies with small bulges; (iii) near the $\sigma_{\rm e} \approx 200\,{\rm km\,s^{-1}}$ line the maps show strong peaks of $V_{\rm rms}$, indicative of bulges as massive or more massive than the discs, but horizontal elongations due to discs are still present; (iv) above the characteristic mass $M_{\rm JAM} \gtrsim 2\times10^{11}\,{\rm M_\odot}$ no horizontal elongations of $V_{\rm rms}$ are seen any more, indicating galaxies are pure spheroids. The latter finding agrees with the classification of the objects as slow rotators (Paper III) and the lack of discs in their bulge–disc decomposition (Paper XVII).

of galaxies (from table 1 of Paper XV). We verified that the JAM inclination agrees with the one inferred from the geometry of the dust, for 26 galaxies with regular dusts discs (see also Cappellari 2008). We further verified that we can recover with JAM models the inclination of simulated galaxies that resemble typical objects in our sample (Paper XII). Although one should not expect the inclination to be reliable for every individual galaxy, it is expected to be accurate for most of our sample. The inclination allows us to recover the intrinsic shape of individual objects. The de-projection is done using the ellipticity ε of the outer isophote, measured in Paper II at radii typically around $4R_{\rm e}$, at the depth limit of the SDSS photometry. At these radii, when a disc is present, the ellipticity is representative of the outer discs and is insensitive to the possible presence of a bulge. We then computed the intrinsic ellipticity assuming an oblate spheroid geometry as (Binney & Tremaine 2008)

$$\varepsilon_{\rm intr} = 1 - \sqrt{1+\varepsilon(\varepsilon-2)/\sin^2 i}. \quad (6)$$

The results of the de-projection is shown in the top panels of Fig. 7. Contrary to all previous diagrams presented so far, the distribution of the intrinsic ellipticity for ETGs on the MP shows a completely different trend. Few galaxies stand out in the top-right corner for being nearly round, with average intrinsic ellipticity $\varepsilon_{\rm intr} \approx 0.3$. These galaxies are all located above the same characteristic mass $M_{\rm JAM} \gtrsim 2\times10^{11}\,{\rm M_\odot}$, where other observables indicated a transition in galaxy properties. This result confirms previous statistical studies of ETGs' shapes (Tremblay & Merritt 1996; van der Wel et al. 2009b; Bernardi et al. 2011). Below this characteristic mass, the mean ellipticity drops dramatically and sharply to about $\varepsilon_{\rm intr} \approx 0.6$, characteristics of discs. This galaxy-by-galaxy shape de-projection confirms a similar result on their shape distribution inferred via Monte Carlo simulations from the distribution of fast rotators ETGs on the (λ_R, ε) diagram, suggesting that fast rotators have a typical intrinsic ellipticity $\varepsilon_{\rm intr} \approx 0.7$ (fig. 15 in Paper III). It also agrees with a statistical inversion of their shape (Weijmans et al. 2013, hereafter Paper XXIII). This agreement also seems to confirm the reliability of the inclinations derived via the JAM models. The result strongly confirms our previous conclusions that fast rotators as a class are disc like (Paper II, III, VII). At the lowest mass range ($M_{\rm JAM} \lesssim 10^{10}\,{\rm M_\odot}$), near the ZOE, there seems to be a marginal decrease of $\varepsilon_{\rm intr}$. The significance or reality of this feature is however unclear.

A similar trend as for the intrinsic shape is seen in the bottom panel of Fig. 7 for the optical morphology, as quantified by the T-type parameter from HyperLeda (Paturel et al. 2003). Above $M_{\rm JAM} \gtrsim 2\times10^{11}\,{\rm M_\odot}$ nearly all galaxies are classified as ellipticals ($T < -3.5$), consistently with the fact that galaxies in this mass range are genuine spheroids. While below this mass both E and S0 classification are present, due to the morphological misclassification of inclined discs for genuine spheroidal ellipticals.

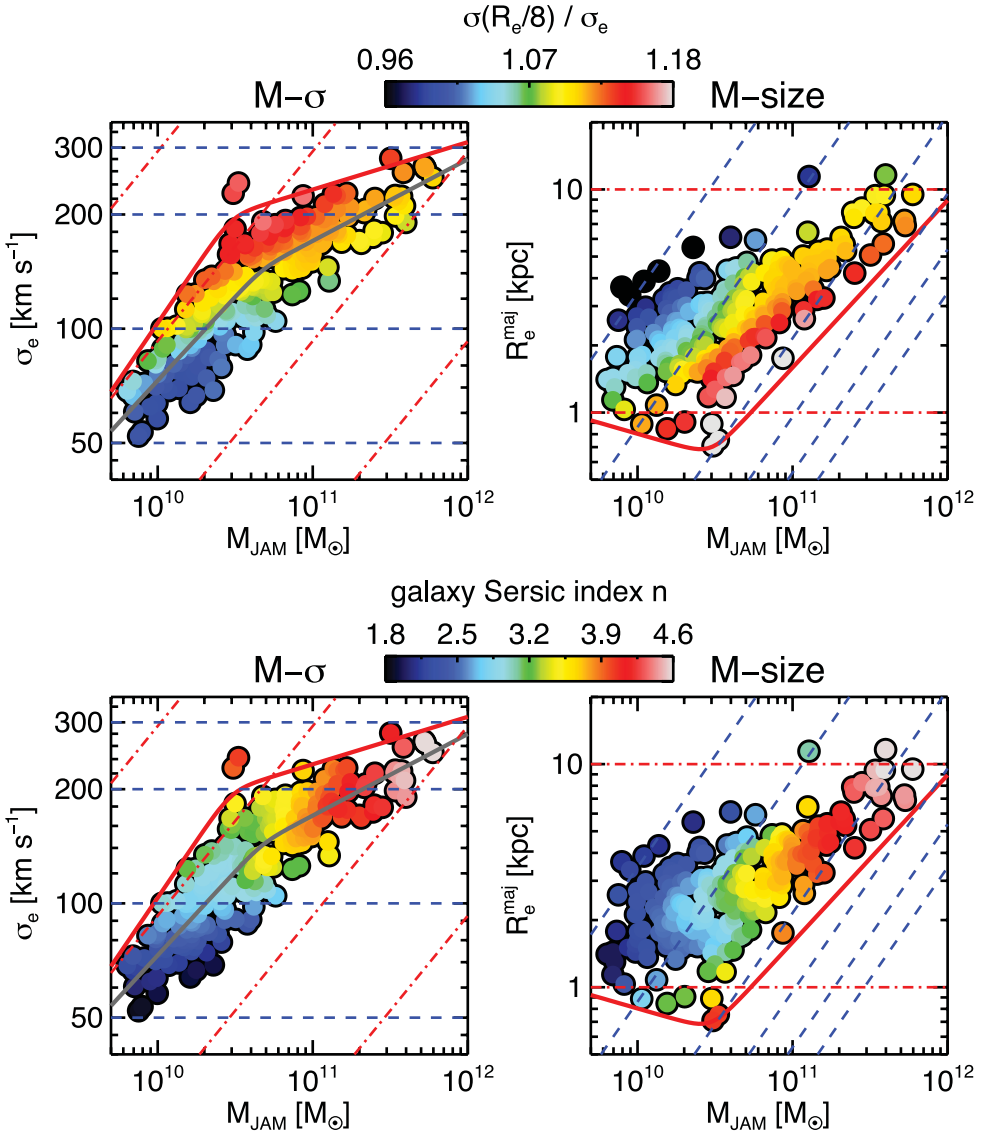

Figure 6. Galaxy concentration on the M–size plane. Top panels: same as in Fig. 1 for the ratio $\sigma(R_e/8)/\sigma_e$, between the velocity second moment measured within a circular aperture of radius $R = R_e/8$ and the second moment σ_e (which includes both rotation and random motions) within the 'effective' isophote of semimajor axis R_e^{maj}. As shown in Fig. 4, this quantity is related to the bulge fraction, and is weakly sensitive to projection effects. Like for $(M/L)_{JAM}$, the variation of this parameter tends to follow lines of constant σ_e, or equivalently $R_e^{maj} \propto M_{JAM}$, or even better, it follows lines parallel to the ZOE above its break. Note the slight decrease of $\sigma(R_e/8)/\sigma_e$ above the characteristic mass $M_{JAM} \gtrsim 2 \times 10^{11}\,M_\odot$. Bottom panels: for comparison this shows the variation of the global Sérsic index n for the galaxies, as measured in Paper XVII. n does not follow lines of constant σ_e and it is not a good empirical predictor of galaxy properties. Above $M_{JAM} \gtrsim 2 \times 10^{11}\,M_\odot$ galaxies tend to have the value $n \gtrsim 4$, which is often associated with pure spheroids.

The round and massive objects that stand out from the shape distribution above $M_{JAM} \gtrsim 2 \times 10^{11}\,M_\odot$ are the prototypical slow rotators, which also stand out for their extremely low specific stellar angular momentum λ_R (Emsellem et al. 2007), as shown in Paper III. In the top panel of Fig. 8, we plot the distribution of the intrinsic λ_R, which was approximately obtained from the observed one given in Paper III by de-projecting the observed velocity to an edge-on view, using the best-fitting inclination from the JAM models. The plot shows a clear transition in the average λ_R of the galaxy population at the mass $M_{JAM} \gtrsim 2 \times 10^{11}\,M_\odot$. Above this mass essentially all ETGs are slow rotators, while below this mass the population is dominated by fast rotators, although some slow rotators are still present. The bottom panel of Fig. 8 plots the angular momentum parameter λ_R for the slow-rotator ETGs only. The slow rotators are found to populate a rather narrow sequence on the MP, with a small range of Σ_e. This plot shows that not all slow rotators are the same. In fact, there is a clear trend of decreasing rotation with increasing mass as noted in Paper III, or possibly a transition around $M_{JAM} \approx 10^{11}\,M_\odot$, which is similar to the characteristic mass defined by other observables. This confirms that the massive slow rotators above our characteristic mass are indeed special and may have formed differently from the rest. Although we tend to cover a smaller field with our kinematics for the largest galaxies, the qualitative difference in the kinematics for the most massive slow rotators is already clearly visible from the velocity fields (Paper II) and it is not due to the difference in the field coverage. A strong indication that indeed the most massive slow rotators are special also comes from the fact that they all appear to have cores, while the less massive ones are core-less (Krajnović et al. 2013a, hereafter Paper XXIV).

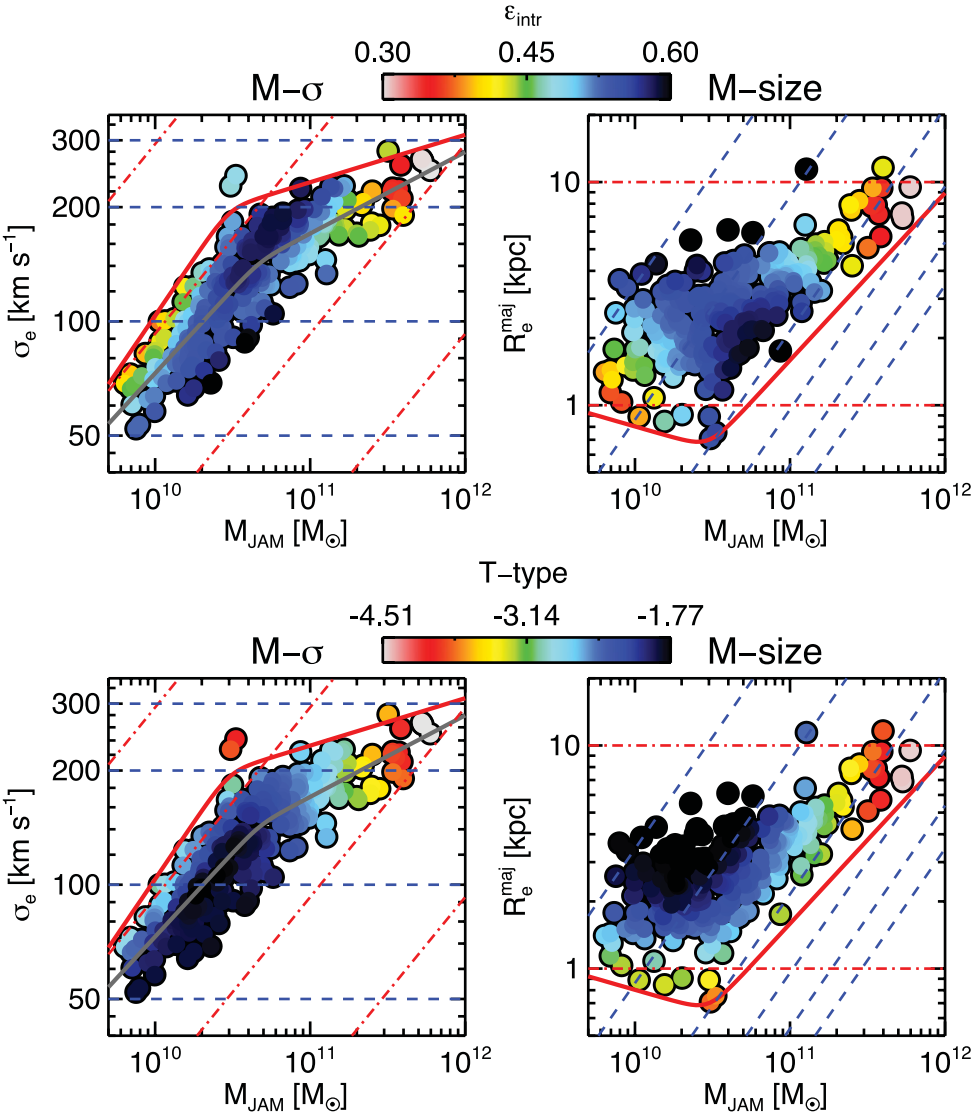

Figure 7. Intrinsic shape and morphology. Top panels: same as in Fig. 1, with colours indicating the intrinsic ellipticity $\varepsilon_{\rm intr}$ of the galaxies outer regions, computed by de-projecting the observed ellipticity ϵ at large radii (Paper II) using the inclination inferred from the JAM models (Paper XV). Except again for the special region above $M_{\rm JAM} \gtrsim 2 \times 10^{11}\,{\rm M}_\odot$, all the rest of the ETGs have on average the flattening of discs $\varepsilon \approx 0.6$ close to the result from the Monte Carlo approach of Paper III, which suggests fast rotators have a typical intrinsic ellipticity $\varepsilon_{\rm intr} \approx 0.7$ and the statistical inversion in Paper XXIII. Bottom panels: same as in the top panel, with colours indicating the galaxy morphology as quantified by the T-type parameter from HyperLeda. For $M_{\rm JAM} \gtrsim 2 \times 10^{11}\,{\rm M}_\odot$ galaxies are invariably classified as E ($T < -3.5$), while both E and S0 classifications are present at lower masses.

In summary, the distribution of galaxy properties on the ($M_{\rm JAM}$, $\sigma_{\rm e}$) and ($M_{\rm JAM}$, $R_{\rm e}^{\rm maj}$) projections of the MP can be understood as due to a smooth variation in the bulge mass as already suggested in fig. 4 of Paper I. The connection between bulge mass and galaxy properties, and the close link between ETGs and spiral galaxies is further illustrated in Fig. 9, which includes the location of the spiral galaxies of the ATLAS$^{\rm 3D}$ parent sample (Paper I) together with the ETGs. The masses of spiral galaxies was approximately estimated assuming a fixed $M/L_K = 0.8\,{\rm M}_\odot/{\rm L}_\odot$, which ensures agreement between $M_{\rm JAM}$ and the K-band luminosity at the lowest masses. The plot shows that ETGs' properties vary smoothly with those of spiral galaxies. Galaxies with negligible bulges are almost invariably star forming and classified as late spirals. Galaxies with intermediate bulges can still form stars and be classified as early spirals, or can be fast-rotator ETGs. But the galaxies with the most massive bulges, as indicated by their largest concentration or $\sigma_{\rm e}$ are invariably ETGs. They have the largest M/L (Fig. 1), the reddest colours, smallest Hβ and lowest molecular gas fraction (Fig. 3), but are still flat in their outer parts, indicating they have discs (Fig. 7) and generally still rotate fast (Fig. 8). An exception are galaxies with masses $M_{\rm JAM} \gtrsim 2 \times 10^{11}\,{\rm M}_\odot$, which stand out for being nearly round, and non-rotating. Above this characteristic mass essentially no spirals are present.

Also included in Fig. 9 is the approximate location of dwarf ETGs (spheroidals) and dwarf irregulars (Im) galaxies in the mass–size diagram. The dwarf ETGs' parameters were taken from Gavazzi et al. (2005), Ferrarese et al. (2006), Misgeld et al. (2008) and Misgeld et al. (2009), while the Im parameters come from Kirby et al. (2008). The plot shows that the spheroidal galaxies lie along the continuation of the M–size relation for spiral galaxies and naturally connect to the region of fast-rotator ETGs with the lowest M/L, young ages and small bulges. One should keep in mind that, while

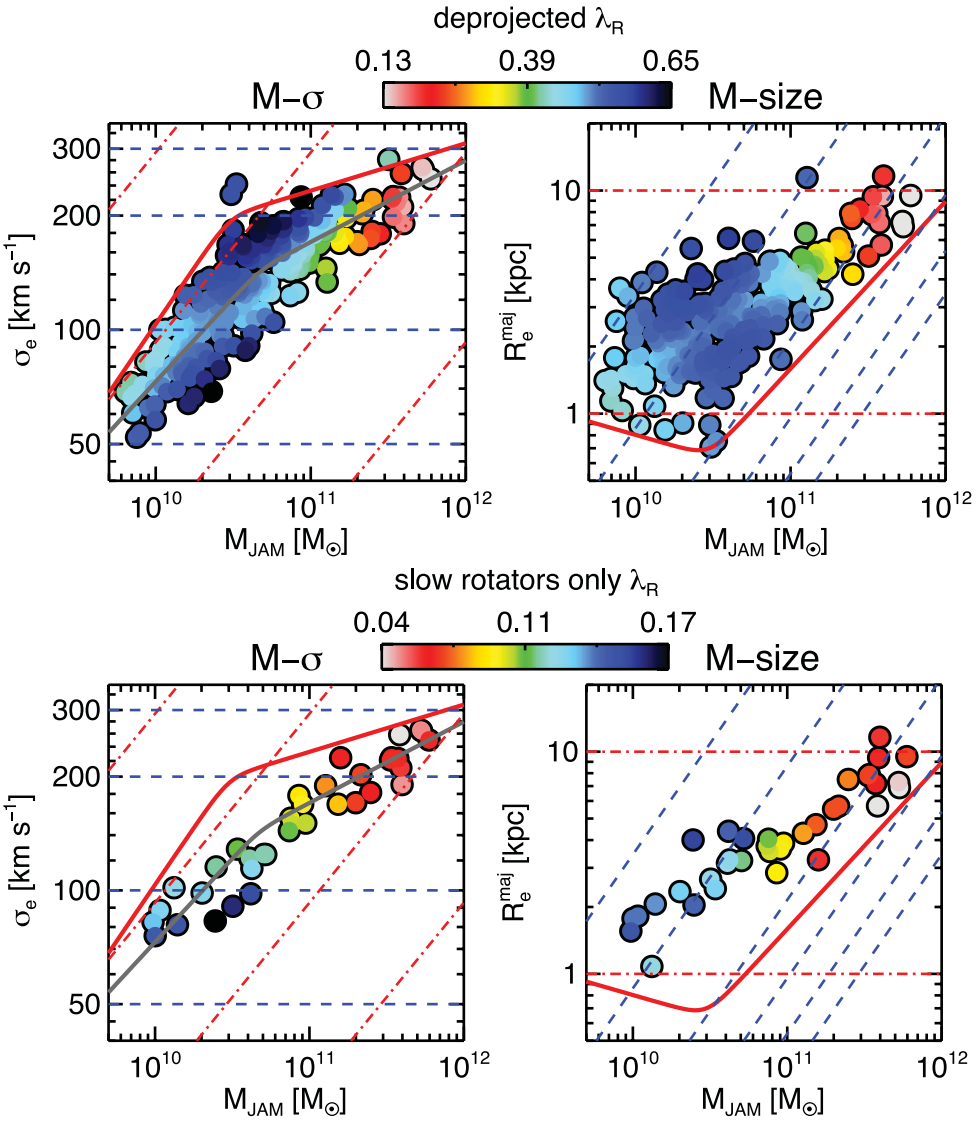

Figure 8. Galaxy stellar rotation on the MP projections. Same as in Fig. 1, with colours indicating the specific angular momentum parameter λ_R of Emsellem et al. (2007), as given in Paper III, de-projected to an edge-on view according to the JAM inclination (Paper XV). Top panels: all ATLAS^{3D} galaxies are included. A clear transition in the mean galaxy rotation is evident above $M_{\rm JAM} \gtrsim 2 \times 10^{11}\,{\rm M}_\odot$, with the population becoming entirely dominated by slow rotators. Bottom panels: only the slow rotators are shown. They seems to define a sequence in the MP, and they show a decrease in the rotation especially above $M_{\rm JAM} \gtrsim 2 \times 10^{11}\,{\rm M}_\odot$, where only the slow rotators with the lowest λ_R are present.

the galaxies parameter space is fully sampled above the mass selection limit $M_{\rm stars} \gtrsim 6 \times 10^9\,{\rm M}_\odot$ of the ATLAS^{3D} survey, below this limit the data are heterogeneous. A much improved coverage of these parameters will soon be provided by the Next Generation Virgo Cluster Survey (Ferrarese et al. 2012) as shown in Ferrarese (2012).

4 SYSTEMATIC VARIATION OF THE IMF

Although the IMF variation could have been included among the other galaxy observables described in Section 3, we keep the IMF in a separate section for a more detailed coverage than for the other observables. In recent months, there has been a large amount of interest on the IMF variation. Before describing our new ATLAS^{3D} results, in the following section we provide a summary of this rapidly evolving field. To clarify the significance and robustness of the various recent claims, including our own, we place particular emphasis on the modelling assumptions that went into the various studies.

4.1 Summary of previous IMF results

4.1.1 IMF of the Milky Way

The stellar IMF describes the distribution of stellar masses when the population formed. Nearly every aspect of galaxy formation studies requires a choice of the IMF to calculate predictions for galaxy observables (Kennicutt 1998). For this reason, the IMF has been subjected to numerous investigations since the first determination more than half a century ago finding it has the form (Salpeter 1955)

$$\zeta(m) \propto m^x = m^{-2.3}, \tag{7}$$

for $m > 0.4\,{\rm M}_\odot$, where m is the stellar mass.

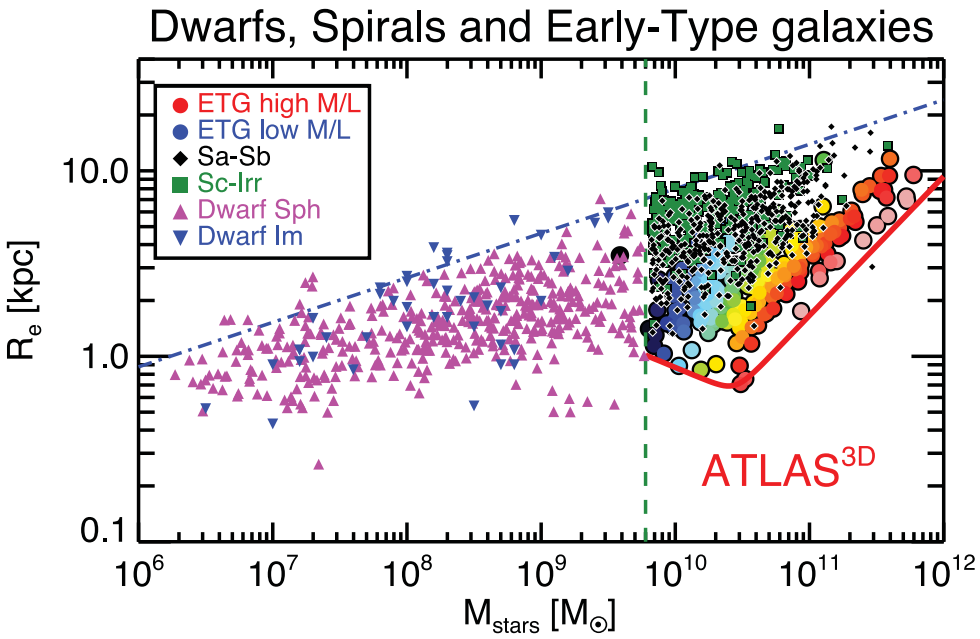

Figure 9. The mass–size distribution for dwarfs, spiral galaxies and ETGs. The ETGs of the ATLAS^{3D} sample are coloured according to their $(M/L)_{JAM}$ as in Fig. 1. This plot however also includes the approximate location of spiral galaxies in the ATLAS^{3D} parent sample, where masses are obtained from *K*-band luminosities, scaled to match M_{JAM} (a plot using luminosities rather than masses for both ETGs and spirals was shown in fig. 4 of Paper I). Early spirals (Sa-Sb: $T \leq 4$) are indicated by the black filled diamonds, while late spirals (Sc-Irr: $T > 4$) are shown with the filled green squares. Late spirals are larger than ETGs, while early spirals overlap with the ETGs with low M/L. There are essentially no spirals in the region of the oldest and reddest ETGs, which have the largest M/L. This illustrates the fact that the increase of the bulge is required to make a galaxy old and red and consequently produce the largest M/L. No spirals are present above the characteristic mass $M_{JAM} \gtrsim 2 \times 10^{11}\,M_\odot$. Also included in the plot is the approximate location of dwarf ETGs (Sph: magenta filled up triangles, from Gavazzi et al. 2005; Ferrarese et al. 2006; Misgeld, Mieske & Hilker 2008; Misgeld, Hilker & Mieske 2009) and dwarf irregulars (Im: blue filled down triangles, from Kirby et al. 2008). These are only shown below the mass limit of the volume-limited ATLAS^{3D} survey (vertical dashed line). For reference, the dash–dotted blue line shows the relation $(R_e/\mathrm{kpc}) = 8 \times [M_{stars}/(10^{10}\,M_\odot)]^{0.24}$.

In the Milky Way, the IMF can be measured via direct stellar counts. Various determination in different environments lead to the finding of a remarkable universality in the shape of the IMF (Kroupa 2002), with the IMF being well described by the Salpeter logarithmic slope $x = -2.3$ for $m \geq 0.5\,M_\odot$ and a shallower one at smaller masses $x = -1.3$ for $m < 0.5\,M_\odot$ (Kroupa 2001). The Milky Way IMF can also be described by a log-normal distribution (Chabrier 2003), which has some theoretical justification. However, the Kroupa and Chabrier IMFs are essentially indistinguishable from an observational point of view (Kroupa et al. 2013). Recent IMF results were reviewed by Bastian, Covey & Meyer (2010) who concluded no clear evidence existed for a non-universal IMF in our galaxy and among different galaxies.

4.1.2 IMF from ionized gas emission or redshift evolution

In external galaxies individual stars cannot yet be resolved down to sufficiently small masses for IMF studies. Some indirect constraints on the slope of the IMF above $\sim$1 $M_\odot$ can be obtained by combining observations of the Hα equivalent widths, which is related to the number of ionizing photons, with the galaxy colour, which is a function of the galaxy stellar population (Kennicutt 1998). Using this technique, Hoversten & Glazebrook (2008) inferred a variation of the IMF with more massive galaxies having a more top-heavy IMF than Salpeter, a result confirmed under the same assumptions (Gunawardhana et al. 2011) by the Galaxy and Mass Assembly (GAMA) survey (Driver et al. 2011). A similar result was found using the ratio between the Hα and ultraviolet fluxes by Meurer et al. (2009), who further pointed out that surface density is more important than mass in driving the IMF trend.

Constraints on the IMF can also be obtained by comparing the local ($z = 0$) stellar mass density to the integral of the cosmic star formation history (SFH). Wilkins et al. (2008) and Davé (2008) find that the local stellar mass density is lower than the value obtained from integrating the cosmic SFH, assuming that all the stars formed with a Salpeter IMF. They propose a time-variable IMF to reconcile the observations.

Alternative constraints on the IMF can be obtained by studying the evolution of the M/L normalization in samples of galaxies as a function of redshift, for example from the evolution of the tilt and normalization of the FP with redshift (Renzini & Ciotti 1993). From these constraints and from the metal abundance in the clusters' interstellar medium, Renzini (2005) concluded that elliptical galaxies as a class must have an IMF close to Salpeter for stellar masses $m > 1\,M_\odot$, while the IMF must flatten at lower masses, similar to the Kroupa IMF.

A related approach was employed by van Dokkum (2008) who used the ratio of luminosity evolution to colour evolution of massive galaxies in clusters to constrain the IMF. He originally concluded that the IMF must be top heavy at high redshift in apparent agreement with some theoretical model predictions (Zepf & Silk 1996; Chiosi et al. 1998). However, this result was recently revised with better data and models to conclude that the IMF above $m > 1\,M_\odot$ is actually not inconsistent with a Salpeter slope (van Dokkum & Conroy 2012).

4.1.3 Lensing or dynamics IMF constraints for external spirals

A more direct approach to constraining the variation of the IMF in galaxies consists of measuring the mass of the stars, and comparing this with the predictions of stellar population models. It is important to stress however that this method does not measure the shape of the IMF directly, but only its overall mass normalization. The method can only verify whether the stellar mass in a certain region within a galaxy is consistent with that due to a stellar population with a certain assumed IMF. Moreover, these methods do not measure the same IMF one can infer via direct stellar counts in star clusters. They measure instead the stellar mass distribution due to the superposition of the IMFs from a large number of star clusters in the galaxy as well as the IMFs coming from the accretion of satellite galaxies during the galaxy hierarchical growth. As pointed out by Kroupa & Weidner (2003), even if the IMF was universal in every cluster in a galaxy, the integrated galactic IMF would be different from the universal one, due to the non-uniform mass distribution of star clusters (see Kroupa et al. 2013 for an in-depth discussion). Hierarchical evolution complicates the picture even further. For these reason, when we state e. g. that 'a galaxy is consistent with the Salpeter IMF', we simply imply, consistently with all previous similar studies, that 'the galaxy has the same stellar M/L of a stellar population with the given age and metallicity (and abundances), and the Salpeter IMF'.

The first convincing constraint on the IMF of external galaxies was obtained for a sample of 21 spiral galaxies, using the kinematics of the gas. Bell & de Jong (2001) concluded that *if the IMF is universal*, a sensible assumption at the time, it cannot have the Salpeter form, but it must be lighter, consistently with Kroupa type. The result was later confirmed, still using gas kinematics, for a sample of 34 bright spiral galaxies by Kassin, de Jong & Weiner (2006).

The need for a light IMF was inferred for the Einstein Cross spiral galaxy gravitational lens system (Huchra et al. 1985) by both van de Ven et al. (2010) and Ferreras et al. (2010), and for another spiral lens galaxy by Suyu et al. (2012). As part of the DiskMass Survey (Bershady et al. 2010), which obtained integral-field stellar kinematics of a sample of 30 spiral galaxies, a light IMF was indirectly confirmed from the submaximality of the discs (Bershady et al. 2011). As part of the Sloan WFC Edge-on Late-type Lens Survey (SWELLS) survey of spiral lens galaxies (Treu et al. 2011), the need for a light IMF for most spiral galaxies was also found from the analysis of 20 strong gravitational lens (Brewer et al. 2012).

An inconsistency of the Salpeter IMF normalization for low-mass galaxies was also inferred by Dutton et al. (2011a), using simple galaxy models with a bulge and a disc, trying to reproduce global trends for a large sample of galaxies extracted from the SDSS.

In summary, there is good agreement on the fact that spiral galaxies as a class must have a normalization lighter than Salpeter and similar to Kroupa/Chabrier. This is a robust result due to the fact that a Salpeter IMF would overpredict the total mass in the galaxy centres. It is unclear whether some spiral galaxies have a Salpeter IMFs, and of course whether the IMF varies within the galaxies themselves, as claimed by Dutton et al. (2013).

4.1.4 Lensing or dynamics IMF constraints on early types

An early attempt at constraining the IMF of 21 elliptical galaxies, using detailed spherical dynamical models including DM, found a general consistency between the stellar $(M/L)_{stars}$ and the one of the population $(M/L)_{pop}$, using the Kroupa IMF, but could not accurately constrain the IMF normalization due to large observational errors (Gerhard et al. 2001). A large study of SDSS elliptical galaxies using fixed spherical Hernquist galaxy models with dark haloes (Padmanabhan et al. 2004) found a mass excess over the predictions of stellar population models with a fixed IMF, increasing with luminosity. This was interpreted as an increase of the DM fraction. A similar conclusion was reached by Zaritsky, Gonzalez & Zabludoff (2006) while studying the fundamental manifold. A caveat of those studies was the use of homologous stellar profiles or approximate assumptions to study systematic variations in the heterogeneous galaxy population.

To overcome these limitations, as part of the SAURON project (de Zeeuw et al. 2002), we constructed self-consistent axisymmetric models reproducing in detail both the photometry and the state-of-the-art integral-field stellar kinematics data (Emsellem et al. 2004) for 25 ETGs (Cappellari et al. 2006). The assumption that mass follows light is not accurate at large radii, but it is a good assumption for the region where kinematics is available ($\lesssim 1 R_e$), and provides accurate measurements of the total (luminous plus dark) M/L within a sphere of radius $r \approx R_e$ (see Paper XV). The resulting improvement in the M/L accuracy and the removal of systematic biases allowed us to strongly confirm that 'the total and stellar M/L clearly do not follow a one-to-one relation. DM is needed to explain the differences in M/L (if the IMF is not varying)' (see fig. 17 of Cappellari et al. 2006). Although DM seemed, at the time, still a more natural explanation of our observations, if the measured trends are re-interpreted as an IMF variation, they would imply an IMF heavier than Salpeter for some of the oldest objects. That study also concluded that *if the IMF is universal* it must have a mass normalization as low as Kroupa IMF, consistently with the results for spiral galaxies, otherwise the stellar mass would overpredict the total one for a number of galaxies. A similar finding was obtained by Ferreras, Saha & Burles (2008) using gravitational lensing of nine elliptical galaxies extracted from the Sloan Lens ACS (SLACS) survey (Bolton et al. 2006).

A number of subsequent studies used approximate models reproducing the velocity dispersion of large galaxy samples to study DM and IMF variations in galaxies. Tortora et al. (2009) used spherical isotropic models with Sersic (1968) profiles to reproduce the large velocity dispersion compilation by Prugniel & Simien (1996). Graves & Faber (2010) used the FP of ETGs from SDSS data. Schulz, Mandelbaum & Padmanabhan (2010) combined weak lensing measurements in the outer parts to SDSS velocity dispersion determination, using spherical Jeans models with a Hernquist profile. All three studies confirmed the existence of a mass excess which increases with mass. They all preferred a DM trend to explain the observations, although they could not exclude the IMF variation alternative.

Grillo et al. (2009) compared stellar population masses, derived from multicolour photometry, to the total masses, inside the Einstein radius of the lenses, published by the SLACS team (Bolton et al. 2008a). He assumed for all galaxies the average DM fraction determined for some of the galaxies by Koopmans et al. (2006) and Gavazzi et al. (2007), which were based on spherical models assuming a single power-law total mass and a Hernquist (1990) (or Jaffe 1983) stellar profile. From this comparison, Grillo et al. (2009) concluded that elliptical galaxies prefer a Salpeter rather than Kroupa/Chabrier IMF. The same result was found when comparing stellar dynamical masses for galaxies in the Coma cluster by Thomas et al. (2009), which includes DM haloes with fixed NFW profiles, to stellar population masses (Grillo & Gobat 2010).

However, given that the dynamical masses were determined assuming a fixed NFW profile, the conclusion depended on the correctness of that assumption. A recent reanalysis of the 16 Coma galaxies by Thomas et al. (2011), still assuming an NFW dark halo profile, interpreted the M/L excess in massive galaxies as more likely due to DM, although their results are not inconsistent with a Salpeter IMF instead. The same conclusions were reached by Wegner et al. (2012) for eight galaxies in Abell 262.

The SLACS team analysed their data assuming all galaxies in their sample can be approximated by homologous spherical and isotropic systems with a Hernquist (1990) (or Jaffe 1983) profile. In Treu et al. (2010), they further assumed a spherical NFW profile for the DM, with fixed slope and only mass as free parameter. Given that the enclosed total (luminous plus dark) mass inside the Einstein radius is essentially fixed by the lens geometry, under these assumptions the central velocity dispersion is a unique function of the profile of the total mass distribution, which in this case is defined by a single parameter: the ratio between the stellar and DM components. Comparing the stellar mass from the lens model to the one from population, based on multicolour photometry (Auger et al. 2009), they found that the data prefer a Salpeter-like normalization of the IMF. Auger et al. (2010a) used the SLACS data and the same spherical Hernquist models but, instead of allowing for free haloes for different galaxies, they assumed the same IMF and the same haloes, following the trends predicted by the abundance matching technique (Moster et al. 2010), for the entire ensemble population. They still assumed NFW haloes but explored both adiabatically contracted (Gnedin et al. 2004) and not contracted haloes. They concluded that the data favour a Salpeter-like normalization of the IMF over a lighter Kroupa/Chabrier form.

Although ground-breaking, the analyses of the SLACS data depended on some non-obvious assumptions. Grillo et al. (2009) had assumed a fixed DM fraction, as well as a power-law form for the total mass. Treu et al. (2010) result depended on the assumption of a fixed NFW halo slope, as the authors acknowledged concluding that 'the degeneracy between the two (IMF or DM) interpretations cannot be broken without additional information, the data imply that massive ETGs cannot have both a universal IMF and universal DM haloes', in agreement with previous dynamical analyses. Auger et al. (2010a) result depended on assuming the halo mass from the abundance matching techniques. This led the authors to conclude that 'better constraints on the star formation efficiency must be obtained from the data in order to draw definitive conclusions about the role of a mass-dependent IMF relative to CDM halo contraction'.

Other independent studies of the same SLACS data did not exclude an IMF variation, but did not confirm the need for a Salpeter IMF to explain the observations. Tortora et al. (2010) reached this conclusion using spherical Hernquist isotropic models like Treu et al. (2010) and Auger et al. (2010a), but could not explain the reason for the disagreement. A similar study was also performed by Deason et al. (2012). They showed that the trend in the galaxies enclosed masses can be explained by a toy model similar to the one adopted by Auger et al. (2010a), but with a universal Kroupa IMF. Deason et al. (2012) study however did not fit the galaxies stellar velocity dispersion, which could be a reason for the difference in the results. Barnabè et al. (2011) re-analysed 16 SLACS galaxies using axisymmetric, rather than spherical, dynamical models, and describing the galaxy images in detail, rather than assuming fixed Hernquist profiles. Their models are fitted to integral-field stellar kinematics, instead of a single velocity dispersion. They find that the data are consistent with both a Kroupa or a Salpeter IMF, in agreement with the early study by Ferreras et al. (2008).

An additional limitation all previous analyses of the full SLACS sample was the assumption that all galaxies in their sample could be described by homologous spherical Hernquist distributions. These models ignore known systematic variations of galaxy morphology with mass (e.g. Caon, Capaccioli & D'Onofrio 1993; Graham & Guzmán 2003; Kormendy et al. 2009; see also Fig. 6). Moreover, real ETGs, even in the mass range of the SLACS survey, are dominated by fast-rotating discs (Paper II; Paper III), some of which are clearly visible in the SLACS photometry. Disc galaxies are not well described by spherical single-component models. It is unclear whether galaxy models that do not reproduce neither the kinematics nor the photometry of the real galaxies under study can be trusted at the $\sim$10 per cent level that is required for IMF studies. Possible systematic biases in the results are however difficult to estimate. A reanalysis of the excellent SLACS data set using more realistic and flexible models would seem to be the best way to clarify the situation and provide a consistent picture. This approach has already been demonstrated by Barnabè et al. (2012) for a single galaxy using the JAM method (Cappellari 2008) in combination with the lensing analysis. One should finally consider that lensing studies measure the mass within cylinders along the line of sight. The recovered stellar mass depends on both the assumed DM profile in the centre and at large radii (Dutton et al. 2011b).

An simple assumption on the DM content of ETGs was made by Dutton, Mendel & Simard (2012a). They selected the most dense galaxies from a large sample of SDSS galaxies and constructed spherical isotropic models to reproduce their stellar velocity dispersion. They assumed that the total dynamical M/L of this set of galaxies is the same as the stellar one. Comparing the inferred mass to the one from stellar population they concluded that the galaxies require on average a Salpeter IMF normalization. This study still depends on the spherical approximation. Moreover, it is unclear to what accuracy the zero DM assumption is verified even for the densest galaxies. Nonetheless, this study confirms that, unlike spiral galaxies, the densest ETGs are not inconsistent with a Salpeter IMF.

In summary, the two result on which nearly all previously discussed studies agree are as follows: (i) the *total* M/L in the central regions of galaxies ($r \lesssim R_e$) does not follow the M/L inferred assuming a universal IMF; (ii) less massive galaxies, especially spiral ones, *require* an IMF normalization lighter than Salpeter and consistent with Kroupa like, while more massive and dense ones allow for a Salpeter IMF. Indications were found for the Salpeter IMF to be actually *required* for massive ellipticals (Grillo et al. 2009; Auger et al. 2010a; Treu et al. 2010; Dutton et al. 2012a). However, these conclusions depend on assuming the knowledge of either the DM fraction or the slope, or the mass of the dark halo. An exception is the recent work by Sonnenfeld et al. (2012), which modelled a rare elliptical with two concentric Einstein rings, and concluded for a Salpeter IMF. More similar objects would be needed to draw solid conclusions. Not all studies agreed on the requirement for a Salpeter IMF, even when analysing the same SLACS data (Ferreras et al. 2008; Tortora et al. 2010; Barnabè et al. 2011; Deason et al. 2012). It seems that this situation could be resolved by the use of more realistic models.

4.1.5 Systematic IMF variation in galaxies

A breakthrough in IMF studies was provided by the work by van Dokkum & Conroy (2010), further strengthened in van Dokkum & Conroy (2011). Contrary to the previously described set of

dynamical and lensing works, they looked for evidences of IMF variation in subtle IMF-sensitive spectral features of the near-infrared region of galaxy spectra, in particular the Wing–Ford band. In this way, their study did not suffer from the dependence on the halo assumptions. Although the spectral technique has been around for decades (e.g. Spinrad & Taylor 1971), only the availability of reliable stellar population models has made the approach sufficiently accurate for IMF studies (Schiavon, Barbuy & Bruzual 2000; Cenarro et al. 2003). van Dokkum & Conroy (2010) analysed the IMF of eight massive ellipticals, from stacked spectra. They used new population models that allow for a variation of the detailed abundance patterns of the stars (Conroy & van Dokkum 2012a) to distinguish abundance from IMF variations. They concluded that the observed spectra required a bottom-heavy, dwarf-rich IMF. Combining their finding with the previous results on the IMF of spiral galaxies they tentatively concluded that 'taken at face value, our results imply that the form of the IMF is not universal but depends on the prevailing physical conditions: Kroupa like in quiet, star-forming discs and dwarf-rich in the progenitors of massive elliptical galaxies'.

Our relatively large and well-selected ATLAS^{3D} sample and high-quality integral-field stellar kinematics appeared well suited to resolve the halo degeneracies of previous dynamical and lensing analyses and test the claims from the spectral analysis. Contrary to previous large studies, we adopted an axisymmetric modelling method which describes in detail both the individual galaxy images using the MGE technique (Emsellem et al. 1994; Cappellari 2002) and the richness of our two-dimensional kinematics (Cappellari 2008), thus avoiding the possible biases of previous more approximate approaches. For the first time, thanks to the tighter constraints to the models provided by the two-dimensional data, our study could leave *both* the halo slope and its mass as free parameters. The halo slope is allowed to vary in a range which includes both the flat inner haloes predicted by halo expansion models (e.g. Governato et al. 2010), and the steep ones predicted by adiabatic halo contraction (e.g. Gnedin et al. 2004). Our models also explicitly include the galaxy inclination and anisotropy as free parameters, although the latter is still assumed to be constant in the region where we have data. The parameters are estimated in a Bayesian framework with a maximum ignorance (flat) prior on the parameters.

We showed that even in this relatively general case the models required a variation of the IMF to reproduce the data (Cappellari et al. 2012), unless there are major flaws affecting all available stellar population models. We additionally tested a variety of sensible modelling assumptions on the halo, some of which had already been employed by previous studies. However, this time our models accurately described the photometry and kinematics of the real galaxies. We confirmed that a non-universal IMF is required under all those halo assumption. The similarity is due to the fact that in all cases DM contributes just about 10–20 per cent to the total mass within $1R_e$, so that it cannot explain an observed M/L excess of up to a factor of 2–3.

Our ATLAS^{3D} sample includes a larger range of masses than previous lensing studies. Not only we could quantify the IMF normalization of ETGs as a class, but we showed that the IMF normalization varies systematically within the ETG population, as a function of the stellar $(M/L)_{stars}$. The IMF was found consistent with Kroupa/Chabrier like at low $(M/L)_{stars}$ and heavier that Salpeter at large $(M/L)_{stars}$. This finding bridges the gap between the Kroupa-like IMF determinations in spirals and the evidence for a Salpeter like or heavier in ETGs. This should be expected given the parallelism and continuity in physical parameters between early-type and spiral galaxies as emphasized in our 'comb' morphological diagram (Paper VII). ETGs at low $(M/L)_{stars}$ in fact completely overlap with the region populated by spiral galaxies on the mass–size projection of the MP (Fig. 9). Our result also reconciled the apparent disagreement between studies claiming that ETGs include cases with Kroupa/Chabrier normalization and those claiming that Salpeter is required.

Although, unsurprisingly, the cleanest IMF trend in Cappellari et al. (2012) was obtained by simply comparing the dynamical and population M/L, a trend with velocity dispersion σ_e was also presented. This is a natural consequence of existence of the (M/L)–σ correlation (Cappellari et al. 2006; van der Marel & van Dokkum 2007). In particular, Cappellari et al. (2012) (their fig. 2) showed an IMF trend, with significant scatter, going from a Kroupa/Chabrier to a Salpeter IMF within the range $\log_{10}(\sigma_e/\mathrm{km\ s^{-1}}) \approx 1.9$–$2.5$, with a gradual variation in between.

A flurry of papers have appeared in subsequent months from independent groups, all in agreement on the existence of a systematic IMF variation in galaxies. Spiniello et al. (2012) used the models of Conroy & van Dokkum (2012a) in combination with SDSS spectra and inferred a variation of the IMF from sodium and titanium-oxide absorptions, which correlate with velocity dispersion (also illustrated by Zhu, Blanton & Moustakas 2010). A similar result was inferred by Ferreras et al. (2013), also from SDSS spectra, but using the population models by Vazdekis et al. (2012). Smith, Lucey & Carter (2012) studied the Wing-Ford absorption for galaxies in the Coma Cluster. They find that their galaxy spectra are best reproduced by a Salpeter IMF and detect a weak IMF trend with metallicity, but do not find an IMF trend with velocity dispersion. Conroy & van Dokkum (2012b) detected a systematic trend of the IMF, versus either σ or metallicity, using both optical and near-infrared spectral features. A key difference from other spectral studies is that they were able to rule out, in a Bayesian framework, a variation of element abundances as the origin of the empirical trends.

Dutton et al. (2012b) showed that it is sufficient to assume the knowledge of the halo mass and fit galaxy scaling relations via approximate spherical galaxy models, to infer a systematic variation of the IMF. Similarly, Tortora, Romanowsky & Napolitano (2013) tested a set of different assumption on the dark halo, using approximate spherical Sersic (1968) galaxy models to fit the SDSS velocity dispersion of a large galaxy sample. Some of the halo assumptions were also included in Cappellari et al. (2012) with more detailed dynamical models, producing consistent results. Although these results still depend on simple approximations and on assumption on the halo, they illustrate that many different halo assumptions, motivated by theoretical models, all lead to the same conclusion of a systematic IMF variation.

In summary, after years of debate on whether the IMF or the DM were responsible for the observed disagreement between stellar population and dynamical or lensing indicators, a consensus seems to have emerged, from dynamical, lensing and spectral arguments, on a systematic IMF variation with the IMF becoming heavier with M/L, mass or velocity dispersion. It is time to investigate IMF trends against other observables, which we do in the following section.

4.2 IMF variation on the MP

In Cappellari et al. (2012), we presented a systematic trend between the IMF and the stellar $(M/L)_{stars}$ derived using axisymmetric JAM models including a dark halo. The IMF was parametrized by the IMF mismatch parameter $\alpha \equiv (M/L)_{stars}/(M/L)_{Salp}$ (in

the notation of Treu et al. 2010), where $(M/L)_{Salp}$ was derived from full spectral fitting as summarized in Section 2.3. Different population approaches were also tested there, producing less clean trends but consistent results. The $(M/L)_{Salp}$ normalization depends on the adopted lower and upper mass cut-offs for the IMF in the population models. The models we use (Vazdekis et al. 2012) adopt standard lower and upper mass cut-offs for the IMF of 0.1–100 $M_\odot$, respectively. $(M/L)_{Salp}$ further depends on whether the gas lost by the stars during the early stages of their evolution is retained in the central regions we observe or is recycled into stars or expelled at large radii. Evidence suggests that the gas is not retained in significant quantities within $1R_e$, neither in ionized or hot X-ray emission form (Sarzi et al. 2010), nor as a cold component (Paper IV). If all the gas was retained it would increase $(M/L)_{Salp}$ by up to 30–40 per cent (Maraston 2005), making population M/L overpredicting total dynamical M/L even for a light Kroupa/Chabrier IMF, for a number of galaxies.

A careful determination of the population M/L for a fixed IMF was recently provided for 35 galaxies in our sample by Conroy & van Dokkum (2012b). They employed different models (Conroy & van Dokkum 2012a) from the ones we adopted (Vazdekis et al. 2012) and used them to fit an independent set of spectra, spanning a larger wavelength range than the SAURON ones. In Fig. 10, we compare the two determinations of M/L (allowing for an arbitrary offset in the absolute normalization). Assuming all measurements have comparable errors, the observed scatter between the 35 values is consistent with an error of just 6 per cent in $(M/L)_{Salp}$. This error is consistent with the error of 7 per cent predicted by Gallazzi & Bell (2009) when optimal spectra information is available. This gives confidence that our population $(M/L)_{Salp}$ are robust and any trend we observe is not due to the details of our population modelling approach.

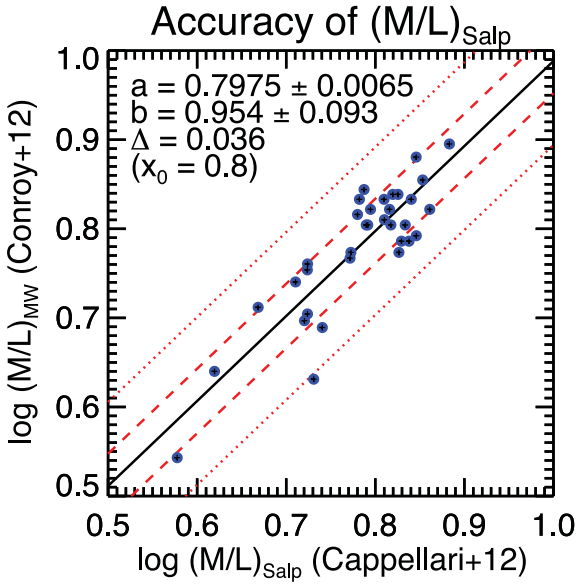

Figure 10. Testing the accuracy of $(M/L_r)_{Salp}$ against the completely independent determination of $(M/L_K)_{MW}$ from Conroy & van Dokkum (2012b), which use a different population modelling software and different spectra with a longer wavelength range than the SAURON ones. Assuming all measurements have comparable errors, the observed scatter between the 35 values is consistent with a 1σ error $\Delta/\sqrt{2}$ of 6 per cent in $(M/L_r)_{Salp}$. The $(M/L_K)_{MW}$ values were multiplied by a constant factor to approximately account for the differences in the photometric band and IMF.

Cappellari et al. (2012) showed that consistent IMF trends are found for a variety of different assumptions on the dark halo, as well as for the most general one (model D) which leaves both the halo slope and mass as free parameters, with only an upper limit on the halo slope, derived from model predictions of halo contraction (Gnedin et al. 2011) (see Paper XV for a description of the models). The similarity in $(M/L)_{stars}$ for the different models is due to the fact that in all cases the data allow for a small fraction of DM within the region where the kinematics are available ($\sim 1R_e$), with the most general model implying a median DM fractions of just 10 per cent. Given the similarity of the different approaches, here we adopt as reference the $(M/L)_{stars}$ values obtained with an NFW halo, with halo mass as free parameter (model B). This choice also makes it easy to compare our results with those of others authors that make the same assumption.

In Fig. 11, we show a different rendition of the similar fig. 2b of Cappellari et al. (2012). Here, we plot $(M/L)_{Salp}$ versus $(M/L)_{stars}$. We still exclude galaxies with very young stellar populations, selected as having stellar absorption line-strength index $H\beta > 2.3$ Å. We found that those galaxies have strong gradient in the stellar

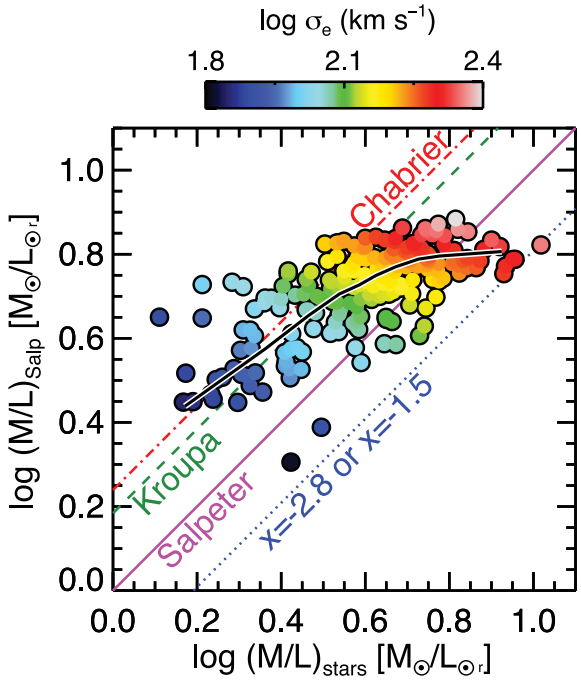

Figure 11. The systematic variation of the IMF. The $(M/L_r)_{stars}$ of the stellar component, determined via dynamical models, is compared to the $(M/L_r)_{Salp}$ determined from spectral fitting using stellar population models and assuming for reference a fixed Salpeter IMF. The colours of the symbols show the galaxies σ_e, which was LOESS smoothed in two dimension to emphasize the trends. The plot only includes the subsets of ATLAS^{3D} galaxies with $H\beta < 2.3$ Å, for which $(M/L)_{Salp}$ is sufficiently reliable. Diagonal lines illustrate the expected trends if the IMF was universal with either the Chabrier (red dash–dotted line), Kroupa (green dashed line) or Salpeter ($\zeta(m) \propto m^{-2.3}$, solid magenta line) forms. Also shown is the expected trend for two IMFs heavier than Salpeter (blue dotted line): a top-heavy one, dominated by stellar remnants ($\zeta(m) \propto m^{-1.5}$) and a bottom-heavy one, dominated by dwarfs ($\zeta(m) \propto m^{-2.8}$). The black solid curve is a LOESS-smoothed version of the data. A clear systematic trend is evident, with the IMF being closer to Kroupa/Chabrier at the lowest M/L, which also have the lowest σ_e, and closer to Salpeter or heavier at the largest M/L or largest σ_e. A different rendition of this plot was presented in fig. 2b of Cappellari et al. (2012).

population and this breaks our approximate assumption of a constant $(M/L)_{stars}$ within the region where we have kinematics, making both $(M/L)_{stars}$ and $(M/L)_{Salp}$ inaccurate and ill-defined. Different diagonal lines illustrate the expected trends if the IMF was universal or either the Chabrier, Kroupa or Salpeter ($\xi(m) \propto m^{-2.3}$) forms. Also shown is the expected trend for two IMFs heavier than Salpeter: a top-heavy one, dominated by stellar remnants ($\xi(m) \propto m^{-1.5}$), and a bottom-heavy one, dominated by dwarfs ($\xi(m) \propto m^{-2.8}$). This figure clearly illustrates the fact that the two indicators of M/L do not follow a one-to-one relation, but deviate systematically, with the IMF being consistent on average with Kroupa/Chabrier at the lowest $(M/L)_{stars}$ and with Salpeter or heavier at the largest $(M/L)_{stars}$, as already concluded in Cappellari et al. (2012). Another way to interpret this plot is by noting that galaxies with the largest $(M/L)_{Salp}$, which are characterized by the oldest populations, have a Salpeter or heavier IMF, while those with the lowest $(M/L)_{Salp}$, which have younger populations, have on average a Kroupa/Chabrier IMF. Detailed trends of the IMF with other population indicators will be presented in McDermid et al. (in preparation).

As in the Cappellari et al. (2012), we also show with colours the galaxies velocity dispersion. However, to emphasize the trend, here we apply the same two-dimensional LOESS smoothing approach (Cleveland & Devlin 1988) introduced in Section 3, instead of showing the individual σ_e values. One can still see the trend for the IMF to vary between Kroupa/Chabrier and Salpeter, albeit with large scatter, within the interval $\log_{10}(\sigma_e/\mathrm{km\ s^{-1}}) \approx 1.9$–$2.5$, with a smooth variation in between. This trend will be more precisely quantified in Section 4.3.

In Fig. 12, we show the variation of the IMF mismatch parameter $(M/L)_{stars}/(M/L)_{Salp}$ on the (M_{JAM}, σ_e) and (M_{JAM}, R_e^{maj}) projections of the MP. The trends in IMF are necessarily noisier than the ones in $(M/L)_{stars}$, as here the errors in both M/L combine. However, the structure in this figure closely resembles the one in the previous Figs 1, 3 and the top panel of Fig. 6. The systematic variation in the IMF follows on average the variations in the total $(M/L)_{JAM}$ and its corresponding stellar population indicators Hβ and galaxy colour, as well as the molecular gas fraction. Like the other quantities, also the IMF appears to roughly follow lines of constant σ_e on the MP, which we showed is tracing the bulge fraction at given galaxy size and mass. In both projections, there is indication for some extra substructure, with IMF variation at constant σ_e. Moreover, the proximity to the ZOE (thick red line) seems to be an even better indicator of IMF than σ_e (blue dashed lines). The (M, R_e^{maj}) projection also makes clear why one should expect spirals to have on average light IMF: spirals populate the empty zone above our galaxies (Fig. 9 here and fig. 4 in Paper I) and overlap with the distribution of ETGs with the Kroupa/Chabrier IMF. However, our plot suggests that, at fixed galaxy stellar (or M_{JAM}) mass and below $M_{JAM} \lesssim 10^{11}\,M_\odot$, the bulge mass (as traced by σ_e) is the main driver of the IMF variation, rather than morphological type, and one may expect IMF variations within the spiral population as well. Our finding explains why Dutton et al. (2012a) inferred a Salpeter or heavier IMF when selecting the smallest (or densest) galaxies at fixed mass, and assuming no DM. DM appears to provide a small contribution to the M/L for our entire sample and not just the smallest ones (Paper XV), but the densest galaxies are precisely the ones with the heaviest IMF. A recent claim has been made for a Salpeter IMF in the bulge of five massive spirals (Dutton et al. 2013), which would go in the suggested direction. However, the IMF is currently already difficult to infer when the M/L can be assumed to be spatially constant and the stellar population homogeneous. Relaxing these assumptions makes the results more uncertain unless very good population data from galaxy spectra and accurate non-parametric models for the photometry are employed.

4.3 IMF versus σ_e correlation

In the previous section, we illustrated the systematic IMF trends already presented in Cappellari et al. (2012) and we additionally presented the variation of the IMF on the projections of the MP. We pointed out that, like the dynamical M/L, its population indicators, colour and Hβ, the cold gas fraction and the galaxy concentration,

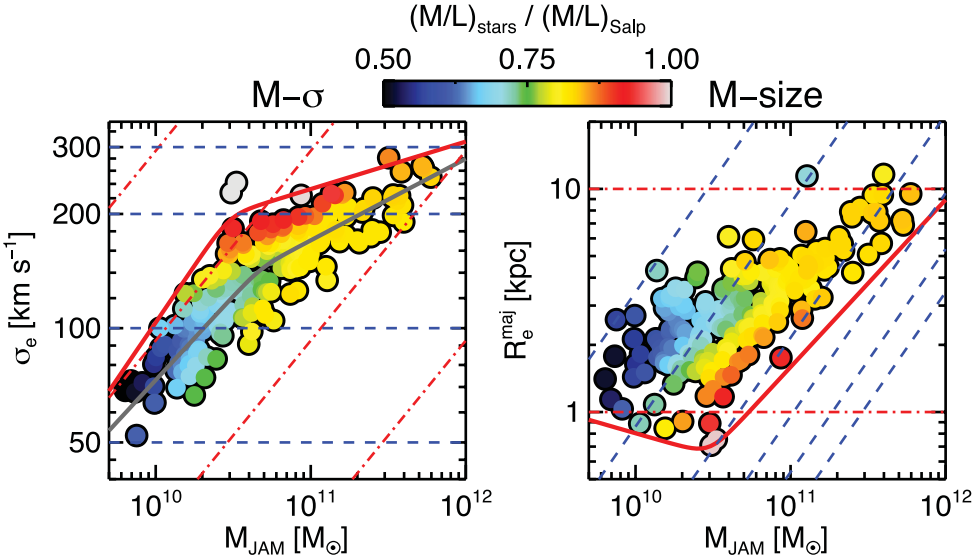

Figure 12. Variation of the IMF on the MP projections. Same as in Fig. 1 for the variation of the IMF mismatch parameter $(M/L)_{stars}/(M/L)_{Salp}$, which measure the ratio between the stellar M/L from dynamical models and the one from population models, with a fixed Salpeter IMF for reference. Like in Fig. 11 only galaxies with Hβ < 2.3 Å are included. The trend follows lines of roughly constant σ_e, or even better, follows lines parallel to the ZOE (thick red line) above its break. Like in other diagrams the trend looks different at large masses $M_{JAM} \gtrsim 10^{11}\,M_\odot$, suggesting these objects are different. The heaviest IMF (red colour) is not reached by the most massive galaxies, but by the fast rotators with the biggest bulges.

which traces to the bulge mass, also the IMF broadly follows lines of nearly constant σ_e on the (M_{JAM}, σ_e) MP projection and consequently $R_e^{maj} \propto M_{JAM}$ on the (M_{JAM}, R_e^{maj}) projection. Interestingly, a 'conspiracy' between the IMF variation and other galaxies properties is required for galaxy scaling relations to still have a small scatter (Renzini & Ciotti 1993).

In Fig. 13, we present a direct correlation between the logarithm of the IMF mismatch parameter $(M/L)_{stars}/(M/L)_{Salp}$ and the logarithm of σ_e, using the robust linear fitting routine LTS_LINEFIT presented[5] in Paper XV, which combines the Least Trimmed Squares robust technique of Rousseeuw & Driessen (2006) into a least-squares fitting algorithm which allows for intrinsic scatter. Like earlier, we exclude galaxies with very young stellar populations, selected s having stellar absorption line-strength index Hβ > 2.3 Å, leading to a sample of 223 out of 260 galaxies. In the fits, we quadratically co-added JAM modelling errors of 6 per cent (Paper XV) plus distance errors (Paper I) for $(M/L)_{stars}$ plus population models errors of 6 per cent for $(M/L)_{Salp}$ (Fig. 10) plus 10 per cent errors for our photometry (Paper XXI). We present fits for (i) the full sample, (ii) for the subsample of galaxies with surface brightness fluctuation (SBF) distances (mostly from Tonry et al. 2001 and Mei et al. 2007; see Paper I) and (iii) for galaxies with $M_{JAM} < 2 \times 10^{11}\,M_\odot$, to eliminate the galaxies above the characteristic mass where the IMF trend, as well as other galaxy properties, seems to change (see Figs 7, 8 and 12). All three relations have a comparable observed scatter $\Delta \approx 0.12$ dex (32 per cent) in $(M/L)_{stars}/(M/L)_{Salp}$ and imply a significant intrinsic scatter of about 21 per cent. When the same outliers are removed, we verified that indistinguishable values for the parameter, their errors and the inferred intrinsic scatter are obtained with the Bayesian approach of Kelly (2007), as implemented in his IDL routine LINMIX_ERR. Our three fits provide consistent values for the best-fitting slopes, within the errors, and nearly consistent normalizations. The fitted relation has the form

$$\log_{10}\frac{(M/L)_{stars}}{(M/L)_{Salp}} = a + b \times \log_{10}\frac{\sigma_e}{130\,km\,s^{-1}}, \qquad (8)$$

and our preferred values (bottom panel of Fig. 13) have best-fitting parameters and formal errors $a = -0.12 \pm 0.01$ and $b = 0.35 \pm 0.06$ (parameters and errors for the other fits are given inside the figures). The observed trend of IMF with σ appears to account for about half of the total trend in the (M/L)–σ_e relation $(M/L)_{JAM} \propto \sigma_e^{0.72}$ (see Paper XV), the remaining one being due to stellar population variations.

Our trend implies a transition of the mean IMF from Kroupa to Salpeter in the interval $\log_{10}(\sigma_e/km\,s^{-1}) \approx 1.9$–$2.5$ (or $\sigma_e \approx$ 90–290 km s^{-1}), with a smooth variation in between, consistently with what can be seen in Cappellari et al. (2012) and in Fig. 11. The fact that this trend is slightly weaker than the one implied by Fig. 11 seems to confirm the intrinsic differences in the IMF of individual galaxies. However, part of this difference could also be explained if the distance errors were underestimated. One way to address this issue would be to repeat our analysis for galaxies in a clusters at intermediate distance like the Coma cluster, for which relative distance errors can be neglected.

Our slope is a factor of ≈3.5 smaller than the 'tentative' trend reported in Treu et al. (2010) for the same quantities, and making the same assumption for the dark halo. A reason for this large difference must be due to the fact that their sample only included galaxies with

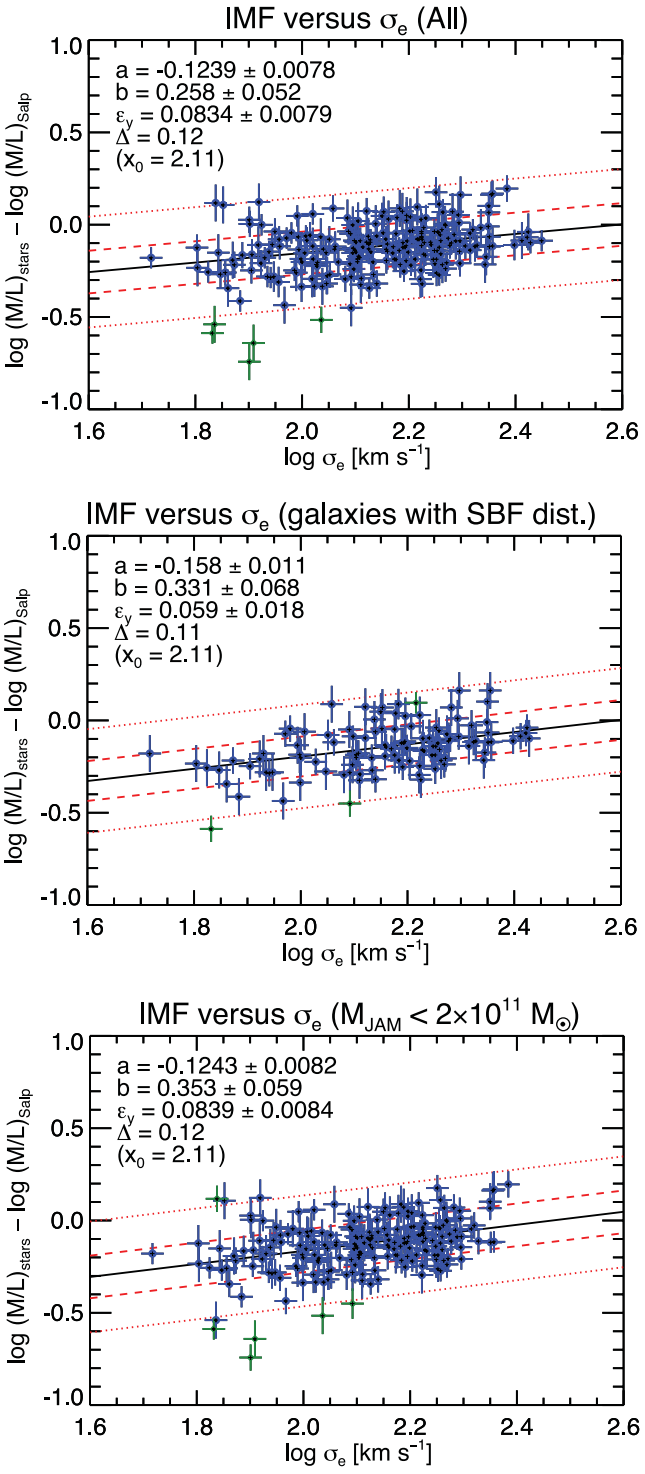

Figure 13. IMF versus σ_e correlations. The plots show as blue filled circles with error bars the logarithm of the IMF mismatch parameter $(M/L)_{stars}/(M/L)_{Salp}$ versus the effective velocity dispersion σ_e, for the subsets of ATLAS^{3D} galaxies with Hβ < 2.3 Å. The green symbols represents the outliers automatically removed from the fits. The dashed and dotted red lines indicate the 1σ and 2.6σ (99 per cent) observed scatter around the best-fitting relation (black solid line). The top panel includes all galaxies. The middle panel shows galaxies with accurate SBF distances. The bottom panel shows galaxies with $M_{JAM} < 2 \times 10^{11}\,M_\odot$.

[5] Available from http://purl.org/cappellari/idl.

$\sigma \gtrsim 200\,\mathrm{km\,s^{-1}}$ ($\log_{10}(\sigma/\mathrm{km\,s^{-1}}) \gtrsim 2.3$). Our sample is too small to reliably study trend in IMF for the galaxies above that σ_e, but their reported trend would exceed the slope of the (M/L)–σ relation (Paper XV), making it difficult to explain. Their steep inferred trend may then be due to their use of spherical and homologous models for all the galaxies, which must introduce systematic trends. Moreover, they used single stellar population M/L based on colours is expected to be less reliable than our determinations based on spectra (Gallazzi & Bell 2009). A reanalysis of the unique SLACS data set seems required to clarify this issue. Our trend with σ_e is also smaller than the one reported by Ferreras et al. (2013) from spectral analysis, who find a rapid change from a Kroupa to a Salpeter IMF in the narrow interval $\sigma \approx 150$–$200\,\mathrm{km\,s^{-1}}$. Our relation is not inconsistent with the values presented in Conroy & van Dokkum (2012b) also from spectral analysis, or with the result reported by Spiniello et al. (2012), with the IMF becoming steeper than Salpeter above $\sigma \gtrsim 200\,\mathrm{km\,s^{-1}}$. We are also broadly consistent with the IMF variation implied by the non-contracted halo spherical dynamical models of Tortora et al. (2013). Overall there is a qualitative agreement between different approaches and the still significant systematic differences in the various methods could account for the differences.

5 DISCUSSION

5.1 Previous relations as seen on the MP

We have shown in Paper XV that the galaxies FP (Djorgovski & Davis 1987; Dressler et al. 1987) can be accurately explained by virial equilibrium combined with a smooth variation of galaxy properties, mainly the total mass-to-light ratio M/L, with velocity dispersion, with galaxies lying on a tight MP ($M_\mathrm{JAM}, \sigma_\mathrm{e}, R_\mathrm{e}^\mathrm{maj}$), for a large volume-limited sample of ETGs (Paper I). Once this has been established, the interesting information on galaxy formation is then all contained in the distribution and the physical properties of galaxies on this plane, which we presented in this paper.

We find that on the MP: (i) galaxies sizes are delimited by a lower boundary, which has a minimum at a characteristic mass $M_\mathrm{JAM} \approx 3 \times 10^{10}\,\mathrm{M_\odot}$; (ii) a number of key galaxy properties: dynamical M/L, and its population indicators Hβ and colour, as well as the molecular gas fraction, which are mainly related to age, the normalization of the IMF and the prominence of the bulge, all tend to be constant along lines of constant σ_e, on the MP; (iii) another characteristic mass for galaxy properties is the value $M_\mathrm{JAM} \approx 2 \times 10^{11}\,\mathrm{M_\odot}$, which separates a region dominated by the round or weakly triaxial slow rotators at large masses from the one dominated by fast-rotators ETGs, flattened in their outer parts and with embedded exponential discs (Paper XVII), whose characteristics merge smoothly with the ones of spiral galaxies. A transition in the bulge fraction at this galaxy mass appears required in our models for the formation of fast and slow rotators (Khochfar et al. 2011, hereafter Paper VIII).

Although our ATLAS^{3D}sample is limited to a minimum mass of $M_\mathrm{JAM} \gtrsim 6 \times 10^9\,\mathrm{M_\odot}$, our picture naturally extends to lower masses. As shown in Fig. 9, our trends for fast-rotator ETGs continue with the dwarf spheroidal (Sph) sequence at lower masses (see also fig. 7 of Binggeli, Sandage & Tarenghi 1984; fig. 38 of Kormendy et al. 2009; fig. 12 of Chen et al. 2010; fig. 4 of Misgeld & Hilker 2011; fig. 20 of Kormendy & Bender 2012), while the spirals sequence continues with a sequence of low-mass late spirals or irregulars (Sc-Irr), as independently noted also by Kormendy & Bender (2012). Interestingly, the approximate stellar mass $M_\star \approx 2 \times 10^9\,\mathrm{M_\odot}$ where there is a break in the *M*–size relation of dwarf galaxies and where galaxies with bulge starts to appear (Fig. 9) corresponds to the threshold for quenching of field galaxies recently discovered by Geha et al. (2012). Below that mass only the cluster or group environment can strip spirals of their gas. Perhaps below that mass bulges cannot grow and star formation cannot be quenched by internal processes.

The parallelism between fast-rotator ETGs and spiral galaxies in scaling relations was one of the driver for our proposed revision (Paper VII) to the tuning-fork diagram by Hubble (1936), in the spirit of van den Bergh (1976) proposed parallelism between S0s and spirals. In Fig. 14, we summarize our results on morphology, kinematics, population and scaling relations in a single diagram, using the same galaxy symbols as fig. 2 of Paper VII, to provide a link between the two papers. This picture allows us to provide a new perspective and a clean empirical view of a number of classic scaling relation and known trends in galaxy properties.

5.1.1 *L*–σ trends

The classic Faber & Jackson (1976) relation $L \propto \sigma^4$ is well known to be a projection of the FP. We study it here using dynamical mass instead of light. Our study for the first time uses σ_e values integrated within R_e, which properly account for both velocity dispersion and stellar rotation, in combination with accurate dynamical masses which, unlike luminosity, can be properly related to the stellar kinematics. We find that the relation is not well described by an approximately linear trend, but it shows a break which is a reflection of the one in the ZOE (equation 4). The slope of the mean σ–M relation (equation 5) changes from $M_\mathrm{JAM} \propto \sigma_\mathrm{e}^{2.3}$ below $M_\mathrm{JAM} \approx 5 \times 10^{10}\,\mathrm{M_\odot}$ ($\sigma_\mathrm{e} \approx 140\,\mathrm{km\,s^{-1}}$) to $M_\mathrm{JAM} \propto \sigma_\mathrm{e}^{4.7}$ at larger masses. Thanks to our use of dynamical masses and σ_e, we find for the first time that the bend in the relation is quantitatively consistent with the one we observe in the *M*–size relation.

The slope we find at the high-mass range is consistent with the original Faber & Jackson (1976) relation, while the low-mass slope in our σ–M relation is consistent with claims of a change in the slope of the σ–L relation of elliptical galaxies at low luminosities, where the relation was reported to become $L \propto \sigma^2$ (Davies et al. 1983; Held et al. 1992; de Rijcke et al. 2005; Matković & Guzmán 2005; Lauer et al. 2007a; Forbes et al. 2008; Tortora et al. 2009). However, previous studies differ from ours because of M/L variations, they ignore stellar rotation, suffer from small number statistics and selection biases. This may be the reason why previous studies suggested a value $M_B \approx -20.5$ mag for the break in the σ–L relation (see section 3.3.3 of Graham 2013 for a review), which corresponds to the characteristic mass $M \approx 2 \times 10^{11}\,\mathrm{M_\odot}$, using the (M/L)–$\sigma$ relation (Cappellari et al. 2006) and considering a typical galaxy colour $B - I \approx 2.2$ mag. The previously reported mass is clearly inconsistent with our accurate value $M_\mathrm{JAM,\,b} \approx 5 \times 10^{10}\,\mathrm{M_\odot}$. Our new result shows that the break in the relation is associated with the characteristic mass $M_\mathrm{JAM} \approx 3 \times 10^{10}\,\mathrm{M_\odot}$ of the break in the ZOE and not with the other characteristic mass $M_\mathrm{JAM} \approx 2 \times 10^{11}\,\mathrm{M_\odot}$ above which round, slow-rotator, cored galaxies dominate.

Observations from the much larger SDSS sample have failed to find evidence for a clear break in the σ–L relation (Bernardi et al. 2003; Gallazzi et al. 2006; Hyde & Bernardi 2009a). For this reason, the relation is still often assumed to be a power law. The accuracy and homogeneity of our data, the size of our sample and especially the quantitative consistency between the σ–M and R_e–M relation provides an unambiguous confirmation for the break and an accurate determination of the transition mass.

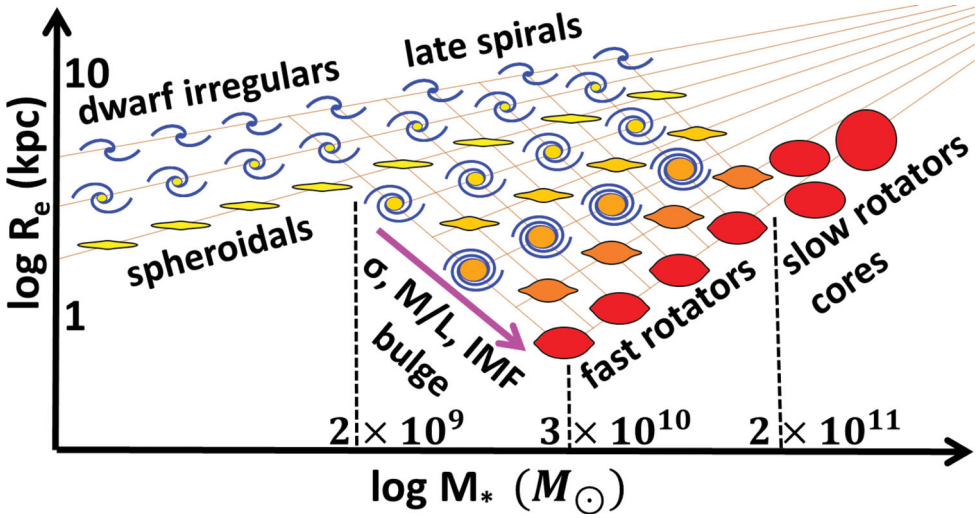

Figure 14. Schematic summary of the results presented in Sections 3 and 4. ETGs' properties, dynamical M/L (Fig. 1) or its population proxies, Hβ and galaxy colour, as well as the molecular gas fraction (Fig. 3), kinematical concentration (Fig. 6), which traces bulge mass, and IMF mass normalization (Fig. 12), all tend to vary along lines with roughly $R_e \propto M$ (or even better $R_e \propto M^{0.75}$), where σ_e is nearly constant. This sequence of ETGs' properties merges smoothly with the one of spiral galaxies (Fig. 9), with little overlap between late spirals (Sc-Irr) and ETGs, a significant overlap between early spirals (Sa-Sb) and fast-rotator ETGs with low M/L and no overlaps between spirals and fast rotators with high M/L. Three characteristic masses are emphasized in this diagram: (i) below $M_\star \approx 2\times10^9\,M_\odot$ there are no regular ETGs and the mass–size lower boundary is increasing (Fig. 9); (ii) $M_\star \approx 3\times10^{10}\,M_\odot$ is the mass at which ETGs reach their minimum size (or maximum stellar density), before a sudden change in slope $R_e \propto M^{0.75}$ at larger masses (see also fig. 4 in Paper I); (iii) Below $M_\star \approx 2\times10^{11}\,M_\odot$ ETGs are dominated by flat fast rotators (Figs 7 and 8), showing evidence for discs (Paper XVII), while slow rotators are rare. Above this mass there are no spirals and the population is dominated by quite round or weakly triaxial slow rotators (paper III) with flat (core/deficit) central surface brightness profiles (Paper XXIV). These smooth trends in scaling relations motivated our proposed parallelism between spirals and fast rotator ETGs. To emphasize this connection, we uses the same morphology symbols here as in our 'comb' diagram in fig. 2 of Paper VII.

5.1.2 $L-R_e$ *trends*

Another well-known projection of the FP is the Kormendy (1977) relation. When using mass instead of light, it becomes clear that it represents the analogue of the Faber & Jackson (1976), but this time in the (M_{JAM}, R_e^{maj}) projection of the MP. Also in this case, when samples are morphologically selected to consist of ellipticals, they tend to populate mostly the region of the diagram near the ZOE, defining a relatively narrow sequence (Graham & Worley 2008; Kormendy et al. 2009; Chen et al. 2010; Misgeld & Hilker 2011). Although the sequence is useful for a number of studies, it is important to realize that it is not a real sequence in galaxy space on the MP. It is due to the sample selection and it represents essentially one of the contour levels of a continuous trend of galaxy properties, spanning from spiral galaxies, to ETGs, and only terminating on the well-defined ZOE (Fig. 9 here and fig. 4 in Paper I).

Given that photometry is much easier to obtain than stellar kinematics, a change of slope in the luminosity–size relation has been known for long. It was pointed out by Binggeli et al. (1984, their fig. 7) when combining photometry measurements of dwarf spheroidals and ordinary ellipticals: the dwarf spheroidals sequence appears to sharply bend from the ellipticals sequence. Similar differences in the slope of the luminosity–size relation of dwarfs and ellipticals were presented by a number of authors (e.g. Kormendy 1985; Graham & Guzmán 2003; Kormendy et al. 2009; Misgeld & Hilker 2011). The change of slope has been interpreted in different ways. Kormendy (1985) and Kormendy et al. (2009) interpreted dwarf spheroidal as constituting a separate family, of gas-stripped dwarf spirals/irregulars, while Graham & Guzmán (2003) and Graham & Worley (2008) explain the change of slope or curvature in the relation as a natural consequence of the variation of the Sersic (1968) index with luminosity (e.g. Young & Currie 1994; Graham & Guzmán 2003) in a homogeneous class of elliptical galaxies with a range of masses (see Graham 2013 and Kormendy & Bender 2012 for two complementary reviews of this subject).

Our results cannot be compared to theirs in a statistical sense, as galaxies in their diagrams are, by design, not representative of the population in the nearby Universe, and certain classes of objects (e.g. M32) are over-represented. Our sample is volume limited and for this reason it gives a statistically representative view of the galaxy population above a certain mass. Still the fact that the sequence of dwarf spheroidals and low-mass spirals/irregulars lie on the continuation of our trends for fast-rotator ETGs and spiral galaxies, respectively (Fig. 9), below the $M_\star \lesssim 6\times10^9\,M_\odot$ mass limit of our survey suggests a continuity between dwarf spheroidals and the low-mass end of our disc-dominated fast-rotator ETGs' population, which in turn we showed are closely related to spiral galaxies. For this reason, our results reconciles the apparent contrast between the findings of an Sph–E dichotomy (Kormendy 1985; de Rijcke et al. 2005; Janz & Lisker 2008; Kormendy et al. 2009) and the ones of a continuity (Graham & Guzmán 2003; Gavazzi et al. 2005; Côté et al. 2006; Ferrarese et al. 2006; Boselli et al. 2008; Graham & Worley 2008; Janz & Lisker 2009; Forbes et al. 2011). Our finding in fact agrees with the proposed common origin of dwarf spheroidal and low-mass spiral galaxies and irregulars (Kormendy 1985; Dekel & Silk 1986), but also shows an empirical continuity between dwarf spheroidals and a subset of the ellipticals family. The missing link between Sph and E is constituted by disc-dominated fast-rotator ETGs (Cappellari et al. 2007; Emsellem et al. 2007). In fact, the continuity we find is not between 'true' ellipticals, namely the slow rotator and dwarf spheroidals, but between 'misclassified' ellipticals with discs and S0, namely the fast rotators and dwarf spheroidals. After this text was written and the parallelism between spiral galaxies and ETGs were presented (Paper VII) to interpret the

trends we observed in galaxy scaling relations (Paper I and Cappellari 2011a), an independent confirmation of this picture, including its extension to low-mass systems was also provided by Kormendy & Bender (2012).

5.1.3 *Population trends with σ or R_e*

The characteristic mass $M_{JAM} \approx 3 \times 10^{10}\,M_\odot$ is the same transition mass discovered by Kauffmann et al. (2003a) who state that 'low-redshift galaxies divide into two distinct families at a stellar mass of $3 \times 10^{10}\,M_\odot$. Lower mass galaxies have young stellar populations, low surface mass densities and the low concentrations typical of discs. Their SFH are more strongly correlated with surface mass density than with stellar mass.' A similar trend, involving colours and also better correlated with surface density (or with the velocity dispersion estimated from the photometry) than with mass, was found to extend to redshift up to $z \approx 3$, with red galaxies being systematically small, and blue galaxies being large at a given mass (Franx et al. 2008). This was recently confirmed, still using photometric data alone, by Bell et al. (2012). The correctness of all these statements can now be easily and accurately verified for the nearby ETG subset in Figs 1 and 3.

The novelty of our work, with respect to all previous studies, is that we have unprecedentedly accurate and unbiased dynamical masses, and stellar velocity dispersions σ_e integrated within a large aperture ($1R_e$), instead of σ values inferred from photometry. This allow us to conclusively state that neither dynamical mass nor stellar surface density are actually the best descriptor of galaxy properties, the main trend being along the σ_e direction (which includes rotation in the case of disc galaxies). Our clean ATLAS^{3D} result was already presented in Cappellari (2011a) and subsequently confirmed with SDSS data and using virial mass estimates by Wake, van Dokkum & Franx (2012). The trend we observed for the ETGs can be extended to spiral galaxies, which fill the region of larger sizes above the ETGs in the (M_{JAM}, R_e^{maj}) projection, smoothly overlapping with the ETGs for the largest spiral bulge fractions (fig. 4 of Paper I and Fig. 9). It has been known for long that in spirals luminosity-weighted ages are lower, star formation is larger and colours bluer on average than the ETGs, essentially by definition (e.g. Hubble 1936; van den Bergh 1976).

Similar trends between age and size (or surface brightness), with older objects being smaller at given age, were found to persist in ETGs. van der Wel et al. (2009a) state that 'at a given stellar velocity dispersion, SDSS data show that there is no relation between size and age'. The same age–size trend was pointed out by Shankar & Bernardi (2009), and in different terms by Graves, Faber & Schiavon (2009) who state that 'no stellar population property shows any dependence on R_e at fixed σ, suggesting that σ and not dynamical mass is the better predictor of past SFH'. These findings are another way of saying that age variations must follow lines of constant σ on the MP as we find here for M/L, Hβ, colour and molecular gas fraction, and confirm using age for our sample in McDermid et al. (in preparation), in agreement with Gallazzi et al. (2006, their fig. 15). The age–size trend was also confirmed in different samples of nearby galaxies by Valentinuzzi et al. (2010) and Napolitano, Romanowsky & Tortora (2010), and a similar trend, with star-forming galaxies being larger than passive ones was found in place from redshift $z \sim 2.5$ (Williams et al. 2010b; Wuyts et al. 2011; Newman et al. 2012). The only contrasting view is the one by Trujillo, Ferreras & de La Rosa (2011), who find a lack of age–size trend both at low and high redshift.

The same characteristics mass $M_\star \approx 3 \times 10^{10}\,M_\odot$ of Kauffmann et al. (2003a), which constitute the location of the break in our ZOE, was found by Hyde & Bernardi (2009a) in the mass–size relation of 5×10^4 SDSS galaxies. Their trend is significant but quite subtle. The reason for the curvature they find becomes clear from what we find: the average radius of the objects on the MP at constant mass bends upwards at low masses, due to the cusp in the ZOE, with the strength of the effect being dependent on the specific criterion adopted to select ETGs.

5.2 Implications for galaxy formation

Galaxy formation is the superposition of a number of complex events that happen in parallel. Here, we sketch a tentative picture of some of the phenomena that can play a role in explaining what we see. We refer the reader to Bois et al. (2011, hereafter Paper VI), Paper VIII and Naab et al. (in preparation) for a more in-depth discussion.

The smoothness and regularity of the trends we observe and the fact that they extend to spirals appears to indicate a close connection between the formation of the two classes of objects (Paper VIII). The same similarity between the fast-rotator ETGs and spirals in terms of their morphology and degree of rotation lead us to propose a revision (Paper VII) of the classic morphological classification (Hubble 1936) to emphasize the parallelism between the fast rotators and spirals, in the same way that van den Bergh (1976) proposed it for S0s and spirals. Only the most massive slow rotators appear to form an empirically separated class. The *kinematic* morphology–density relation (Paper VII), which applies to our kinematic classes the relation discovered by Dressler (1980), suggest that most spirals are being transformed into fast rotators due to environmental effects (Khochfar & Ostriker 2008), with a mechanism that is sufficiently 'gentle' to preserve the near axisymmetry of the disc (Paper II).

One process which is often mentioned in the context of cluster galaxy populations is stripping by the interstellar medium (Spitzer & Baade 1951; Abadi, Moore & Bower 1999), which may impact the global morphology of the galaxy by removing a significant fraction (or most) of its gas content but mostly preserving the stellar disc component. This may explain some of the most flattened galaxies in the fast-rotator class (e.g., NGC 4762), as emphasized in Paper VII. This would work by removing some of the mass of the galaxy keeping a relatively constant effective size (of the stellar component), and may contribute to the scatter in the mass–size plane for fast rotator as well as to their overlap with the more gas-rich spiral galaxies.

As to explain the intermediate- to high-σ end of the fast-rotator class, we would need a process which is able to increase the bulge size, while at the same time removing the gas or shutting off star formation (Paper VIII). The empirical signatures of this phenomenon are visible in our data as an 'apparent' decrease of the galaxy size, and increase of σ_e, which is actually due to the bulge concentrating more light at smaller radii, accompanied by an increase in M/L, which is tracing a decrease of star formation or an age increase. The process appears to generally preserve the intrinsic flatness of the stellar discs at large radii (top panel of Fig. 7). A similar scenario was recently proposed by Bell et al. (2012) to interpret the relationship between rest-frame optical colour, stellar mass, star formation activity and galaxy structure from $z \approx 2$ to the present day.

Intense gas-rich accretion events, mostly via cold streams (Kereš et al. 2005; Dekel et al. 2009a), or major gas-rich mergers (Paper VIII), will increase both the mass and σ_e. During the

accretion the gas may sink towards the centre (Mihos & Hernquist 1994) until it becomes self-gravitating and starts forming stars. It is during this phase of rapid gas accretion that the (M/L)–σ (Cappellari et al. 2006; van der Marel & van Dokkum 2007) and IMF–σ (Section 4.3) relations, the tilt of the FP (Dressler et al. 1987; Djorgovski & Davis 1987; Faber et al. 1987), the Mgb–σ (Burstein et al. 1988; Bender, Burstein & Faber 1993) or the Mgb–$V_{\rm esc}$ relation (Davies, Sadler & Peletier 1993; Scott et al. 2009; Paper XXI), will be imprinted in the ETGs' population (Robertson et al. 2006; Hopkins et al. 2009b) and then mostly preserved in the following evolution.

The early progenitors of today's fast-rotator ETGs would be high-redshift spirals, which are different from local ones. They are characterized by giant gas clumps (Elmegreen et al. 2007; Genzel et al. 2011), have high gas fractions (Daddi et al. 2010; Tacconi et al. 2010), possess large velocity dispersion and are dominated by turbulent motions (Förster Schreiber et al. 2006, 2009; Genzel et al. 2006, 2008; Law et al. 2012). In that situation, bulges may form naturally as the clumps collide and sink to the centre (Bournaud, Elmegreen & Elmegreen 2007; Dekel, Sari & Ceverino 2009b), unless they are efficiently destroyed by stellar feedback (Genel et al. 2012; Hopkins et al. 2012). Secular effects (Kormendy & Kennicutt 2004) will also contribute to the bulge growth and $\sigma_{\rm e}$ increase, while keeping the mass unchanged, as will contribute the destabilizing effect of minor mergers.

During the bulge growth some process must be able to turn off star formation, without destroying the fast-rotating discs that still dominate the local ETGs' population (Paper II; Paper III) and that dominates the ETGs' population already from $z \sim 2$ (van der Wel et al. 2011; see also van Dokkum 2011). The reduced efficiency of star formation by morphological quenching (Martig et al. 2009; Ceverino, Dekel & Bournaud 2010; Martig et al. 2013, hereafter Paper XXII) may be one of the processes explaining why on average bigger bulges correspond to older ages and larger M/L. However, we showed in Fig. 3 that the cold gas fraction is decreasing with the bulge fraction, which shows that less fuel is available for galaxies with more massive bulges. Bulge/spheroid growth seems also associated with AGN feedback, which would provide another bulge-related quenching mechanism (Silk & Rees 1998; Granato et al. 2004; Bower et al. 2006; Croton et al. 2006; Hopkins et al. 2006). During the sequence of bulge/spheroid-growth followed by quenching, the original gas-rich spiral will move from the left of the observed ($M_{\rm JAM}$, $R_{\rm e}^{\rm maj}$) plane towards the right, or possibly the bottom right due to the increased concentration, while intersecting the constant σ lines (blue arrow in Fig. 15 and top row of Fig. 16). At the end of the events, the galaxy will be a fast-rotator ETG, generally more massive and with a bigger bulge (smaller $R_{\rm e}$, larger $\sigma_{\rm e}$ and concentration) than the precursor clumpy spiral.

At any stage during the bulge-growth phase, the galaxy may accrete purely stellar satellites (Khochfar & Silk 2006). In the case of these dry mergers, the situation is quite different and one can predict the final configuration using energy conservation (Hernquist et al. 1993; Cole et al. 2000; Boylan-Kolchin et al. 2006; Ciotti, Lanzoni & Volonteri 2007). The predictions show that sizes will increase as the mass grows. For major mergers (equal mass) and typical orbital configurations, one can show that the mass and radius double, while σ remains constant in agreement with simulations (Nipoti et al. 2009; see Hilz et al. 2012; Hilz, Naab & Ostriker 2013 for more accurate numerical simulations and detailed physical explanations of this process). While in the limit in which the same mass doubling happens via small satellites as mostly expected from the shape of the Schechter (1976) mass function, the radius will increase by a factor of 4 and the dispersion will be twice smaller (Bezanson et al. 2009; Hopkins et al. 2009a; Naab, Johansson & Ostriker 2009; Hilz et al. 2012). As a result, the galaxy will move along lines that are parallel to the constant σ lines, or steeper. During these dry mergers, given that there is little gas involved, the stellar population, colour and M/L will remain unchanged (red arrow in Fig. 15 and bottom row of Fig. 16).

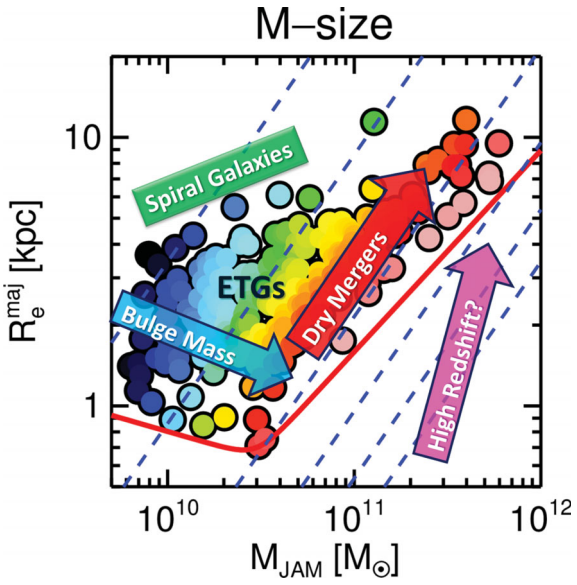

Figure 15. Evolution scenario for ETGs. The symbols are the same as in Fig. 1, while the large arrows indicate the proposed interpretation of the observed distribution as due to a combination of two processes – (a) in situ star formation: bulge or spheroid growth, which seems to be associated with the quenching of star formation, which moves galaxies towards the right of the bottom, due to the increased concentration (decreasing $R_{\rm e}$ and increasing $\sigma_{\rm e}$), and (b) external accretion: dry mostly minor merging, increasing $R_{\rm e}$ by moving galaxies along lines of roughly constant $\sigma_{\rm e}$ (or steeper), while leaving the population unchanged. A schematic illustration of these two processes is shown in Fig. 16.

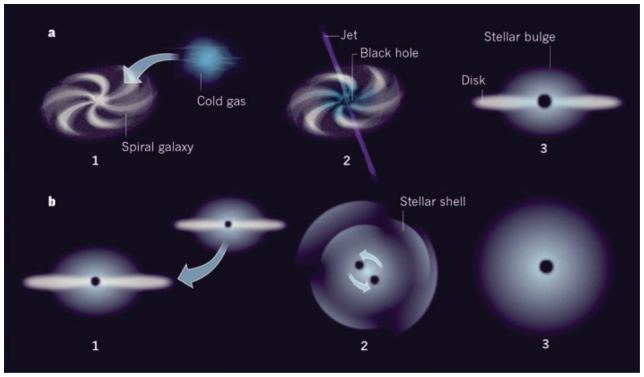

Figure 16. Schematic representation of the two main processes responsible for the formation of the observed distribution of galaxies on the MP. (a) In situ star formation: bulge growth via cold accretion, secular evolution, or minor gas-rich mergers, followed by quenching by AGN or other mechanisms, leaving the galaxy more massive, more compact, and consequently with a larger $\sigma_{\rm e}$, and gas poor (blue arrow in Fig. 15); (b) external accretion: major or minor dry mergers, increasing galaxy mass and sizes at nearly constant $\sigma_{\rm e}$, or with a possible decrease, leaving the population mostly unchanged (red arrow in Fig. 15). (Taken from Cappellari 2011b.)

When the galaxy grows more massive than the characteristic mass $M_\star \gtrsim 2 \times 10^{11}\,\mathrm{M}_\odot$, a transition seems to happen in their formation, evolution, possibly associated with the shock heating of the infalling gas, due to the halo mass (Dekel & Birnboim 2006). Above this mass galaxies are in fact embedded in massive and hot X-ray haloes (Kormendy et al. 2009; Paper XIX) which prevents any further cold gas accretion on to the galaxy.

The gas-rich mergers/accretion scenario is generally consistent with the observed correlation between supermassive black holes (BH) and galaxy velocity dispersion or bulge mass (Di Matteo, Springel & Hernquist 2005). It is generally believed that the correlations indicate a joint evolution of galaxies and BHs, with BH growth happening at the same time as the bulge growth, and providing a self-regulation via feedback (Silk & Rees 1998; but see Peng 2007 and Jahnke & Macciò 2011 for a non-causal origin of the correlations). We demonstrate that indeed the σ variation directly traces the bulge growth (Kormendy & Gebhardt 2001). In fact, σ traces the central galaxy concentration and the bulge size as estimated on optical morphology, while the outer galaxy discs remain flat. This implies that, if the BH indeed accretes from the same gas that grows the bulge, BH mass should correlate better with σ than with total mass as observed (Ferrarese & Merritt 2000; Gebhardt et al. 2000).

However, when ETGs' experience dry mergers, their BH grows in proportion to the mass, but galaxies move along lines of nearly constant σ. For this reason, an expectation from this picture is that BHs at the high-mass end should start to appear too massive with respect to the predictions of the $M_{\rm BH}$–σ relation (see also Nipoti et al. 2003; Boylan-Kolchin et al. 2006; Ciotti 2009). The high-mass BH end is still not sufficiently populated to reliably test this prediction, but indirect evidence seems to support this possibility (Lauer et al. 2007a). More evidence comes from the recent detection of two giant black holes at the centre of two bright cluster galaxies, which are clearly more massive than the $M_{\rm BH}$–σ prediction (McConnell et al. 2011) or the related observation that fainter ETGs follow a steeper $M_{\rm BH} - L$ relation than brighter ones (Graham 2012). The transition seems to happen near the mass of the break in our $\sigma - M$ relation as one would have expected (Scott et al. 2013b).

In summary, we propose that the distribution of galaxy properties on the MP, where M/L, age and cold gas fraction follow lines of constant σ, could be explained by the combination of two processes, which can happen multiple times during the evolution of a single galaxy. (i) They accrete gas, which grows the bulge and BH, shrinks their $R_{\rm e}$ and increases $\sigma_{\rm e}$ and concentration, while some process which seems to be associated with the bulge growth (e.g. AGN feedback), quenches star formation. (ii) They experience mostly minor dry mergers that move them along lines of roughly constant σ (or steeper).

An open question in the scenario in which ETGs evolve relatively quietly from spirals comes from the comparison of our findings with the empirical scaling relations one observes at larger redshift. In fact, at $z \gtrsim 1.5$ galaxies are found to be smaller than local ones with the same mass (Daddi et al. 2005; Trujillo et al. 2006, 2007; Cimatti et al. 2008; van Dokkum et al. 2008). They populate the region below the ZOE in the $(M, R_{\rm e})$ plane of local galaxies, although their σ tend to be consistent with our local (M, σ) observations (Cappellari 2013). This may indicate that the compact high-redshift ETGs follow a different and more violent evolutionary path than the more quiet majority of local ETGs, as suggested by other high-redshift observations (Barro et al. 2013). A way to reconcile this very mild (or lack of) σ evolution is by assuming that the compact primordial ETGs grow mostly by accretion of small satellites in their outer haloes, while preserving the central structure (Naab et al. 2009; Hopkins et al. 2010; Oser et al. 2010, 2012). This seems consistent with the shape of the photometric profiles of the early ETGs (Bezanson et al. 2009; Hopkins et al. 2009a; van Dokkum et al. 2010; Hilz et al. 2013). A caveat is that significant biases may still exist in the high-redshift photometry (Mancini et al. 2010), considering that systematic differences of up to a factor of 2 exist even on well-observed ETGs in the nearby Universe (Kormendy et al. 2009; Chen et al. 2010; Paper I). Moreover, comparisons of photometric profiles tend to be made against bona fide ellipticals, while the remnant of the high-redshift ETGs are likely disc-like fast-rotators ETG, which have systematically different profiles. Finally, the comparisons should ideally be done in mass density, instead of surface density, but kinematic information is available for only a handful of galaxies. This implies that there is perhaps still some room for the compact high-z ETGs to become more consistent with local ones, than currently assumed.

6 SUMMARY

In the companion Paper XV, we describe in detail the axisymmetric dynamical models for all the ATLAS^{3D} ETGs that were introduced in Cappellari et al. (2012). We found that galaxies lie on a thin MP in the three-dimensional parameter space defined by $(M_{\rm JAM}, \sigma_{\rm e}, R_{\rm e}^{\rm maj})$.

Here, we studied the inclined projection of the MP and find that (i) the galaxies define a clear ZOE, roughly described by two power laws, joined by a break at a first characteristic mass $M_{\rm JAM} \equiv L \times (\mathrm{M/L})_e \approx 3 \times 10^{10}\,\mathrm{M}_\odot$, which corresponds to the regime where a number of global galaxy properties were reported to change; (ii) we find a second characteristic mass $M_{\rm JAM} \approx 2 \times 10^{11}\,\mathrm{M}_\odot$, which separates a region with only nearly round slow-rotator ETGs at large masses from one dominated by fast-rotator ETGs with discs and spiral galaxies at lower masses; (iii) the distribution of $(\mathrm{M/L})_e$, as well as population indicators of $(\mathrm{M/L})_{\rm pop}$ like Hβ and colour, and the molecular gas fraction, all tend to be constant along lines of constant $\sigma_{\rm e}$ on the $(M_{\rm JAM}, \sigma_{\rm e})$ plane, or correspondingly $R_{\rm e}^{\rm maj} \propto M_{\rm JAM}$ (or even better parallel to the ZOE $R_{\rm e}^{\rm maj} \propto M_{\rm JAM}^{0.75}$) on the $(M_{\rm JAM}, R_{\rm e}^{\rm maj})$ plane; (iv) properties of ETGs merge smoothly and form parallel sequences to those of spiral galaxies; (v) below our survey mass limit, the distribution of fast-rotator ETGs continues with that of dwarf spheroidal (Sph), while the sequence of late spirals continues with the dwarf irregulars (Im).

We show that, at fixed mass, $\sigma_{\rm e}$ in ETGs traces the galaxy bulge fraction, which appears the main driver for the changes in galaxy properties that we observe. These findings explains why $\sigma_{\rm e}$ (not L, $M_\star$, $R_{\rm e}$ or $\Sigma_{\rm e}$) has often been the most successful single descriptor of galaxy properties. We discuss a number of previously found galaxy correlation and we find that they are all consistent with what we find. In fact, most observed relations turn out to be just special projections of the cleaner and more general view provided by the MP.

The stellar IMF was previously shown to vary systematically with $(\mathrm{M/L})_{\rm stars}$ (Cappellari et al. 2012) and as expected it also follows the other population indicators. It also tend to vary along lines of nearly constant $\sigma_{\rm e}$ on the MP. This is a necessary expectation if one wants to preserve the tightness of the FP or the (M/L)–$\sigma_{\rm e}$ relation. The trend of IMF with σ appears to account for about half of the total trend in the (M/L)–$\sigma_{\rm e}$ relation (see Paper XV), the remaining one being due to stellar population variations.

The distribution of galaxy properties on the MP can be qualitatively interpreted as due to a combination of two main processes:

(i) bulge growth, changing the galaxy population and decreasing R_e, while increasing σ_e, and (ii) dry merging, increasing mass and R_e by moving galaxies along lines of approximately constant σ_e, while leaving the population unchanged. It is unclear where the reported dense high-redshift ETGs fit in this picture. They may simply follow a different route, which forms the most massive galaxies and is not affecting the fast-rotator population, which dominates ETGs in the nearby Universe. Or there may be some remaining biases in the photometric observations, producing an underestimation of the radius. Stellar kinematics of high-redshift ETGs is critically needed to address this question.

ACKNOWLEDGEMENTS

MC acknowledges support from a Royal Society University Research Fellowship. This work was supported by the rolling grants 'Astrophysics at Oxford' PP/E001114/1 and ST/H002456/1 and visitors grants PPA/V/S/2002/00553, PP/E001564/1 and ST/H504862/1 from the UK Research Councils. RLD acknowledges travel and computer grants from Christ Church, Oxford and support from the Royal Society in the form of a Wolfson Merit Award 502011.K502/jd. RLD also acknowledges the support of the ESO Visitor Programme which funded a 3 month stay in 2010. SK acknowledges support from the Royal Society Joint Projects Grant JP0869822. RMcD is supported by the Gemini Observatory, which is operated by the Association of Universities for Research in Astronomy, Inc., on behalf of the international Gemini partnership of Argentina, Australia, Brazil, Canada, Chile, the United Kingdom and the United States of America. TN and MBois acknowledge support from the DFG Cluster of Excellence 'Origin and Structure of the Universe'. MS acknowledges support from a STFC Advanced Fellowship ST/F009186/1. PS is a NWO/Veni fellow. (TAD) The research leading to these results has received funding from the European Community's Seventh Framework Programme (/FP7/2007-2013/) under grant agreement No 229517. MBois has received, during this research, funding from the European Research Council under the Advanced Grant Program Num 267399-Momentum. The authors acknowledge financial support from ESO.

REFERENCES

Abadi M. G., Moore B., Bower R. G., 1999, MNRAS, 308, 947
Aihara H. et al., 2011, ApJS, 193, 29
Auger M. W., Treu T., Bolton A. S., Gavazzi R., Koopmans L. V. E., Marshall P. J., Bundy K., Moustakas L. A., 2009, ApJ, 705, 1099
Auger M. W., Treu T., Gavazzi R., Bolton A. S., Koopmans L. V. E., Marshall P. J., 2010a, ApJ, 721, L163
Auger M. W., Treu T., Bolton A. S., Gavazzi R., Koopmans L. V. E., Marshall P. J., Moustakas L. A., Burles S., 2010b, ApJ, 724, 511
Bacon R. et al., 2001, MNRAS, 326, 23
Baldry I. K., Glazebrook K., Brinkmann J., Ivezić Ž., Lupton R. H., Nichol R. C., Szalay A. S., 2004, ApJ, 600, 681
Barnabè M., Czoske O., Koopmans L. V. E., Treu T., Bolton A. S., 2011, MNRAS, 415, 2215
Barnabè M. et al., 2012, MNRAS, 423, 1073
Barro G. et al., 2013, ApJ, 765, 104
Bastian N., Covey K. R., Meyer M. R., 2010, ARA&A, 48, 339
Bell E. F., de Jong R. S., 2001, ApJ, 550, 212
Bell E. F. et al., 2012, ApJ, 753, 167
Bender R., Burstein D., Faber S. M., 1992, ApJ, 399, 462
Bender R., Burstein D., Faber S. M., 1993, ApJ, 411, 153
Bernardi M. et al., 2003, AJ, 125, 1866
Bernardi M., Roche N., Shankar F., Sheth R. K., 2011, MNRAS, 412, L6
Bershady M. A., Verheijen M. A. W., Swaters R. A., Andersen D. R., Westfall K. B., Martinsson T., 2010, ApJ, 716, 198
Bershady M. A., Martinsson T. P. K., Verheijen M. A. W., Westfall K. B., Andersen D. R., Swaters R. A., 2011, ApJ, 739, L47
Bezanson R., van Dokkum P. G., Tal T., Marchesini D., Kriek M., Franx M., Coppi P., 2009, ApJ, 697, 1290
Binggeli B., Sandage A., Tarenghi M., 1984, AJ, 89, 64
Binney J., Tremaine S., 2008, Galactic Dynamics, 2nd edn. Princeton Univ. Press, Princeton, NJ
Blanton M. R. et al., 2003, ApJ, 592, 819
Bois M. et al., 2011, MNRAS, 416, 1654 (Paper VI)
Bolton A. S., Burles S., Koopmans L. V. E., Treu T., Moustakas L. A., 2006, ApJ, 638, 703
Bolton A. S., Burles S., Koopmans L. V. E., Treu T., Gavazzi R., Moustakas L. A., Wayth R., Schlegel D. J., 2008a, ApJ, 682, 964
Bolton A. S., Treu T., Koopmans L. V. E., Gavazzi R., Moustakas L. A., Burles S., Schlegel D. J., Wayth R., 2008b, ApJ, 684, 248
Boselli A., Boissier S., Cortese L., Gavazzi G., 2008, ApJ, 674, 742
Bournaud F., Elmegreen B. G., Elmegreen D. M., 2007, ApJ, 670, 237
Bower R. G., Benson A. J., Malbon R., Helly J. C., Frenk C. S., Baugh C. M., Cole S., Lacey C. G., 2006, MNRAS, 370, 645
Boylan-Kolchin M., Ma C.-P., Quataert E., 2006, MNRAS, 369, 1081
Brewer B. J. et al., 2012, MNRAS, 422, 3574
Burstein D., Davies R. L., Dressler A., Faber S. M., Lynden-Bell D., 1988, in Renzini R. G. K. A., ed., Astrophysics and Space Science Library, Vol. 141, Towards Understanding Galaxies at Large Redshift. Kluwer Academic Publishers, Dordrecht, p. 17
Burstein D., Bender R., Faber S., Nolthenius R., 1997, AJ, 114, 1365
Caon N., Capaccioli M., D'Onofrio M., 1993, MNRAS, 265, 1013
Cappellari M., 2002, MNRAS, 333, 400
Cappellari M., 2008, MNRAS, 390, 71
Cappellari M., 2011a, in Hickox R., ed., Proc. Conf. on Galaxy Formation. Durham University, Durham, UK, available at http://astro.dur.ac.uk/Gal2011/talks.php
Cappellari M., 2011b, Nat, 480, 187
Cappellari M., 2013, in Thomas D., Pasquali A., Ferreras I., eds, Proc. IAU Symp. Vol. 295, The Intriguing Life of Massive Galaxies. Cambridge Univ. Press, Cambridge, in press (arXiv:1210.7742)
Cappellari M., Emsellem E., 2004, PASP, 116, 138
Cappellari M. et al., 2006, MNRAS, 366, 1126
Cappellari M. et al., 2007, MNRAS, 379, 418
Cappellari M. et al., 2011a, MNRAS, 413, 813 (Paper I)
Cappellari M. et al., 2011b, MNRAS, 416, 1680 (Paper VII)
Cappellari M. et al., 2012, Nat, 484, 485
Cappellari M. et al., 2013, MNRAS, 432, 1709 (Paper XV)
Carlberg R. G., 1986, ApJ, 310, 593
Cenarro A. J., Gorgas J., Vazdekis A., Cardiel N., Peletier R. F., 2003, MNRAS, 339, L12
Ceverino D., Dekel A., Bournaud F., 2010, MNRAS, 404, 2151
Chabrier G., 2003, PASP, 115, 763
Chen C., Côté P., West A. A., Peng E. W., Ferrarese L., 2010, ApJS, 191, 1
Chiosi C., Bressan A., Portinari L., Tantalo R., 1998, A&A, 339, 355
Cimatti A. et al., 2008, A&A, 482, 21
Ciotti L., 1991, A&A, 249, 99
Ciotti L., 2009, Nuovo Cimento Riv. Ser., 32, 1
Ciotti L., Lanzoni B., Volonteri M., 2007, ApJ, 658, 65
Cleveland W., 1979, J. Am. Stat. Assoc., 74, 829
Cleveland W., Devlin S., 1988, J. Am. Stat. Assoc., 83, 596
Cole S., Lacey C. G., Baugh C. M., Frenk C. S., 2000, MNRAS, 319, 168
Conroy C., van Dokkum P., 2012a, ApJ, 747, 69
Conroy C., van Dokkum P. G., 2012b, ApJ, 760, 71
Conroy C., Gunn J. E., White M., 2009, ApJ, 699, 486
Côté P. et al., 2006, ApJS, 165, 57
Croton D. J. et al., 2006, MNRAS, 365, 11
Daddi E. et al., 2005, ApJ, 626, 680
Daddi E. et al., 2010, ApJ, 713, 686
Davé R., 2008, MNRAS, 385, 147

Davies R. L., Efstathiou G., Fall S. M., Illingworth G., Schechter P. L., 1983, ApJ, 266, 41
Davies R. L., Sadler E. M., Peletier R. F., 1993, MNRAS, 262, 650
de Rijcke S., Michielsen D., Dejonghe H., Zeilinger W. W., Hau G. K. T., 2005, A&A, 438, 491
de Vaucouleurs G., 1959, Handbuch Phys., 53, 311
de Zeeuw P. T. et al., 2002, MNRAS, 329, 513
Deason A. J., Belokurov V., Evans N. W., McCarthy I. G., 2012, ApJ, 748, 2
Dekel A., Birnboim Y., 2006, MNRAS, 368, 2
Dekel A., Silk J., 1986, ApJ, 303, 39
Dekel A. et al., 2009a, Nat, 457, 451
Dekel A., Sari R., Ceverino D., 2009b, ApJ, 703, 785
Di Matteo T., Springel V., Hernquist L., 2005, Nat, 433, 604
Djorgovski S., Davis M., 1987, ApJ, 313, 59
D'Onofrio M. et al., 2008, ApJ, 685, 875
Dressler A., 1980, ApJ, 236, 351
Dressler A., Lynden-Bell D., Burstein D., Davies R. L., Faber S. M., Terlevich R., Wegner G., 1987, ApJ, 313, 42
Driver S. P. et al., 2011, MNRAS, 413, 971
Dutton A. A. et al., 2011a, MNRAS, 416, 322
Dutton A. A. et al., 2011b, MNRAS, 417, 1621
Dutton A. A., Mendel J. T., Simard L., 2012a, MNRAS, 422, L33
Dutton A. A., Maccio' A. V., Mendel J. T., Simard L., 2012b, MNRAS, in press (arXiv:1204.2825)
Dutton A. A. et al., 2013, MNRAS, 428, 3183
Elmegreen D. M., Elmegreen B. G., Ravindranath S., Coe D. A., 2007, ApJ, 658, 763
Emsellem E., Monnet G., Bacon R., 1994, A&A, 285, 723
Emsellem E. et al., 2004, MNRAS, 352, 721
Emsellem E. et al., 2007, MNRAS, 379, 401
Faber S. M., Jackson R. E., 1976, ApJ, 204, 668
Faber S. M., Dressler A., Davies R. L., Burstein D., Lynden-Bell D., 1987, in Faber S. M., ed., Nearly Normal Galaxies: From the Planck Time to the Present. Springer-Verlag, New York, p. 175
Faber S. M. et al., 1997, AJ, 114, 1771
Falcón-Barroso J., Sánchez-Blázquez P., Vazdekis A., Ricciardelli E., Cardiel N., Cenarro A. J., Gorgas J., Peletier R. F., 2011, A&A, 532, A95
Ferrarese L., 2012, in Rejkuba M., ed., Proc. Conf. on Science from the Next Generation Imaging and Spectroscopic Surveys. ESO, Garching, Germany, available at http://www.eso.org/sci/meetings/2012/surveys2012/program.html
Ferrarese L., Merritt D., 2000, ApJ, 539, L9
Ferrarese L. et al., 2006, ApJS, 164, 334
Ferrarese L. et al., 2012, ApJS, 200, 4
Ferreras I., Saha P., Burles S., 2008, MNRAS, 383, 857
Ferreras I., Saha P., Leier D., Courbin F., Falco E. E., 2010, MNRAS, 409, L30
Ferreras I., La Barbera F., de la Rosa I. G., Vazdekis A., de Carvalho R. R., Falcón-Barroso J., Ricciardelli E., 2013, MNRAS, 429, L15
Forbes D. A., Lasky P., Graham A. W., Spitler L., 2008, MNRAS, 389, 1924
Forbes D. A., Spitler L. R., Graham A. W., Foster C., Hau G. K. T., Benson A., 2011, MNRAS, 413, 2665
Förster Schreiber N. M. et al., 2006, ApJ, 645, 1062
Förster Schreiber N. M. et al., 2009, ApJ, 706, 1364
Franx M., van Dokkum P. G., Schreiber N. M. F., Wuyts S., Labbé I., Toft S., 2008, ApJ, 688, 770
Freeman K. C., 1970, ApJ, 160, 811
Gallazzi A., Bell E. F., 2009, ApJS, 185, 253
Gallazzi A., Charlot S., Brinchmann J., White S. D. M., 2006, MNRAS, 370, 1106
Gargiulo A. et al., 2009, MNRAS, 397, 75
Gavazzi G., Donati A., Cucciati O., Sabatini S., Boselli A., Davies J., Zibetti S., 2005, A&A, 430, 411
Gavazzi R., Treu T., Rhodes J. D., Koopmans L. V. E., Bolton A. S., Burles S., Massey R. J., Moustakas L. A., 2007, ApJ, 667, 176
Gebhardt K. et al., 2000, ApJ, 539, L13
Geha M., Blanton M. R., Yan R., Tinker J. L., 2012, ApJ, 757, 85
Gelman A., Carlin J., Stern H., Rubin D., 2004, Bayesian Data Analysis. CRC Press, Boca Raton
Genel S. et al., 2012, ApJ, 745, 11
Genzel R. et al., 2006, Nat, 442, 786
Genzel R. et al., 2008, ApJ, 687, 59
Genzel R. et al., 2011, ApJ, 733, 101
Gerhard O. E., Binney J. J., 1996, MNRAS, 279, 993
Gerhard O., Kronawitter A., Saglia R. P., Bender R., 2001, AJ, 121, 1936
Gnedin O. Y., Kravtsov A. V., Klypin A. A., Nagai D., 2004, ApJ, 616, 16
Gnedin O. Y., Ceverino D., Gnedin N. Y., Klypin A. A., Kravtsov A. V., Levine R., Nagai D., Yepes G., 2011, ApJ, preprint (arXiv:1108.5736)
Governato F. et al., 2010, Nat, 463, 203
Graham A. W., 2012, ApJ, 746, 113
Graham A. W., 2013, in Oswalt T. D., Keel W. C., eds, Planets, Stars and Stellar Systems, Vol. 6. Springer, Berlin, p. 91
Graham A. W., Guzmán R., 2003, AJ, 125, 2936
Graham A. W., Worley C. C., 2008, MNRAS, 388, 1708
Granato G. L., De Zotti G., Silva L., Bressan A., Danese L., 2004, ApJ, 600, 580
Graves G. J., Faber S. M., 2010, ApJ, 717, 803
Graves G. J., Faber S. M., Schiavon R. P., 2009, ApJ, 698, 1590
Grillo C., Gobat R., 2010, MNRAS, 402, L67
Grillo C., Gobat R., Lombardi M., Rosati P., 2009, A&A, 501, 461
Gunawardhana M. L. P. et al., 2011, MNRAS, 415, 1647
Heavens A., Panter B., Jimenez R., Dunlop J., 2004, Nat, 428, 625
Held E. V., de Zeeuw T., Mould J., Picard A., 1992, AJ, 103, 851
Hernquist L., 1990, ApJ, 356, 359
Hernquist L., Spergel D. N., Heyl J. S., 1993, ApJ, 416, 415
Hilz M., Naab T., Ostriker J. P., Thomas J., Burkert A., Jesseit R., 2012, MNRAS, 425, 3119
Hilz M., Naab T., Ostriker J. P., 2013, MNRAS, 429, 2924
Hopkins P. F., Hernquist L., Cox T. J., Di Matteo T., Robertson B., Springel V., 2006, ApJS, 163, 1
Hopkins P. F., Bundy K., Murray N., Quataert E., Lauer T. R., Ma C.-P., 2009a, MNRAS, 398, 898
Hopkins P. F., Hernquist L., Cox T. J., Keres D., Wuyts S., 2009b, ApJ, 691, 1424
Hopkins P. F., Bundy K., Hernquist L., Wuyts S., Cox T. J., 2010, MNRAS, 401, 1099
Hopkins P. F., Kereš D., Murray N., Quataert E., Hernquist L., 2012, MNRAS, 427, 968
Hoversten E. A., Glazebrook K., 2008, ApJ, 675, 163
Hubble E. P., 1936, Realm of the Nebulae. Yale Univ. Press, New Haven
Huchra J., Gorenstein M., Kent S., Shapiro I., Smith G., Horine E., Perley R., 1985, AJ, 90, 691
Huchra J. P. et al., 2012, ApJS, 199, 26
Hyde J. B., Bernardi M., 2009a, MNRAS, 394, 1978
Hyde J. B., Bernardi M., 2009b, MNRAS, 396, 1171
Jaffe W., 1983, MNRAS, 202, 995
Jahnke K., Macciò A. V., 2011, ApJ, 734, 92
Janz J., Lisker T., 2008, ApJ, 689, L25
Janz J., Lisker T., 2009, ApJ, 696, L102
Jiang F., van Dokkum P., Bezanson R., Franx M., 2012, ApJ, 749, L10
Kassin S. A., de Jong R. S., Weiner B. J., 2006, ApJ, 643, 804
Kauffmann G. et al., 2003a, MNRAS, 341, 33
Kauffmann G. et al., 2003b, MNRAS, 341, 54
Kelly B. C., 2007, ApJ, 665, 1489
Kelson D. D., van Dokkum P. G., Franx M., Illingworth G. D., Fabricant D., 1997, ApJ, 478, L13
Kennicutt R. C., Jr, 1998, in Howell G. G. D., ed., ASP Conf. Ser. Vol. 142, 38th Herstmonceux Conf. The Stellar Initial Mass Function. Astron. Soc. Pac., San Francisco, p. 1
Kereš D., Katz N., Weinberg D. H., Davé R., 2005, MNRAS, 363, 2
Khochfar S., Ostriker J. P., 2008, ApJ, 680, 54
Khochfar S., Silk J., 2006, MNRAS, 370, 902
Khochfar S. et al., 2011, MNRAS, 417, 845 (Paper VIII)
Kirby E. M., Jerjen H., Ryder S. D., Driver S. P., 2008, AJ, 136, 1866

Koopmans L. V. E., Treu T., Bolton A. S., Burles S., Moustakas L. A., 2006, ApJ, 649, 599
Kormendy J., 1977, ApJ, 218, 333
Kormendy J., 1985, ApJ, 295, 73
Kormendy J., Bender R., 2012, ApJS, 198, 2
Kormendy J., Gebhardt K., 2001, in Wheeler J. C., Martel H., eds, AIP Conf. Ser. Vol. 586, 20th Texas Symposium on Relativistic Astrophysics. Astron. Soc. Pac., San Francisco, p. 363
Kormendy J., Kennicutt R. C., Jr, 2004, ARA&A, 42, 603
Kormendy J., Fisher D. B., Cornell M. E., Bender R., 2009, ApJS, 182, 216
Krajnović D. et al., 2013a, MNRAS, submitted (Paper XXIV)
Krajnović D. et al., 2013b, MNRAS, 432, 1768 (Paper XVII)
Kroupa P., 2001, MNRAS, 322, 231
Kroupa P., 2002, Sci, 295, 82
Kroupa P., Weidner C., 2003, ApJ, 598, 1076
Kroupa P., Weidner C., Pflamm-Altenburg J., Thies I., Dabringhausen J., Marks M., Maschberger T., 2013, in Oswalt T. D., Gilmore G., eds, Planets, Stars and Stellar Systems, Vol. 5. Springer, Berlin, p. 115
Kuntschner H. et al., 2006, MNRAS, 369, 497
Kuntschner H. et al., 2010, MNRAS, 408, 97
Lablanche P.-Y. et al., 2012, MNRAS, 424, 1495 (Paper XII)
Lauer T. R. et al., 2007a, ApJ, 662, 808
Lauer T. R. et al., 2007b, ApJ, 664, 226
Law D. R., Shapley A. E., Steidel C. C., Reddy N. A., Christensen C. R., Erb D. K., 2012, Nat, 487, 338
Longhetti M., Saracco P., 2009, MNRAS, 394, 774
Magorrian J. et al., 1998, AJ, 115, 2285
Mancini C. et al., 2010, MNRAS, 401, 933
Maraston C., 2005, MNRAS, 362, 799
Maraston C., Daddi E., Renzini A., Cimatti A., Dickinson M., Papovich C., Pasquali A., Pirzkal N., 2006, ApJ, 652, 85
Martig M., Bournaud F., Teyssier R., Dekel A., 2009, ApJ, 707, 250
Martig M. et al., 2013, MNRAS, 432, 1914 (Paper XXII)
Matković A., Guzmán R., 2005, MNRAS, 362, 289
McConnell N. J., Ma C.-P., Gebhardt K., Wright S. A., Murphy J. D., Lauer T. R., Graham J. R., Richstone D. O., 2011, Nat, 480, 215
Mei S. et al., 2007, ApJ, 655, 144
Meurer G. R. et al., 2009, ApJ, 695, 765
Mihos J. C., Hernquist L., 1994, ApJ, 431, L9
Misgeld I., Hilker M., 2011, MNRAS, 414, 3699
Misgeld I., Mieske S., Hilker M., 2008, A&A, 486, 697
Misgeld I., Hilker M., Mieske S., 2009, A&A, 496, 683
Moster B. P., Somerville R. S., Maulbetsch C., van den Bosch F. C., Macciò A. V., Naab T., Oser L., 2010, ApJ, 710, 903
Naab T., Johansson P. H., Ostriker J. P., 2009, ApJ, 699, L178
Napolitano N. R., Romanowsky A. J., Tortora C., 2010, MNRAS, 405, 2351
Navarro J. F., Frenk C. S., White S. D. M., 1996, ApJ, 462, 563
Newman A. B., Ellis R. S., Bundy K., Treu T., 2012, ApJ, 746, 162
Nipoti C., Londrillo P., Ciotti L., 2003, MNRAS, 342, 501
Nipoti C., Treu T., Auger M. W., Bolton A. S., 2009, ApJ, 706, L86
Onodera M. et al., 2012, ApJ, 755, 26
Oser L., Ostriker J. P., Naab T., Johansson P. H., Burkert A., 2010, ApJ, 725, 2312
Oser L., Naab T., Ostriker J. P., Johansson P. H., 2012, ApJ, 744, 63
Padmanabhan N. et al., 2004, New Astron., 9, 329
Paturel G., Petit C., Prugniel P., Theureau G., Rousseau J., Brouty M., Dubois P., Cambrésy L., 2003, A&A, 412, 45
Peng C. Y., 2007, ApJ, 671, 1098
Press W. H., Teukolsky S. A., Vetterling W. T., Flannery B. P., 1992, Numerical Recipes in fortran. The Art of Scientific Computing, 2nd edn. Cambridge Univ. Press, Cambridge
Prugniel P., Simien F., 1996, A&A, 309, 749
Renzini A., 2005, in Corbelli E., Palla F., Zinnecker H., eds, Astrophysics and Space Science Library, Vol. 327, The Initial Mass Function 50 Years Later. Springer, Dordrecht, p. 221
Renzini A., Ciotti L., 1993, ApJ, 416, L49
Robertson B., Cox T. J., Hernquist L., Franx M., Hopkins P. F., Martini P., Springel V., 2006, ApJ, 641, 21
Rousseeuw P., Van Driessen K., 2006, Data Mining and Knowledge Discovery, 12, 29
Rybicki G. B., 1987, in de Zeeuw P. T., ed., Proc. IAU Symp. Vol. 127, Structure and Dynamics of Elliptical Galaxies. Reidel, Dordrecht, p. 397
Salpeter E. E., 1955, ApJ, 121, 161
Sánchez-Blázquez P. et al., 2006, MNRAS, 371, 703
Sandage A., 1961, The Hubble Atlas. Carnegie Institution, Washington
Sarzi M. et al., 2010, MNRAS, 402, 2187
Sarzi M. et al., 2013, MNRAS, 432, 1845 (Paper XIX)
Schechter P., 1976, ApJ, 203, 297
Schiavon R. P., Barbuy B., Bruzual A. G., 2000, ApJ, 532, 453
Schulz A. E., Mandelbaum R., Padmanabhan N., 2010, MNRAS, 408, 1463
Scott N. et al., 2009, MNRAS, 398, 1835
Scott N. et al., 2013a, MNRAS, 432, 1894 (Paper XXI)
Scott N., Graham A. W., Schombert J., 2013b, ApJ, 768, 76
Sersic J. L., 1968, Atlas de galaxias australes. Observatorio Astronomico, Cordoba, Argentina
Shankar F., Bernardi M., 2009, MNRAS, 396, L76
Shen S. et al., 2003, MNRAS, 343, 978
Silk J., Rees M. J., 1998, A&A, 331, L1
Silverman B. W., 1986, Density Estimation for Statistics and Data Analysis, Vol. 26. Chapman & Hall/CRC, Boca Raton
Skrutskie M. F. et al., 2006, AJ, 131, 1163
Smith R. J., Lucey J. R., Carter D., 2012, MNRAS, 426, 2994
Sonnenfeld A., Treu T., Gavazzi R., Marshall P. J., Auger M. W., Suyu S. H., Koopmans L. V. E., Bolton A. S., 2012, ApJ, 752, 163
Spiniello C., Trager S. C., Koopmans L. V. E., Chen Y. P., 2012, ApJ, 753, L32
Spinrad H., Taylor B. J., 1971, ApJS, 22, 445
Spitzer L., Jr, Baade W., 1951, ApJ, 113, 413
Suyu S. H. et al., 2012, ApJ, 750, 10
Tacconi L. J. et al., 2010, Nat, 463, 781
Thomas D., Maraston C., Bender R., Mendes de Oliveira C., 2005, ApJ, 621, 673
Thomas J., Saglia R. P., Bender R., Thomas D., Gebhardt K., Magorrian J., Corsini E. M., Wegner G., 2009, ApJ, 691, 770
Thomas J. et al., 2011, MNRAS, 415, 545
Tonry J. L., Dressler A., Blakeslee J. P., Ajhar E. A., Fletcher A. B., Luppino G. A., Metzger M. R., Moore C. B., 2001, ApJ, 546, 681
Tortora C., Napolitano N. R., Romanowsky A. J., Capaccioli M., Covone G., 2009, MNRAS, 396, 1132
Tortora C., Napolitano N. R., Romanowsky A. J., Jetzer P., 2010, ApJ, 721, L1
Tortora C., Romanowsky A. J., Napolitano N. R., 2013, ApJ, 765, 8
Tremblay B., Merritt D., 1996, AJ, 111, 2243
Treu T. et al., 2005, ApJ, 633, 174
Treu T., Auger M. W., Koopmans L. V. E., Gavazzi R., Marshall P. J., Bolton A. S., 2010, ApJ, 709, 1195
Treu T., Dutton A. A., Auger M. W., Marshall P. J., Bolton A. S., Brewer B. J., Koo D. C., Koopmans L. V. E., 2011, MNRAS, 417, 1601
Trujillo I. et al., 2006, MNRAS, 373, L36
Trujillo I., Conselice C. J., Bundy K., Cooper M. C., Eisenhardt P., Ellis R. S., 2007, MNRAS, 382, 109
Trujillo I., Ferreras I., de La Rosa I. G., 2011, MNRAS, 415, 3903
Valentinuzzi T. et al., 2010, ApJ, 712, 226
van de Ven G., Falcón-Barroso J., McDermid R. M., Cappellari M., Miller B. W., de Zeeuw P. T., 2010, ApJ, 719, 1481
van den Bergh S., 1976, ApJ, 206, 883
van den Bosch F. C., 1997, MNRAS, 287, 543
van der Marel R. P., van Dokkum P. G., 2007, ApJ, 668, 756
van der Wel A., Bell E. F., van den Bosch F. C., Gallazzi A., Rix H.-W., 2009a, ApJ, 698, 1232
van der Wel A., Rix H.-W., Holden B. P., Bell E. F., Robaina A. R., 2009b, ApJ, 706, L120
van der Wel A. et al., 2011, ApJ, 730, 38

van Dokkum P. G., 2008, ApJ, 674, 29
van Dokkum P., 2011, Nat, 473, 160
van Dokkum P. G., Conroy C., 2010, Nat, 468, 940
van Dokkum P. G., Conroy C., 2011, ApJ, 735, L13
van Dokkum P. G., Conroy C., 2012, ApJ, 760, 70
van Dokkum P. G., Franx M., 1996, MNRAS, 281, 985
van Dokkum P. G., Franx M., Kelson D. D., Illingworth G. D., 1998, ApJ, 504, L17
van Dokkum P. G. et al., 2008, ApJ, 677, L5
van Dokkum P. G. et al., 2010, ApJ, 709, 1018
Vazdekis A., Ricciardelli E., Cenarro A. J., Rivero-González J. G., Díaz-García L. A., Falcón-Barroso J., 2012, MNRAS, 424, 157
Wake D. A., van Dokkum P. G., Franx M., 2012, ApJ, 751, L44
Wegner G. A., Corsini E. M., Thomas J., Saglia R. P., Bender R., Pu S. B., 2012, AJ, 144, 78
Weijmans A.-M. et al., 2013, MNRAS, submitted (Paper XXIII)
Wilkins S. M., Hopkins A. M., Trentham N., Tojeiro R., 2008, MNRAS, 391, 363
Williams M. J., Bureau M., Cappellari M., 2009, MNRAS, 400, 1665
Williams M. J., Bureau M., Cappellari M., 2010a, MNRAS, 409, 1330
Williams R. J., Quadri R. F., Franx M., van Dokkum P., Toft S., Kriek M., Labbé I., 2010b, ApJ, 713, 738
Wolf J., Martinez G. D., Bullock J. S., Kaplinghat M., Geha M., Muñoz R. R., Simon J. D., Avedo F. F., 2010, MNRAS, 406, 1220
Worthey G., 1994, ApJS, 95, 107
Wuyts S., Franx M., Cox T. J., Hernquist L., Hopkins P. F., Robertson B. E., van Dokkum P. G., 2009, ApJ, 696, 348
Wuyts S. et al., 2011, ApJ, 742, 96
York D. G. et al., 2000, AJ, 120, 1579
Young C. K., Currie M. J., 1994, MNRAS, 268, L11
Young L. M. et al., 2011, MNRAS, 414, 940 (Paper IV)
Zaritsky D., Gonzalez A. H., Zabludoff A. I., 2006, ApJ, 638, 725
Zepf S. E., Silk J., 1996, ApJ, 466, 114
Zhu G., Blanton M. R., Moustakas J., 2010, ApJ, 722, 491

SUPPORTING INFORMATION

Additional Supporting Information may be found in the online version of this article:

Table 1. Central velocity dispersion, DM fraction and M/L for the ATLAS3D sample of 260 ETGs (http://mnras.oxfordjournals.org/lookup/suppl/doi:10.1093/mnras/stt644/-/DC1).

Please note: Oxford University Press is not responsible for the content or functionality of any supporting materials supplied by the authors. Any queries (other than missing material) should be directed to the corresponding author for the article.

This paper has been typeset from a TEX/LATEX file prepared by the author.